Universitat Autònoma de Barcelona
Facultat de Ciències - Física
Istitut Català de Nanotecnologia

Coupling of metal-organic complexes to magnetic substrates investigated by polarized x-ray absorption spectroscopy

Alberto Lodi Rizzini

A dissertation submitted to attain
the degree of Doctor of Philosophy

Supervisor: Prof. Pietro Gambardella

Contents

Abstract

Metal-organic molecules at the interface with metallic substrates are interesting systems for future applications in electronic and spintronic devices, as they hold promise for replacing some of the metal-based magnetic components in use today. Spin carrying molecules are highly attractive materials, both as ordered two-dimensional films in multilayer structures and as single magnetic units, because of their reduced dimensions and functional properties. Among this class of molecules, single molecule magnets (SMMs) are the most promising materials, because they combine bulk magnetic properties and molecular scale dimensions. Several problems limit their application in real devices; however the main one is the low blocking temperature (T_B), tipically in the helium liquid range, under which SMMs behave like nanomagnets; furthermore, it is not an easy task to control the magnetic moment of a single molecule. To overcome these obstacles, many strategies are under investigation, including single molecules in break junctions, molecules deposition on magnetic substrates, change of the

organic ligand to modify the ligand field, etc..

To study these materials, synchrotron radiation spectroscopy represents a powerful technique: X-ray absorption spectroscopy (XAS) and x-ray magnetic circular dichroism (XMCD), in particular, allow element selectivity and independent measurements of the atomic orbital and spin moments, fundamentals quantities for understanding the macroscopic magnetic properties of the matter.

We investigate the interaction of $TbPc_2$ SMMs with ferromagnetic (FM) Ni surfaces. Using XMCD magnetometry, we show that $TbPc_2$ couple antiferromagnetically to Ni films through ligand-mediated superexchange. The magnitude, but not the sign of the exchange coupling energy, can be tailored by reducing or oxidizing the substrate. Contrary to paramagnetic molecules, we find that the SMM magnetic moment does not follow the magnetization of the underlying FM layer, depending on the relative orientation of the molecule and substrate magnetic anisotropy axes, superexchange, and Zeeman interaction. Coupled to Ni, $TbPc_2$ retain their intrinsic SMM properties, but they exhibit enhanced thermal stability relative to isolated molecules, demonstrating an effective approach to include SMM in spintronic devices.

A further step towards the control of SMMs is to induce coupling with an antiferromagnetic (AFM) substrate. This finding may enable independent magnetization reversal of molecular layers with respect to the pinning substrate. The key phenomenon in this case is exchange bias, the unidirectional magnetic anisotropy

at the interface between FM and AFM layers, used in spintronics to stabilize and control the magnetization of multilayer structures. Here we investigate the possibility to induce exchange bias between SMMs and metallic or oxide AFM layers. Element-resolved XMCD measurements show that $TbPc_2$ molecules deposited on an AFM Mn thin film present magnetic hysteresis and a negative horizontal shift of the Tb magnetization loop after field cooling. This evidence of exchange bias is consistent with the observation of pinned spins in the Mn layer that couple parallel to the Tb magnetic moment during field cooling. Conversely, molecules deposited on CoO substrates present paramagnetic magnetization loops with no indication of exchange bias. These experiments demonstrate the ability of SMM to polarize the uncompensated pinned spins of an antiferromagnet and realize metal-organic exchange biased heterostructures.

Finally, we draw attention to the behaviour of paramagnetic molecules, such as MnPc. We deposited MnPc on several substrates, both magnetic and non magnetic, and performed a systematic study of how the electronic configuration of the Mn ions and their magnetic moment are modified. What we observe is that the MnPc electronic configuration is highly affected by the substrate and that the main mechanism inducing changes is likely charge transfer. MnPc on FM Ni behaves, as expected, like a normal paramagnetic molecule on FM layers, mimicking the substrate magnetization, while no exchange bias is observed on AFM

oxides layers, as for $TbPc_2$ SMM. We also tried to estimate the magnetic moment for each sample, finding unexpected results that need to be clarified. This study is still at a first stage, and needs the support of further measurements and calculations to confirm our assumptions.

Resumen

Las moléculas metal-orgánicas en la intercara con sustratos metálicos son sistemas interesantes para aplicaciones futuras en la grabación magnética y dispositivos de espintrónica, ya que prometen sustituir algunos de los componentes magnéticos basados en metales en uso hoy en día. Las moléculas que llevan espín son materiales muy atractivos, tanto como capas finas bidimensionales en estructuras de multi-capas o como unidades magnéticas individuales, debido a sus reducidas dimensiones y propiedades funcionales. Entre esta clase de moléculas, los imanes moleculares (SMMs) son los más prometedores, ya que combinan propiedades magnéticas de bulk y dimensiones a escala molecular. Varios problemas limitan su aplicación en dispositivos reales: la principal es la baja temperatura de bloqueo T_B, típicamente alrededor de la temperatura de liquefacción de helio, por debajo del cuál los SMMs se comportan como nanoimanes; además, controlar el momento magnético de una sola molécula no es una tarea fácil. Para superar estos obstáculos se están investigando muchas estrategias y la más

prometedora parece ser la deposición sobre sustratos magnéticos.

Para el estudio de estos materiales, las espectroscopías de radiación sincrotrón representan técnicas muy poderosas: la espectroscopía de absorción de rayos X (XAS) y el dicroísmo magnético circular de rayos X (XMCD), en particular, permiten medir selectivamente diferentes elementos y mediciones independientes de los momentos atómicos orbitales y de espín, cantidades fundamentales para la comprensión de las propiedades magnéticas macroscópicas de la materia.

En este estudio se ha investigado la interacción del SMM $TbPc_2$ con superficies ferromagnéticas (FM) de Ni. Usando la magnetometría XMCD, se ha demostrado que $TbPc_2$ se acopla antiferromagneticamente a la capa de Ni a través de la interacción de supercanje mediada por el ligando. La magnitud, pero no el signo, de la energía de acoplamiento de canje puede ser ajustado mediante la reducción o la oxidación del sustrato. Contrariamente a las moléculas paramagnéticas, encontramos que el momento magnético de los SMMs no sigue la magnetización de la capa FM subyacente en cualquier condición, sino que depende de la orientación relativa de los ejes de anisotropía magnética de la molécula y del sustrato, de la interacción de supercanje y de la interacción Zeeman. Las moléculas de $TbPc_2$, acopladas al Ni, conservan sus propiedades intrínsecas de SMM, pero también presentan una mejor estabilidad térmica respecto a la molécula aislada, lo que demuestra una estrategia efectiva para incluir SMM

en dispositivos de espintrónica.

Se puede dar un paso más hacia el control de un SMM estudiando el acoplamiento con sustratos antiferromagnéticos (AFM). Esto permitiría la inversión de la magnetización de capas moleculares con respecto al sustrato que bloquea el espín. El fenómeno clave para demostrar este acoplamiento es el exchange bias, la anisotropía magnética unidireccional en la intercara entre capas FM y AFM, usada en espintrónica para estabilizar y controlar la magnetización de estructuras multicapas. Aquí se investiga la posibilidad de inducir exchange bias entre SMM y capas AFM metálicas o de óxido. Las medidas de XMCD muestran que las moléculas de $TbPc_2$ depositadas sobre una capa fina AFM de Mn tienen, después del enfriamiento con un campo magnetico externo aplicado, una curva de magnetización abierta y desplazada horizontalmente. Esta evidencia de exchange bias es coherente con la observación de espínes bloqueados en la capa de Mn que se acoplan paralelamente al momento magnético del Tb, durante el enfriamiento en campo. Al contrario, las moléculas depositadas sobre sustratos de CoO presentan ciclos de magnetización paramagnéticos sin indicación alguna de exchange bias. Estos experimentos demuestran la capacidad de los SMMs para polarizar los espínes bloqueados no compensados de un antiferromagneto y para formar heteroestructuras metal-orgánicas que presentan exchange bias.

Por último, se ha puesto atención en la molécula param-

agnética MnPc. Se ha depositado esta molécula en varios sustratos, tanto magnéticos como no magnéticos, y se ha llevado a cabo un estudio sistemático de la modificación de la configuración electrónica en las diferentes muestras. Lo que observamos es que la configuración electrónica del MnPc se ve muy afectada por el sustrato y que el mecanismo principal que induce los cambios es probablemente la transferencia de carga. El MnPc en sustratos FM de Ni se comporta previsiblemente como las otras moléculas paramagnéticas en capas FM, siguiendo la magnetización del sustrato, mientras que, en capas AFM de óxido, no se observa exchange bias, como en el caso de SMM $TbPc_2$. También hemos tratado de calcular el momento magnético de cada muestra, descubriendo resultados inesperados que necesitan ser aclarados. Este estudio se encuentra todavía en una primera etapa, y necesita el apoyo de otras mediciones y cálculos teoricós para confirmar nuestras suposiciones.

Chapter 1

Introduction

Metallic thin films became the object of intense investigation starting from the 1970s. In particular, research focused on magnetic thin films for applications in magnetic recording. Transition metals Fe, Co, Ni and their alloys in the form of polycrystalline thin films were the most promising materials to substitute ferrite particulate disks. This was favoured also by the improvement of the deposition techniques, like sputtering and evaporation, that allowed to prepare films with better thinness, with low defects and then with an improved smoothness. At the end of the 1980s the discovery of the giant magnetoresistance (GMR) [6, 10] enabled to build a new generation of magnetic reading heads. This was also the first application to a real device of spintronics [23], namely spin based electronics, the field of research that aims to exploit the degree of freedom given by the spin, in contrast to conventional

electronics that make use only of the charge to transport information. The GMR read heads are basically made by a multilayer structure with two ferromagnetic films separated by a very thin non-magnetic spacer: when the magnetization of the two layers is parallel the resistance is relatively low, while in the antiparallel configuration has a huge increase [64]. This technology allowed to build more sensitive reading heads to the fringing fields of the magnetized regions of an hard disk and, therefore, to increase the areal density of data stored. This combined with the introduction of perpendicular recording media, allowed to increase the slope of the Moore law starting from the 1990s. Regardless all these progresses that always surpassed all the optimistic predictions, radical changes are required in device design for the future. Magnetic thin films have an intrinsic limit: at a certain dimensions, the magnetized regions of a thin film enter in the so called superparamagnetic limit, in which they cannot keep a fixed magnetization that starts to randomly flip under the influence of the temperature.

To overcome this limit, new materials and new methods have been investigated in the last decade. Metal-organic molecules are particularly attracting materials because of their properties [67]. The structure of these molecules normally is constituted by a core of one or more metal ions and the organic ligand surrounding the core. The dimensions are in general in the range of 1-10 nm, so that one can see them as perfect building blocks for achieving hybrid devices and, in the case of magnetic molecules, they can

represent single magnetic units. The possibility to change and to functionalize the ligand part makes metal-organic molecules versatile for different applications: we can attach them to functionalized surfaces or, if the ligand has a planar shape, deposit them on clean metallic surfaces and leave them free, depending on pressure and temperature condition, to self-assemble in uniform layers. This bottom-up approach is completely opposite with respect to that of thin films.

Among organic molecules, single molecule magnets (SMMs) represent the most promising class for application in magnetic recording, spintronics and quantum computing. SMMs combine the properties of bulk magnetic materials, as the slow relaxation of the magnetization, with the molecular scale [12]. The main obstacle of using SMMs in real devices is given by the low temperatures at which they show a stable magnetization. The goal of the research on SMMs is to stabilize and take control of the magnetic moment at high temperatures. The idea of this work is to stabilize the magnetic properties of both SMM and paramagnetic molecules depositing them on magnetic surfaces. In particular, we are interested to check the presence of magnetic coupling between molecules and surfaces. This approach is not new, but we will show some original results.

The thesis is organized as follows. Chapter 2 presents the basic principles of synchrotron radiation spectroscopies, focusing especially on x-ray absorption spectroscopy and on x-ray magnetic

circular dichroism. The element selectivity and the possibility of estimating orbital and spin magnetic moments separately make these techniques particularly suitable for investigating the interaction of metal-organic molecules with the underneath surfaces. It also presents the experimental the set-up of the beamline where our measurements took place. Chapter 3 reports a brief overview on single molecules magnets, a particular class of metal-organic molecules. The attention is driven on the bis-phthalocyaninato terbium ($TbPc_2$), since we choose this molecule for our experiments. The second part of the chapter shows our results for the $TbPc_2$ deposited on ferromagnetic surfaces. Chapter 4 is organized similarly to the previous chapter. The first part provides a synthetic resume on the exchange bias effect, while the second part illustrates our experiments on $TbPc_2$ when the molecule is deposited on antiferromagnetic substrates, aiming for the observation of the exchange bias on our samples. Chapter 5 changes the subject, as we reports experiments on the paramagnetic manganese phthalocyanine (MnPc). This molecule is deposited on several surfaces, both magnetic and non magnetic. The purpose of these measurements is to understand the coupling mechanisms between molecules and surfaces and in which way they affect the electronic structure and magnetic moments. Finally, we resume the results of this dissertation and we give some suggestions in order to continue this work.

Chapter 2

Experimental techniques

This chapter presents the principles underneath the experimental techniques employed in this thesis work. The focus is on X-ray Absorption Spectroscopy (XAS) and X-ray Magnetic Circular Dichroism (XMCD). Other dichroisms are also mentioned, such as X-ray Natural Linear Dichroism (XNLD), which we used to retrieve information about the orientation of the molecules on surfaces. We discuss different methods to measure XAS, and give an example of application of the XMCD sum rules to transmission measurements. Finally we provide a descripton of the experimental set-up of the ID08 beamline of the European Synchrotron Radiation Facility (ESRF), where we ran the experiments reported in the next chapters.

2.1 X-ray Absorption Spectroscopy

The basic principle underlying the XAS and XMCD, in particular, is the polarization-dependent photon absorption in magnetic materials.

The polarization is a property of the photon that describes the oscillation direction of the electric field vector **E** during the propagation of the particle. The vector **E** oscillates in a plane perpendicular to the propagation direction **k**. If **E** oscillates on a straight line, the light is linearly polarized. When the tip of the vector **E** describes in an ellipse (circle), the light is elliptically (circularly) polarized. If, when looking at the tip of the **E** vector as the light comes straight toward us, **E** goes around in a counterclockwise (clockwise) direction, we call it right-hand (left-hand) circular polarization [65]. This is Feynman s definition reported in his The Feynman Lectures on physics . It is important to underline this definition because in some books the opposite conventions are used.

Photons are bosons with an angular momentum quantum number $L = 1$ (in units of $\hbar$). This number is the magnitude of the angular momentum and it is independent of the state of polarization. It is customary to define the photon angular momentum by the quantum number L_z, which represents the expectation value of the angular momentum operator along the quantization axis z. In this case $\mathbf{L_z} = 0 \pm 1$.

The polarization-dependent photon angular momentum is used to indicate the degree of polarization, since this is defined solely by the direction of the torque the photon applies to the atomic electron, and we will indicate it in general as q. q can have values $+1$, 0 and -1, where $q = +1$ ($q = -1$) describe right (left) circularly-polarized photons, while $q = 0$ linearly polarized photons.

In order to calculate quantitatively the absorption process, one has to take into account the time-dependent perturbation of the sample due to the electromagnetic field, that induces transitions between an initial state i and final state f . If the system evolves directly from one state to the other, we speak about first-order process, otherwise, if an intermediate state n is involved we call it second-order process. In the formalism developed by Kramers, Heisemberg and Dirac, also known as Fermi s golden rules, the transition probability is expressed as

$$T_{if} = \frac{2\pi}{\hbar} \left| f\ H_{int}\ i\ + \sum_n \frac{f\ H_{int}\ n \quad n\ H_{int}\ i}{\epsilon_i - \epsilon_n} \right|^2 \delta\left(\epsilon_i - \epsilon_n\right) \rho\left(\epsilon_f\right) \tag{2.1}$$

where the sum is over all possible energy states, $\rho\left(\epsilon_f\right)$ is the density of final states per unit energy and the Hamiltonian for absorption processes H_{int} has the form

$$H_{int} = \frac{e}{m_e} \mathbf{p} \cdot \mathbf{A} \tag{2.2}$$

By quantizing the electromagnetic field one can separate the matrix elements in equation 2.1 into electronic and photon parts, evaluate the photon part, and obtain the matrix elements in terms of transitions between the electronic states a and b. The matrix elements have the form

$$M = \ b\ \mathbf{p}\boldsymbol{\epsilon} e^{i\mathbf{k}\cdot\mathbf{r}}\ a \tag{2.3}$$

where $\mathbf{p}$ is the electron momentum, $\boldsymbol{\epsilon}$ the unit photon polarization vector and $\mathbf{k}$ the photon unit wave vector. Introducing the *dipole approximation*, it is possible to eliminate the dependence of the matrix element on $\mathbf{k}$

$$M = \ b\ \mathbf{p}\boldsymbol{\epsilon}\,(1 + \mathbf{k}\cdot\mathbf{r} + \quad)\ a\ \approx\ b\ \mathbf{p}\boldsymbol{\epsilon}\ a\ = im_e \quad b\ \mathbf{r}\boldsymbol{\epsilon}\ a \tag{2.4}$$

where m_e is the mass of the electron and $\quad = \ _b - \ _a$ the photon frequency associated to the transition from a to b. The electric dipole approximation assumes that the photon wavelength is long compared to the dimensions of the atom, i.e. $\mathbf{r}\ \ll 1 \quad \mathbf{k}\ = \lambda\ 2\pi$, so that the electric field is constant over the atomic volume.

2.1.1 The polarization dependent dipole operator

In the dipole approximation, the polarization dependent dipole operator is given by the product $\epsilon \cdot \mathbf{r}$, where ϵ is the unit photon polarization vector and $\mathbf{r}$ the electron position vector, which in Cartesian coordinates is

$$\mathbf{r} = x\mathbf{e_x} + y\mathbf{e_y} + z\mathbf{e_z} \tag{2.5}$$

For linearly polarized light X-rays, the direction of the **E** vector determines the X-ray absorption intensity, and in the case it is aligned with the Cartesian axis we have the corresponding real unit polarization vectors

$$\boldsymbol{\epsilon}_{\boldsymbol{x}}^{\mathbf{0}} = \boldsymbol{\epsilon}_{\boldsymbol{x}} = \mathbf{e_x} \quad \boldsymbol{\epsilon}_{\boldsymbol{y}}^{\mathbf{0}} = \boldsymbol{\epsilon}_{\boldsymbol{y}} = \mathbf{e_y} \quad \boldsymbol{\epsilon}_{\boldsymbol{z}}^{\mathbf{0}} = \boldsymbol{\epsilon}_{\boldsymbol{z}} = \mathbf{e_z} \tag{2.6}$$

For circularly polarized X-rays, in the case $\mathbf{k}$ z, we write the unit polarization vector as

$$\boldsymbol{\epsilon}_{\boldsymbol{z}}^{\pm} = \mp\frac{1}{\overline{2}}\left(\boldsymbol{\epsilon}_{\boldsymbol{x}} \pm i\boldsymbol{\epsilon}_{\boldsymbol{y}}\right) \tag{2.7}$$

The dipole operators $P_\alpha^\pm = \epsilon \cdot \mathbf{r} = \epsilon_\alpha^{\mathbf{q}} \cdot \mathbf{r}$ can be rewritten in terms of spherical harmonics $Y_{l,m}\left(\theta\ \phi\right)$ or, because of the prefactors, in terms of the Racah s spherical tensor operators; for $\alpha = z$ and $l = 1$ we have

$$P_z^\pm = \boldsymbol{\epsilon}_{\boldsymbol{z}}^{\pm} \cdot \mathbf{r} = \mp\frac{1}{\overline{2}}\left(\mathbf{e_x} \pm i\mathbf{e_y}\right) = r\sqrt{\frac{4\pi}{3}}Y_{1,\pm1} = rC_0^{(1)} \tag{2.8}$$

$$P_z^0 = \boldsymbol{\epsilon}_{\boldsymbol{z}} \cdot \mathbf{r} = z = r\sqrt{\frac{4\pi}{3}}Y_{1,0} = rC_{\pm1}^{(1)} \tag{2.9}$$

The dipole operator for all polarization cases ($q = 0\ \pm1$) and orientations of axes of the coordinate system ($\alpha = x\ y\ z$) presents the general form

$$P^q_\alpha \; r = \sum_{p=0,\pm1} e^q_{\alpha,p} C^{(1)}_p = e^q_{\alpha,1} C^{(1)}_1 + e^q_{\alpha,0} C^{(1)}_0 + e^q_{\alpha,-1} C^{(1)}_{-1} \quad (2.10)$$

Aware of this, we can rewrite the transition matrix elements as $b\,\epsilon \cdot \mathbf{r}\,a \;=\; b\,P^q_\alpha\,a$.

The calculation of the transitions matrix elements depends on the wavefuctions a and b . The simplest wavefunctions that we can consider are the atomic wavefuctions in a central field

$$a \;=\; b \;=\; R_{n,l}; l \;\; m_l \;\; s \;\; m_s \;\; = R_{n,l} Y_{l,m_l} \theta_{\,s,m_s} \quad (2.11)$$

where $R_{n,l}$ is the radial component of a shell n with angular momentum l and Y_{l,m_l} are spherical harmonics characterizing the angular part and $\theta_{\,s,m_s}$ is the spin part. General wavefunctions appropriate to describe an atom in a solid, where one has to take into account ligand field or a band state that includes for example exchange and spin-orbit effects, can be written as linear combination of atomic functions of the form 2.11. The dipole operator, for transitions from core shell with angular momentum c to unfilled valence shell with angular momentum l, becomes

$$b\,P^q_\alpha\,a \;= \delta(m_s \;\; m_s) \;\; R_{n',l}(r)\; r\; R_{n,c}(r) \sum_{m_c,m_l,p} e^q_{\alpha,p} \;\; l \;\; m_l \; C^{(1)}_p \; c \;\; m_c \quad (2.12)$$

It is worth noting that we can separate the contribution of the radial and angular part and calculate them separately. The dipole operator does not act on the spin and only transitions that preserve the spin are allowed. The dependence on the dipole operator is completely contained in the angular part, while the radial part determines the angle-integrated transition strength. By considering the nonvanishing matrix elements, we can extract the dipole selection rules

$$\Delta l = l - l = \pm 1 \tag{2.13}$$

$$\Delta m_l = m_l - m_l = q = 0 \pm 1 \tag{2.14}$$

$$\Delta s = s - s = 0 \tag{2.15}$$

$$\Delta m_s = m_s - m_s = 0 \tag{2.16}$$

where $q\hbar$ is the X-ray angular momentum.

2.1.2 X-ray absorption: one-electron and configuration pictures

The X-ray absorption could be described in different ways. The simplest one is the so called *one-electron picture*. In this model absorption is viewed as a simple excitation of a single electron from the core-shell state to the available valence shell due to the energy transferred from the X-ray photon. However, this picture is not fully correct because it ignores all the other electrons during

excitation process and treats them as passive. This simplified view is intuitive and it allows us to visualize and easily calculate the physical absorption process and for this reason it is often used in X-ray absorption literature. The initial state refers to a core level state and can be expressed as

$$i \ = R_i\left(r\right) \ c \ m_c; s = 1 \ \ 2 \ m_s \tag{2.17}$$

where $R_i\left(r\right)$ is the radial component. In the same way we can express the final state

$$f \ = R_f\left(r\right) \ l \ m_l; s = 1 \ \ 2 \ m_s \tag{2.18}$$

Transitions between the two states will occur only when there is an available empty valence state. It is important to underline that we expressed equations 2.17 and 2.18 in the basis states $l \ m_l; s \ m_s$, where the spin and orbital momenta are uncoupled. The electric dipole field only interacts with the orbital moment and it will excite transitions following the selections rules 2.16: the dipole matrix elements will be zero unless $l = c \pm 1$ and $m_l = m_c + q$. Aware of this, we can express all the matrix elements in terms of the final state m_l.

The spin moments become involved in the matrix element through the spin-orbit coupling in the core level. The spin-orbit split core level states are expressed in terms of the basis states $j \ m_j$, with the total angular momentum $j = j_{\pm} = (c \pm 1 \ \ 2)$,

where c is the orbital momentum and $s = 1\ 2$ the electron spin. In terms of the uncoupled states $c\ m_c; s = 1\ 2\ m_s$ the initial state is

$$\begin{aligned} i &= R_i(r)\ j\ m_j \\ &= R_i(r) \sum_{m_c, m_s} c\ m_c; s = 1\ 2\ m_s\ \ j\ m_j\ \ c\ m_c; s = 1\ 2\ m_s \end{aligned} \tag{2.19}$$

where the radial component R_i is assumed to be the same for all electrons in the same subshell, and $c\ m_c; s = 1\ 2\ m_s\ \ j\ m_j$ are the Clebsh-Gordan coefficients.

The one-electron picture is misleading because it presents the spin-orbit splitting of the core shell as an initial state effect. In reality there is no splitting since the core shell is filled in the ground state.

The more correct way to describe X-ray absorption process is the *configuration picture*: an atom is excited from a ground or initial state configuration to an excited or final configuration. This picture describes multiplets, a set of different values of a total angular momentum J, which arises from a given set of spin and orbital angular momenta. A multiplet of an atom is determined from the spin and orbital momenta of all electrons belonging to that atom.

The total angular momentum is described, in general, in terms of two coupling schemes, depending on the strength of the spin-orbit coupling. If the spin orbit coupling is negligible, as in the

case of valence shell states in metallic solids, the Russell-Saunders (or LS) coupling scheme is applied. The term symbol for each possible multiplet configuration is given by

$$^{2S+1}L_J \tag{2.20}$$

where $\mathbf{L} = \sum_i \mathbf{l_i}$ and $\mathbf{S} = \sum_i \mathbf{s_i}$. The small letters denote the quantum number of individual electrons, while the capitol letters the atomic quantum numbers. The total angular momentum is then

$$\mathbf{J} = \mathbf{L} + \mathbf{S} \tag{2.21}$$

where the summation is a vector summation, so that J possible value are between $L + S$ and $L - S$.

If the spin-orbit coupling is stronger, such as for core shell electrons, it is more suitable to apply the jj-coupling scheme. In this case the net angular momentum is

$$\mathbf{J} = \sum_i \mathbf{j_i} \tag{2.22}$$

where $j_i = l_i + s_i$ is determined by the spin-orbit coupling interaction. In the description of an atomic configuration, the two schemes are often mixed, since the strength of the spin-orbit coupling can vary from subshell to subshell.

It is interesting to apply these approaches to some examples. The simplest case is represented by the transition $2p^6 3d^9$

$2p^5 3d^{10}$. This configuration presents a single hole in the $3d$ subshell, while all the states of lower energy are full. The angular momentum contribution from closed subshell is $J = L = S = 0$, hence the ground state angular momentum is given by the $3d$ shell only. The only possible configuration are $^2D_{5/2}$ and $^2D_{3/2}$, corresponding to the initals states $J = 5\ 2\ M_J$ and $J = 3\ 2\ M_J$. The possible configurations for the excited state are $^2P_{3/2}$ and $^2P_{1/2}$ (final states $J = 3\ 2\ M_J$ and $J = 1\ 2\ M_J$). The $^2D_{5/2}$ $^2P_{1/2}$ transition is forbidden by the selection rules 2.16. In this particular case we can notice the equivalence of the two pictures, that in part justify the use of the one-electron picture, being the initial and final states reversed. However, the spin-orbit splitted initial states cannot be true, since the $2p$ core shell is full and $S = L = 0$. Differences become explicit when a multi-hole case is considered. For example, in the case of $2p^6 3d^8$ $2p^5 3d^9$, assuming no spin-orbit coupling, the initial configuration, according to Hund s rules, is given by ^3F. Similarly one can calculate the final configuration, finding that the only possible trasitions are ^3F ^3D and ^3F ^3F, since the selection rules 2.16 are $\Delta L = 0 \pm 1$ and $\Delta M_L = q$. In comparison, the one-electron picture does not take into account the angular momentum interactions with the other electrons belonging to the same atom.

2.1.3 XNLD

X-ray Natural Linear Dichroism is one of the different types of X-ray dichroism. The term dichroism, originally referred to the polarization dependent absorption of the light. At the microscopic level the dichroic behaviour originates from the spatial anisotropy of the charge or the spin. In the case of XNLD the spins are not aligned and the effect depends only on the charge. This technique is used especially to probe the anisotropy of the valence charge and determine the orientation of molecules or functional groups on surfaces and in organic materials, and to probe the direction and nature of covalently bonded systems.

An easy way to visualize the polarization dependence underlying XNLD is the so called search light effect : for linear polarized X-rays, the electric field vector **E** acts like a search light for the direction of the maximum and minimum number of empty valence states. Knowing that in experiments on X-ray absorption electrons are exited from core shell to empty valence states, the transition intensity is directly proportional to the number of empty valence states in the direction of **E**.

In the case of excitation from core 1s to 2p valence states (K edge), the transition intensities are given by

$$\left| \; b \; \frac{P^q_\alpha}{r} \; a \; \right|^2 = \left| \; 2p_n \; \frac{P^0_\alpha}{r} \; 1s \; \right|^2 \tag{2.23}$$

where P^q_α is the polarization dependent dipole operator, $\alpha = x \;\; y \;\; z$

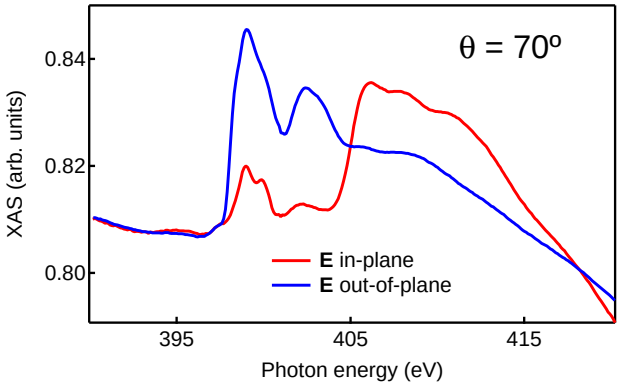

Figure 2.1: Linear horizontal and vertical absortpion spectra recorded at $\theta = 0°$, $T = 8K$ and $B = 0T$ on K-edge of N, in the MnPc molecules deposited on Cu(100).

and $q = 0$ represents the linearly polarized light with **E** x,y,z. For all s p_i (i = x,y,z) transitions, we find a transition intensity 1 3 when the **E** vector is along p_i orbital lobe and zero otherwise. The polarization averaged intensity per p_i orbital is $I = 1$ 9.

An example of XNLD for the $1s$ $2p$ transition is given in figure 2.1, which reports the N K-edge of the MnPc molecules ($\approx 0\ 6 - 1$ML) deposited on a Cu(100) surface. The measurement was done with the linear polarized X-ray beam at grazing incidence ($\theta = 70°$), with the electric field vector **E** oscillating vertically and horizontally (in-plane and out-of-plane direction with respect the sample surface) and at $T = 8K$. The two spectra have a different shape providing an indication about the orientation of

the molecule on the surface: MnPc are adsorbed flat on the Cu surface.

More generally, the intensity can be written as a function of the angle θ between **E** and the symmetry axis (labeled). The intensity has the following form

$$I(\theta) = I \ \cos^2\theta + I \ \sin^2\theta \tag{2.24}$$

The intensities I and I are determined by the projection of the charge distribution along the symmetry axis and a direction perpendicular to it. If the charge distribution has a node perpendicular to the symmetry axis, $I = 0$ and the expression of the linear dichroism intensity depends only on squared cosine. For uniaxially aligned systems the intensity varies as

$$I(\theta) = I \ \cos^2\theta = 3 \ I \ \cos^2\theta \tag{2.25}$$

A much clearer example of the search light effect is given by the XNLD in the L-edge of 1ML of CuPc deposited on Ag(100) surface. Cu in the ground state has a $3d^9$ configuration with a one hole. Cu, in this system, has a ligand field with a square planar symmetry that splits the $3d$ orbitals as shown in the sketch of fig. 2.2 (top-left). The $d_{x^2-y^2}$ orbital is half filled Exciting transitions using linear polarized photons, we could get informations about the empty orbitals. The figure also reports the experimental geometry. The beam direction forms an angle of $\theta = 70^\circ$ with respect

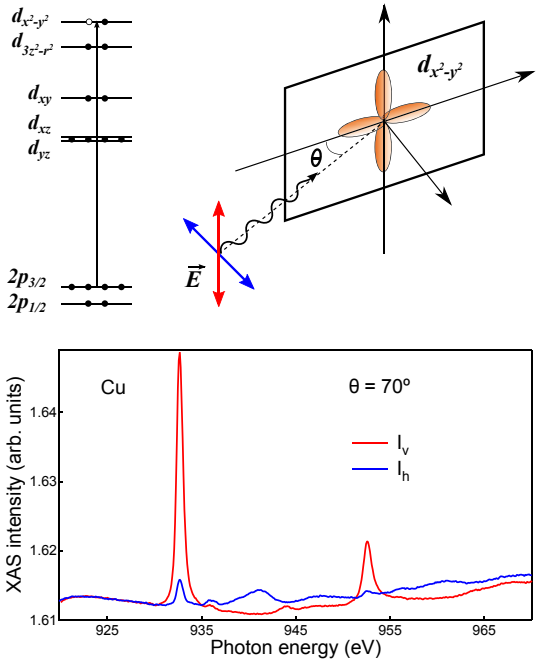

Figure 2.2: Qualitative scheme of the $2p \rightarrow 3d$ transition for $3d^9$ configuration in a square planar ligand field (top-right). Experimental geometry with linear polarized X-ray beam oriented at $\theta = 70°$ with respect the sample plane. Instead of the CuPc sample, we draw a sketch of the empty 3d orbital while red and blue arrows show the direction of oscillation of the electric field vector **E** (top-right). Linear horizontal and vertical absortpion spectra recorded at $T = 300K$ and $B = 0T$ on $L_{3\,2}$ Cu edges (bottom).

to the normal to the surface, and the electric field can oscillate in vertical or horizontal directions, probing respectively in-plane and out-of-plane empty orbitals. Figure 2.2 (bottom) reports the two recorded linear spectra: since the only empty orbital lies in-plane, only linearly vertical polarized light can excite transitions and we can clearly observe nice L_3 and L_2 peaks; horizontal light on the contrary produces a flat spectrum.

2.2 XMLD

X-ray Magnetic Linear Dichroism (XMLD) arises from non spherical distortion of the atomic charge due to spin-orbit interaction, when the spins are uniaxial alligned by exchange interaction. The intensity of this effect is proportional to the expectation value of the square of the magnetic moment and to the square cosine of the angle between electric field vector and magnetic axis. For this reason this technique is applied mainly to the characterization of antiferromagnets, where XMCD effect vanish. An example is given by the measurement of the temperature dependence in L_2 features of a NiO surface, done to prove the goodness of the substrate (figure 5.8).

2.3 XMCD

X-ray magnetic circular dichroism (XMCD) is a technique that allows to probe atomic magnetic properties using the absorption of circulary polarized X-rays. It is a powerful technique if compared with traditional magnetic characterization methods, mainly for two reasons. First, it allows element selectivity, i.e. it is possible to measure the magnetic moment of different atomic species in the same sample, just moving the photon energy in a different range. Second, XMCD allows direct and indipendent measurements of orbital (m_{orb}) and spin moments (m_{spin}), fundamental quantities for understanding the macroscopic magnetic properties of the matter: their determination with element specificity represents a tremendous advance in understanding the mechanisms underlying important technological aspects of magnetic multilayers and alloy materials.

All XMCD experiments are performed using a synchrotron radiation source, because one needs a focused beam of a defined circular polarization (right or left) and a defined energy (for studying 3d metals, for example, in the range of soft x-rays).

This technique is especially used to study magnetic properties of 3d transition metals, by exciting 2p core electrons to unfilled 3d states, or rare-earth for $3d \quad 4f$ excitations. In the case of L-edges the contribution also comes from $p \quad s$ transitions, although $p \quad d$ dominates by a factor ≈ 20: in any case, as shown below

in paragraph 2.4, sum rules take into account this contribution by subtracting a step function from the area of the sum spectrum. This is not necessary for M-edges (why? More localized 4f states, magnetic moment dominate by 4f electrons, ligand field smaller then spin-orbit and smaller then exchange and coulomb interaction then orbital moment not destroyed by ligand field in 4f shell)

In the rest of the paragraph we will treat the case of $2p \quad 3d$ transitions. It is intuitively easy to understand the basis of XMCD assuming that d shell only has spin moment. The orbital moment for transition metals is very small, quenched by the ligand field. The spin moment is just the difference between the d holes with spin-up and spin-down: in order to measure it, the absorption process needs to be spin-dependent. Since electric dipole transitions do not allow spin flips, spin-up (spin-down) photoelectrons from core shell can only be excited into spin-up (spin-down) d hole states. Using right and left circular polarized photons one can excite preferentially spin-up photoelectrons in one measurement and spin-down in the other one, and the difference in the transition intensity would reflect the difference in up and down holes in the 3d shell.

A way to describe the absorption of photons and the probing of spin and orbital moments is given by the *two step model* [77,79]. The first X-ray absorption step considers the excitation probability of the initial state, without having worrying about final state: right or left circular polarized photons transfer respectively their

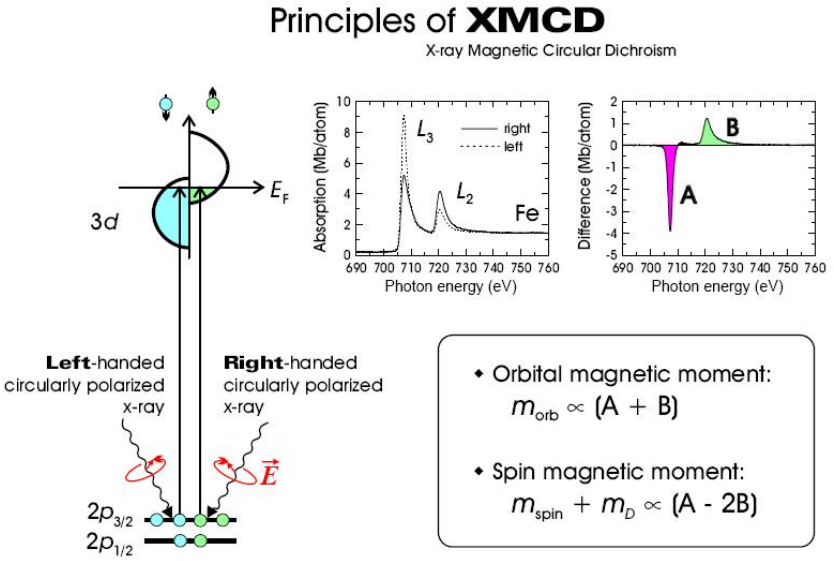

Figure 2.3: Schematic view of the XMCD technique. On the left the cartoon of the absorption process, where the imbalance of spin-up and spin-down produes a difference in the absorption spectra between photons of different polarization. The right part shows an example of measured spectra on Fe edges. The magnetic moments can be derived by integrating the difference spectrum.

angular momentum, $\hbar$ and $-\hbar$, to the excited photoelectron. If the photoelectron is excited from a spin-orbit split level, the angular momentum is trasferred in part to the spin through the spin-orbit coupling. Right circularly polarized photons transfer the opposite momentum to the electron than left circularly polarized photons, and hence photoeletrons are spin polarized. In the case of $2p \quad 3d$ transitions, p is splitted into two level with opposite spin-orbit coupling ($l + s = 3\ \ 2$ and $l - s = 1\ \ 2$) and the spin polarization will be opposite in the two cases.

The magnetic properties enter in the second step, where the spin-split valence shell acts as a detector for the excited photoelectrons. The imbalance in the spin of the photoelectrons can be thought as a probe to detect the imbalance in the final state. The quantization axis of the detector is given by the magnetization direction, which must be aligned with the photon spin direction to have maximum dichroism effect. It is worth noting that a fixed magnetization with the photon elicity changing from right to left is equivalent to a fixed helicity with the switching of the magnetization direction.

If there are more spin-up states available in the 3d band, the $q = -1$ photons will have a larger absorption in the L_2 peak than the $q = +1$ photons. The effect is opposite in sign on the L_3 edge. If we call A the L_3 absorption intensity and B the other one, the difference $A - 2B$ of the two will give a quantity proportional to the spin moment, as will be discuss in paragraph 2.4. On the other

hand, if the d valence shell possesses an orbital moment (for $3d^5$ is zero), it acts also as an orbital momentum detector: the orbital sum rule relates the sum of A and B with with the orbital moment (figure 2.3).

2.4 XMCD Sum Rules

The XMCD Sum Rules are a powerful tool that allows to determine separately the ground state orbital and spin momentum from the XMCD spectra. This work will present only the general results without entering in the details of the calculations ([83], [17])

The Sum Rules are calculated assuming:

- electric dipole transitions in multi-electron atoms with a partially filled valence shell;
- core subshell fulled in the ground state;
- core hole state spin-orbit splitted.

The first sum rule published was the one that relate the ground state orbital moment expectation value L_z to an experimental measurable quantity ρ

$$\rho \equiv \frac{\int_{edge} d \quad (\mu^+ - \mu^-)}{\int_{edge} d \quad (\mu^+ + \mu^- + \mu^0)} = \frac{1}{2} \frac{c\,(c+1) - l\,(l+1) - 2}{l\,(l+1)\,(4l+2-n)} \frac{L_z}{\hbar} \tag{2.26}$$

The $\int_{edge} d$ indicates the integration over the photon energy in the range of the $l^n \quad cl^{n+1}$ resonance edge, where n is the number of of electrons occupying the l subshell and c is the angular momentum of the core hole; $\mu^{\pm}$ is the linear absorption coefficient of the circulary polarized x-ray, μ^0 is the absorption coefficient for the linearly polarized x-ray. μ is defined by

$$\frac{I}{I_0} = e^{-\mu x} \tag{2.27}$$

where $I \; I_0$ is the fractional reduction in the intensity of the photons after they have passed through the sample and x the distance the photons have traveled through the sample. The integration over μ in 2.26 is related to the absorption intensity of polarized light $I_i^q \;_f$ (q is th photon polarization) by the

$$I_i^q \;_f = A \left| \left\langle f \left| C_q^{(1)} \right| i \right\rangle \right|^2 = \int\limits_{edge} \sigma^q d\,(\hbar \;) \quad \int\limits_{edge} \mu^q d \tag{2.28}$$

where σ is the absorption cross section per atom and $C_q^{(1)}$ is a Racah s tensor operator. μ and σ are related by $\mu = (number of atoms per unit volume)\,\sigma$.

The spin sum rule relates the measurable quantity δ to the expectation values of the ground state spin moment S_z and the magnetic dipole T_z

$$
\begin{aligned}
\delta \equiv & \frac{\int_{j_+} d \quad (\mu^+ - \mu^-) - [(c+1) \quad c] \int_{j_-} d \quad (\mu^+ - \mu^-)}{\int_{j_+ + j_-} d \quad (\mu^+ + \mu^- + \mu^0)} \\
= & \frac{l\,(l+1) - 2 - c\,(c+1)}{3c\,(4l+2-n)} \frac{S_z}{\hbar} \\
+ & \frac{l\,(l+1)\,[l\,(l+1) + 2c\,(c+1) + 4] - 3\,(c-1)^2\,(c+2)^2}{6lc\,(l+1)\,(4l+2-n)} \frac{T_z}{\hbar}
\end{aligned}
\tag{2.29}
$$

where $j_\pm$ is the spin-orbit coupling of the core hole ($c \pm 1 \;\; 2$), and the magnetic dipole term is defined as

$$
T = \sum_i \mathbf{s_i} - 3\hat{\mathbf{r}}_\mathbf{i}\,(\hat{\mathbf{r}}_\mathbf{i} \cdot \mathbf{s_i}) \tag{2.30}
$$

where $\mathbf{s_i}$ is the spin moment of the ith electron and $\hat{\mathbf{r}}_\mathbf{i}$ is the unit position vector of the electron associated with the spin moment $\mathbf{s_i}$.

It is very important to underline that we can obtain the orbital moment sum rule without considering the spin-orbit interaction because the electrical field of the photon directly interacts with the orbital angular moment. This is not true for the spin moment, because of the selection rule $\Delta S = 0$ of dipole transitions. In this case we have to take into account the spin-orbit interaction: the spin angular momentum interacts indirectly with photon electric field through this one.

2.4.1 XMCD Sum Rules for 2p 3d transitions in 3d transitions metal elements

From the general Sum Rules (2.26 and 2.30) we can calculate the expression for the L edges of transition metals. This section will show how to apply the Sum Rules to Fe spectra measured in transmission.

Orbital moment sum rule

The equation 2.26 can be written in the case of 2p 3d transitions for 3d metals, considering $l = 2$ and $c = 1$

$$\rho = \frac{\int_{L_3+L_2} d \quad (\mu^+ - \mu^-)}{\int_{L_3+L_2} d \quad (\mu^+ + \mu^- + \mu^0)} = -\frac{1}{2N}\frac{m_{orb}}{\mu_B} \tag{2.31}$$

where m_{orb} is the ground state orbital magnetic moment and $N \equiv (4l + 2 - n)$ is the number of holes in the 3d shell at ground state. In experiments, the integral that appears at the denominator, $\int_{edge} d \quad \left(\mu^+ + \mu^- + \mu^0\right)$, is approximated by

$$\int_{edge} d \quad \left(\mu^+ + \mu^- + \mu^0\right) \approx \frac{3}{2} \int_{edge} d \quad \left(\mu^+ + \mu^-\right) \tag{2.32}$$

so, the equation becomes

$$m_{orb} = -\frac{4}{3}\frac{\int_{L_3+L_2} d \quad (\mu^+ - \mu^-)}{\int_{L_3+L_2} d \quad (\mu^+ + \mu^-)} N\mu_B \tag{2.33}$$

Spin moment sum rule

The spin moment sum rule can also be re-written for 3d metals

$$\begin{aligned}\delta &= \frac{\int_{L_3} d \quad (\mu^+ - \mu^-) - 2\int_{L_2} d \quad (\mu^+ - \mu^-)}{\int_{L_3+L_2} d \quad (\mu^+ + \mu^- + \mu^0)} \\ &= -\frac{1}{3N}\frac{m_{spin}}{\mu_B}\left(1 + \frac{7}{2}\frac{T_z}{S_z}\right) \end{aligned} \tag{2.34}$$

Applying the same approximation that we use before for the denominator and neglecting the ratio $\frac{T_z}{S_z}$

$$m_{spin} = -\frac{2\int_{L_3} d \quad (\mu^+ - \mu^-) - 4\int_{L_2} d \quad (\mu^+ - \mu^-)}{\int_{L3+L_2} d \quad (\mu^+ + \mu^-)} N\mu_B \tag{2.35}$$

2.4.2 XMCD Sum Rules for 3d 4f transitions in rare-earth elements

It is also possible to find, from general equations 2.26 and 2.30, the sum rules for M-edges in the case of $3d$ $4f$ transitions, considering $c = 2$ and $l = 3$.

Orbital moment sum rule

The orbital moment sum rule for rare-earths becomes

$$\rho = \frac{\int_{M_5+M_4} d \quad (\mu^+ - \mu^-)}{\int_{M_5+M_4} d \quad (\mu^+ + \mu^- + \mu^0)} = -\frac{1}{3N}\frac{m_{orb}}{\mu_B} \tag{2.36}$$

Spin moment sum rule

The spin moment sum rule is

$$\begin{aligned} \delta &= \frac{\int_{M_5} d \quad (\mu^+ - \mu^-) - \frac{3}{2}\int_{M_4} d \quad (\mu^+ - \mu^-)}{\int_{M_5+M_4} d \quad (\mu^+ + \mu^- + \mu^0)} \\ &= -\frac{1}{3N}\frac{m_{spin}}{\mu_B}\left(1 + 3\frac{T_z}{S_z}\right) \end{aligned} \tag{2.37}$$

In the case of rare-earth, the magnetic dipole term T_z can be evaluated analytically and has the form

$$\begin{aligned} T_z &= M\left(l - n + \frac{1}{2}\right)\cdot \\ &\cdot\left(\frac{3\left(S-J\right)^2\left(S+J+1\right)^2}{2\left(2l+3\right)\left(2l-1\right)\left(2L-1\right)SJ\left(J+1\right)} + \right. \\ &\left. -\frac{L\left(L+1\right)\left[L\left(L+1\right)2S\left(S+1\right)+2J\left(J+1\right)\right]}{2\left(2l+3\right)\left(2l-1\right)\left(2L-1\right)SJ\left(J+1\right)}\right) \end{aligned} \tag{2.38}$$

for $n \leqslant 2l{+}1$. The case $n \geqslant 2l{+}1$ is accounted for by $n \quad 4l{+}2{-}n$.

2.5 Experimental concepts of XAS

There are in general three main ways (figure 2.4) to measure XAS spectra: transmission (direct way), fluorescence and electron yield (indirect ways). In this section the attention will be put on transmission and electron yield measurements, the main ways to obtain XAS spectra for $L_{3,2}$ of 3d metals.

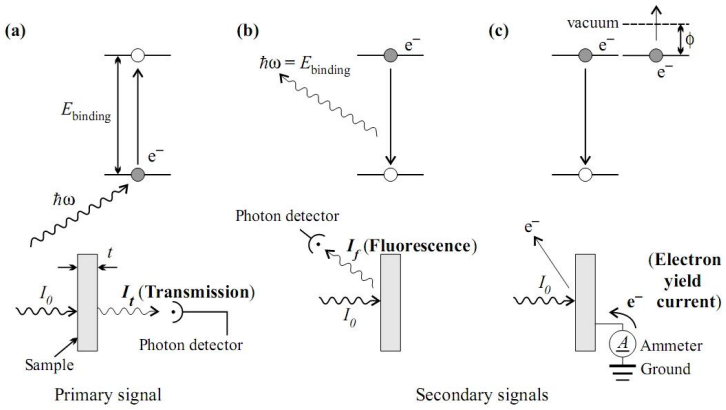

Figure 2.4: Methods of obtaining X-ray absorption signals: transmission (a), fluorescence (b) and electron yield (c).

2.5.1 Transmission

Transmission is the direct way to quantify the x-ray absorption. In fact one measures the transmitted intensity after the beam have passed through the sample and the incident flux has been partially absorbed. Equation 2.27 relates the linear absorption coefficient and the measured photon intensity. In theory, this is the best way to mesure absorption spectra but there is a main limitation (also called saturation effect): the transmitted intensity I. If the sample is too thick or the absorption rate is too high, the photon intensity I 0. In practice, one needs a reasonably thin sample (around 50Åfor many 3d metals like Fe) and also an exstreamly thin substrate made by an x-ray transparent material (like pary-

lene).

2.5.2 Total Electron Yield

A second way to measure the cross section is the electron yield method. When a photon is absorbed an electron is exited to an higher energy level. At this point there is a certain probability that some electrons are emitted by the transfer of energy, released by the relaxation of the excited electron, to another electron (Auger process). These Auger electrons have high kinetic energy and they often produce a cascade of secondary electrons by inelastic scattering. The total electron yield measures the rate of these secondary electrons, that under certain conditions could be approximately considered proportional to the absorption cross section σ.

Without entering too much in the details of the theory, we can express the electron yield current as

$$i_{EY} = I_0 G \frac{\mu\lambda_e}{\cos\theta} \frac{1}{1 + \mu\lambda_e \ \cos\theta} \tag{2.39}$$

where I_0 is the initial photon intensity, G the empirical multiplication factor proportional to $\hbar$, μ the linear absorption coefficient, θ is the x-ray incidence angle and λ_e the electron escape depth, i.e. the maximum average distance that an electron could cover through the sample before escaping. In the limit of small $\mu\lambda_e \ \cos\theta$ the equation become

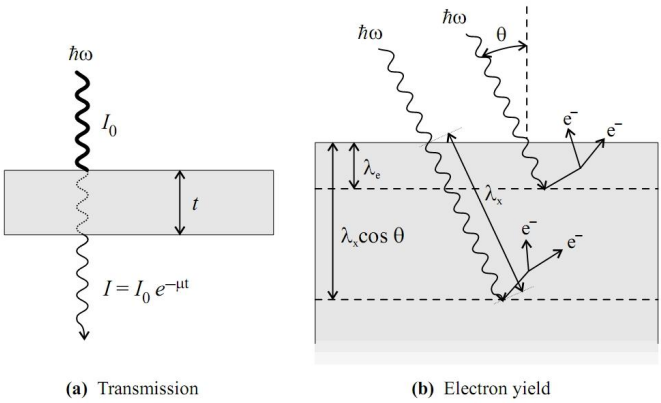

Figure 2.5: Qualitative description of transmission and electron yield methods of X-ray absorption measurements. In transmission measurements the photon intensity I after transmission through the sample of thickness t, is compared with respect to the initial intensity I_0 (a). In the electron yield method, the atoms, after the absorption of a photon, have a certain probability to produce Auger electrons

$$\lim_{\mu\lambda_e \to 0} i_{EY} = I_0 G \frac{\mu\lambda_e}{\cos\theta} \tag{2.40}$$

In this case, the electron yield signal is directly proportional to μ. By trying to understand more this approximation, one could introduce the x-ray penetration length λ_x(or attenuation length), which is the inverse of the absorption coefficient ($\mu = 1 \ \lambda_x$) and the penetration depth $\lambda_x \ \cos\theta$ (figure 2.5). The condition $\mu\lambda_e \ \cos\theta \quad 0$ means that $\lambda_e << \lambda_x$, i.e. the major part of Auger electrons cannot escape and produce secondary electrons. Saturation effects in the electron yield method are reached when the linear proportionality is lost: this happens when λ_e is comparable or higher than λ_x, i.e. when most of the electrons can escape and the production of secondary electrons fall down.

With respect to the transmissions measurements there are no particular restrictions in the thickness of the sample, but from an experimental point of view it is better to put a capping layer on the top to prevent oxidation. The best choice is to find a material with a small x-ray absorption to minimize the background signal. Possible materials are Au, Ru, Cu and C for the $500 - 1000$eV range of energy. The sample have also to be conductive, so that it is possible measure a current when it is grounded.

2.5.3 Fluorescence

The fluorescence yield is the second indirect way to measure x-ray absorption. It is not very much used for the $L_{3,2}$ edges of 3d metals because it constitutes less then 1% of the secondary signal, and also because the signal does not quantitatively follow the true absorption signal. This is due to the fact that the excitation is proportional to the absorption, but the emission of the fluorescence comes from a state that is different from the ground one.

2.6 Application of the sum rules to Fe XMCD spectra measured in transmission

This section presents the application of the XMCD sum rules to real measurements recently performed by us at the SIM beamline of the Swiss Light Source (SLS) (Paul Scherrer Institute, Villigen, Switzerland).

Figure 2.6 shows the experimental set-up and a sketch of the sample. A magnetic field of up to 0,8T produced by an electromagnet is applied parallel to the x-ray beam to saturate the magnetization along the photon polarization direction. The x-ray beam passes through one pole of the magnet and hits the sample at normal incidence. The samples are fabricated by sputtering on a silicon nitride silicon window (Silson Ltd., England). The win-

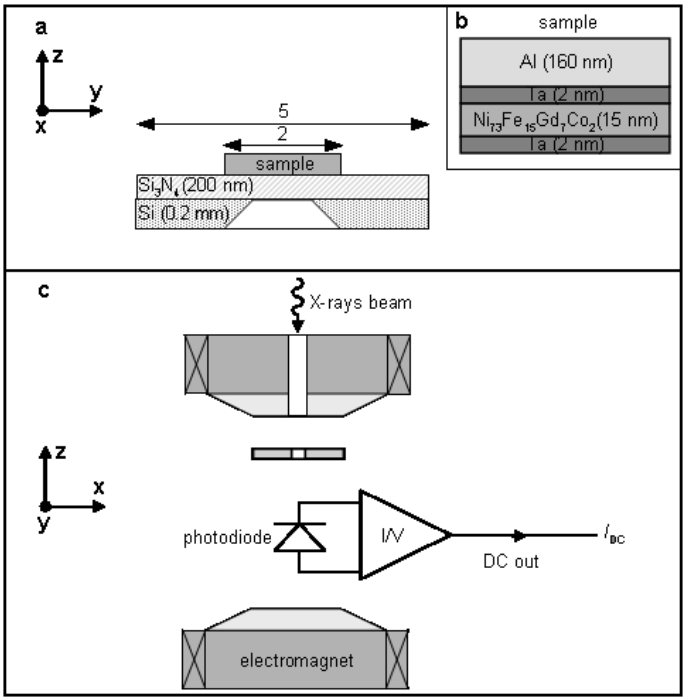

Figure 2.6: Experimental set-up. Sample on a silicon nitride silicon window (a) and in the inset (b) the different layers. Below the geometry of the experiment, with the x-ray beam, the sample and the photodiode placed inside the magnet (c).

dow consists of a Si_3N_4 membrane supported by a Si frame. The polycrystalline sample measured in this paper consists of Al(160 nm) Ta(2 nm) $Ni_{73}Fe_{18}Gd_7Co_2$(15 nm) Ta(2 nm) Si_3N_4(200 nm). The Al top layer improves the thermal conduction and the mechanical stability of the membrane, while the Ta layer is used to improve the adhesion. The transmission in the range 700 eV to 900 eV of each layer is approximately: Al (90%), Ta (95%), $Ni_{73}Fe_{18}Gd_7Co_2$ (90%), Si_3N_4 (75%), giving a total transmission larger than 50%.

Figure 2.7a shows the transmission spectra (left and right polarization) of Fe in doped permalloy ($Ni_{73}Fe_{18}Gd_7Co_2$) measured in current units by the photodiode placed behind the sample. From these spectra one can calculate the relatives absorption cross sections (figure 2.7b) just using the equation

$$\mu_{\pm} \quad -\log\left[I_{\pm}(\ )\ \ I_s(\ )\right] \tag{2.41}$$

where I_s is the background intensity due to the substrate. By adding and subtracting the absorption, one obtains the sum (figure 2.7c) and the XMCD (figure 2.7d) spectra: in the first one the dotted line shown is the two-step-like function for edge jumps removal before the integration, while r is the value of the integrated area of the sum spectra minus the edge jump area. All integrals are calculated using the trapezoidal method. In the case of the XMCD spectrum, p is the integral of the L_3 edge contribution, while q is the integral over the whole energy range (2.7d).

Applying equations 2.33 and 2.34 one finds

$$m_{orb} = -4qN\ 3r = (0\ 117 \pm 0\ 002)\mu_B \quad (2.42)$$

$$m_{spin} = -(6p - 4q) \cdot N\ r = (2\ 451 \pm 0\ 004)\mu_B \quad (2.43)$$

The results are close to the values that one finds in the literature (see table 2.1), but it is unexpected that the ratio is closed to the value of bulk Fe (bcc) [18], while the values of the single moments are more similar to calculated permalloy [89]. The number of holes N is taken equal to 3 4 as found in literature [78].

	m_{tot}	m_{spin}	m_{orb}	$m_{orb}\ m_{spin}$
Fe (bcc)	2,07	1,98	0,085	0,043
Fe in $Ni_{80}Fe_{20}$	2,644	2,59	0,054	0,021
Fe (our)	2,568	2,451	0,117	0,048

Table 2.1: Spin and orbital moments in Fe bulk [18] and permalloy [89]. The moments are given in units of μ_B per atom.

2.7 Experimental set-up

The experiments presented in the following chapters were performed at the ID08 beamline of the European Synchrotron Radiation Facilities (ESRF) in Grenoble. Figure 2.8 shows a schematic view of the entire end station. Sample preparation was reproduced

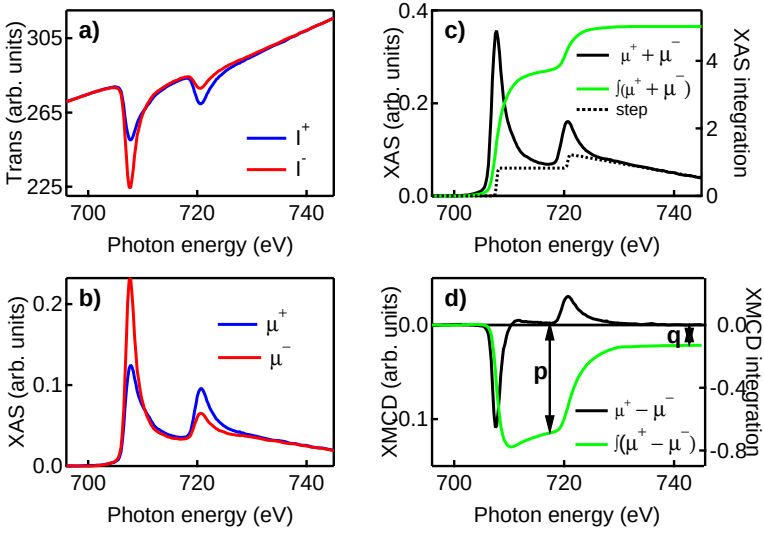

Figure 2.7: Fe in doped permalloy $Ni_{73}Fe_{18}Gd_7Co_2$. Transmission x-ray absorption spectra taken with right and left polarized light (a). Absorption cross sections derived from the transmission spectra (b). Sum spectrum of the two cross sections and integration spectrum of the difference between the sum and the step function. XMCD spectrum with the relative integration (d).

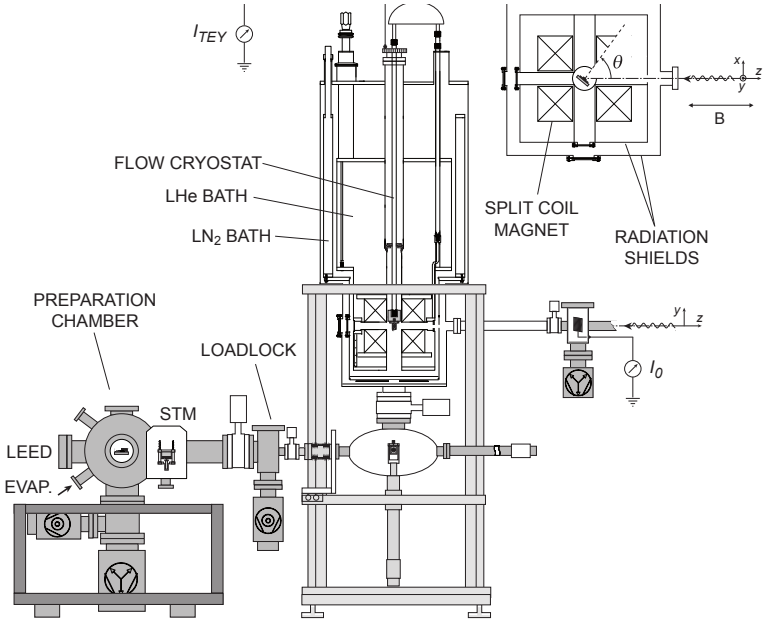

Figure 2.8: Scheme of the end-station at the ID08 beamline of the ESRF. In the top part on the right, the view from above of the XMCD chamber with the experimental geometry is presented.

in situ in a dedicated prep-chamber. We clean our Cu(100) and Ag(100) single crystal substrate surfaces by mean of Ar^+ sputtering and annealing cycles. Thin metallic (mainly 3d transition metals like Ni, Co or Mn) or oxide (NiO, CoO and MnO) films were deposited by e-beam evaporation, while Me-Pc or $TbPc_2$ were evaporated by molecular-beam epitaxy using a Knudsen Cell. The base pression was around 5*10−10 mbar. LEED and STM were used to check the cleaning of the single crystals, to verify the goodness of thin films growth and the precence of molecules on the surfaces and avoid to pass the limit of 1ML. After that the samples were transfered without breaking the ultra high vacuum to the XMCD end station. As we see in the figure, the sample holder is screwed to a cold-finger directly conneted to the cryostat and we can flow liquide He to cool down the sample till a temperature around 7-8K (the measured temperature is lower, but since the thermocouple is not close to the sample holder, we made an estimation). The pressure in the XMCD chamber is close to 1*10−10, but it went down when we cooled down the sample, since the free atoms in the chamber tend to stick to the walls. The beamline provides a 99% of polarization for both circular and linear polarized light and a range of energies between $0\ \ 4-1\ \ 5$KeV with a resulution of $\Delta E = 5 * 10^{-10}$ at 850eV; this range is ideal for studying magnetic properties of transition metals and rare earths. Spectra are recorded in Total Electron Yield (TEY) mode, measuring the I_{TEY} current due to the emitted electron of the sample surface.

Right before the chamber the beam hit a gold grid that provides the reference signal I_0 used for normalize the spectra. Inside the XMCD chamber, there is a superconducting split coil magnet that gives a field till ± 5T collinear with the beam direction. In the inset on the right, the top view of the chamber is presented: the beam is along the **z** axis as the magnetic field, and it forms an angle θ with the normal to the sample surface. $\theta = 0°$ will correspond to the normal incidence while $\theta = 70°$ to the grazing one. The maximum sample rotation we can reach is 180°. Spectra recorded with circularly polarized light with photon helicity parallel and antiparallel to **B** are indicated as I^+ and I^-, respectively. The XMCD signal is defined as $I^- - I^+$. In order to check the anisotropy of the molecules and of the thin films we used also linear polarized light, with **E** along **y** and **x**, in order to probe in plane and nearly out of plane directions, when $\theta = 70°$.

Chapter 3

Coupling of Single Molecule Magnets to ferromagnetic substrates

In this chapter we investigate the interaction of $TbPc_2$ single molecule magnet (SMM) with ferromagnetic Ni surfaces. The first paragraph (3.1) gives a brief overview on SMM, underlining the main properties and focuses the attention on $TbPc_2$, while paragraph 3.2 presents the measurements done by depositing this molecule on ferromagnetic Ni surfaces, the data analysis, and the interpretation of the results.

3.1 Single Molecule Magnets

3.1.1 General properties

Single Molecule Magnets (SMMs) are a class of magnetic metal-organic molecules that show slow relaxation of the magnetization at low temperature. These compounds have been intensively studied so far because of their potential technological applications in fields like magnetic recording and spintronics, by considering the molecules as single magnetic units and therefore possible building blocks for future devices.

Below the so called *blocking temperature* (T_B), SMMs behave like a nanomagnet and give rise to magnetic hysteresis of purely molecular origin [73].

SMMs are usually made by a core of transition metal ions surrounded by organic ligands. These ions are strongly coupled through superexchange interaction that gives rise to a high spin ground state, and for this reason they can be described by an effective spin Hamiltonian, in which isotropic exchange is the leading term

$$H_{ex} = \sum_{i>j} J_{ij} \mathbf{S_i} \cdot \mathbf{S_j} \tag{3.1}$$

where i and j run over all metal sites of the cluster. The occurrence of a large spin ground state is a necessary, although not sufficient, condition to observe slow relaxation of the magnetization. The second requirement is to have a large magnetic anisotropy, that in

SMMs mainly comes from magnetocrystalline contributions due to the low-symmetry environment around the metal centers of the molecule. For a system with no symmetry at all, using the spin-Hamiltonian treatment commonly used to describe SMMs, this anisotropy is given by

$$H_{an} = \mathbf{S} \cdot \mathbf{D} \cdot \mathbf{S} = D\left[S_z^2 - \frac{1}{3}S\left(S+1\right)\right] + E\left(S_x^2 - S_y^2\right) \qquad (3.2)$$

where D represents the axial anisotropy and E the transverse one. The effect of the anisotropy on the $(2S+1)$ states of the spin multiplet is the removed of their degeneration even in the absence of an external magnetic field, namely a zero-field splitting of the levels. The anisotropy energy associated to a SMM system is the energy gap in zero field between the largest and smallest m , where m is an eigenvalue of S_z. In the case of pure axial anisotropy ($E = 0$) the gap corresponds respectively to $D\ S^2$ for integer and $D\ \left(S^2 - 1\ 4\right)$ and half-integer. A system showing easy axis magnetic anisotropy state has a ground doublet characterized by $m = \pm S$, which corresponds to two potential wells separated by an energy barrier. When a magnetic field is applied, the degeneracy is removed and one of the wells is populated; removing the field the system returns back to equilibrium through multi-step Orbach processes. SMMs are usually described by adopting the giant spin approximation: at low temperature only the ground spin state is populated, and the dynamics of the magnetization is in first approximation well rationalized, assuming that the whole

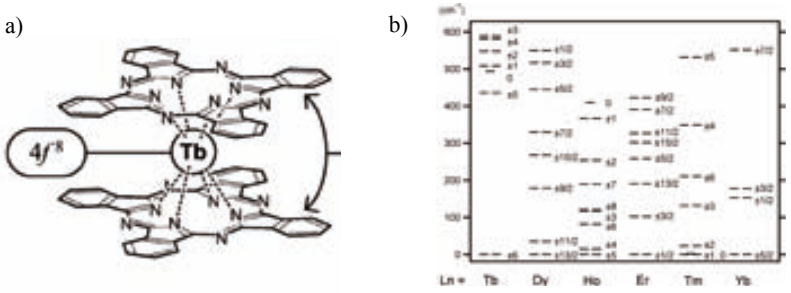

Figure 3.1: (a) Cartoon of the $TbPc_2$ molecule. (b) Enery level spliting for $LnPc_2$ complexes.

molecule behaves like a unique large spin characterized by its axial and transverse anisotropies.

(quantum tunneling of the magnetization - how explain in few words?)

The great limit of the properties of these molecules is the temperature: for transition metal SMMs the blocking temperatures T_B are close to liquid He ones. It should also be stressed the fact that T_B is not a constant but depends mainly on the time-scale of the measurements: the faster we measure, the slower the magnetization relax and the higher is the T_B.

3.1.2 Lanthanide complexes: $TbPc_2$

Among the SMMs there is a particular class of compounds, the lanthanide bis(phtalocyanines) complexes, that present similar prop-

erties to those of transition metals ones despite the different structure. These are mononuclear molecules, with a rare earth atom lying between two phthalocyanine, one on the top and the other one on the bottom, as shown in figure 3.1. From AC susceptibilities measurements, it was shown that only $TbPc_2$ and $DyPc_2$ present slow relaxation of the magnetization, while the other lanthanide complexes did not [36]. These two molecules present a high spin ground state and a large zero field splitting, like polynuclear SMMs, but its origin is different and it does not come from exchange interaction between the spins of the metal ions. In this case, the ligand field potential is splitting the ground multiplet so that the lowest sublevel has the largest J_z value (for Tb $J_z = 6$) and a large energy gap arises with respect the rest of the sublevels (Fig. 3.1). This unusual condition leads to a small probability of transition and hence to a slow magnetization relaxation [39].

In this paragraph, the attention is drawn on $TbPc_2$, because it presents a higher energy gap between ground state and the excited ones ($\approx$50 meV), as well as a higher blocking temperature with respect to $DyPc_2$. T_B depends on the time scale of the measurements, the dilution of the molecules and the amount of charge of the molecule. Ishikawa *et al.* [36] clearly showed, by using AC susceptibilities measurements, that the peak in the θ''_M in correspondence of T_B, shifts toward higher temperatures if we increase the frequency (from 15 K to 40 K if the AC frequency changes from 10 to 1000 Hz). We can also observe a small increase of T_B

if the molecules are isolated and do not interact with each other. In a powder this was achieved by diluting $TbPc_2$ with diamagnetic YPc_2 molecules. Moreover, it was also shown that if we measure the neutral $[TbPc_2]^0$, which has an open π shell delocalized on the ligand with a $S = 1\ 2$ spin, T_B rises, reaching 36 to 50 K for a frequency between 10 Hz and 1 kHz, i.e., higher values then the results obtained on $[TbPc_2]^-$ [37].

Magnetization loops have been measured to check the presence of a hysteretic behaviour, sign of magnetic bistability of mononuclear SMMs. The loop presents the so-called butterfly shape (Fig. 3.2 (a)), with two different trends depending on the strength of the magnetic field: for $B > 0\ 1$ the decrease of the magnetization with decreasing the field is relatively small, while for $B < 0\ 1$ we can observe a sharp drop. The molecule seem to relax faster at low fields.

The characteristic step structure in $TbPc_2$ did not show to be caused by resonant tunneling processes, at $T = 1\ 7K$ because the energy separation between the ground and the first excited level is higher then the energies that could be reached in this range of fields by Zeeman interaction ($B < 1\ 6T$) [37]. Surprisingly measurements taken at $T = 0\ 04K$ present a characteristic staircase structure at very low fields ($B < 0\ 05T$). The steps observed for $TbPc_2$ must therefore be caused bt a different mechanism. Taking into account the hyperfine interaction term $A_{hf}\mathbf{J} \cdot \mathbf{I}$ and the nuclear quadrupole interaction term $P\left[I_z^2 - 1\ 3I\left(I+1\right)\right]$, one

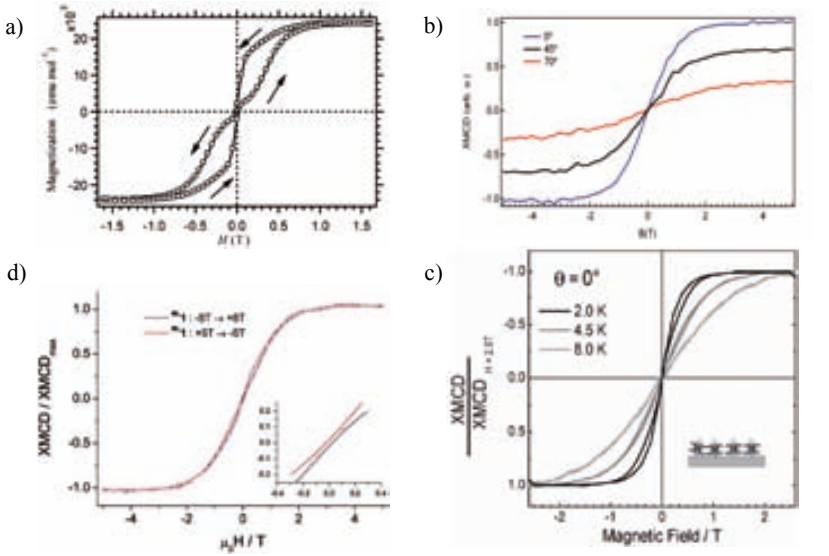

Figure 3.2: $TbPc_2$ hysteresis loops recorded (a) in the powder sample or when the molecule is deposited (b) on Cu(111), (c) on Au(111), (d) on highly oriented pyrolitic graphite (HOPG).

can obtain the Zeeman diagram by numerical diagonalization of a $[(2J+1)(2I+1) \times (2J+1)(2I+1)]$ matrix for the states generated from $J = 6$ electronic multiplet and $I = 3/2$ nuclear multiplet. All positions of the steps in the loop are reproduced by the diagram [35].

Since $TbPc_2$ shows these interesting magnetic properties, it is crucial to deposit this molecule on a surface and try to control its properties: this is the first step required towards the engi-

neering of molecule-based magneto-electronic devices. $TbPc_2$ was first deposited on Cu(111) using a dry imprint technique, and it was studied by Scanning Tunneling Microscopy (STM), Scanning Tunneling Spectroscopy (STS) and Density Functional Theory (DFT) [87]. It was demonstrated that the molecules structure does not change significantly by interacting with the substrate: the $4f^8$ electron states responsible for the large magnetic moment, are not much affected by the interaction with the substrate. Furthermore, it was also shown that $TbPc_2$ could be deposited by thermal evaporation in UHV condition on metallic surfaces, like Cu(111) [76] or Au(111) [51], without loosing their molecular integrity. $TbPc_2$ adsorbs flat (or with a small angle distribution) on these surfaces, with the easy axis of the molecule perpendicular to the substrate plane, as measured by STM and X-ray linear dichroism. By comparing the shape of the XAS spectra with the calculated ones, it was shown that the molecules did not loose their $4f^8$ configuration, with a $J = 6$ ground state ($L = S = 3$). The unchanged shape of the XMCD spectra varying the angle and the fact that the intensity of this peak scales as $\cos\theta$, suggest that the Tb magnetic moment has an Ising-like behaviour, showing a spin parallel or antiparallel to the normal to the surface, depending on the direction of the applied magnetic field. On both Cu and Ag samples magnetization curves measured by XMCD presented closed loops at $T = 8K$ (Fig. 3.2 (b),(c)), with a typical paramagnetic S-shape. For molecules on Au(111), an open curves was

measured, but only for temperatures lower then 5 K. On the contrary, open hysteresis loops were measured at 7 K for molecules deposited in air onto a freshly cleaved highly oriented pyrolitic graphite (HOPG) (Fig.Figure 3.2 (d)), casting a drop of a 10^{-6} M solution of acetal protected $TbPc_2$ [32]. The butterfly loop shown at higher temperatures could be the result of the different deposition technique or, most likely, it could be due to the change made on the Pc ligand. We do not believe we can ascribe this different magnetic behaviour to the HOPG substrate.

3.2 $TbPc_2$ on Ni substrates: experimental results

As described in paragraph 3.1.2, $TbPc_2$ presents the highest T_B among SMM, it adsorb flat on surfaces and, since is a mononuclear complex, it is in principle an easy system to study compared with 3d transition−metal SMMs. In order to try to stabilize the magnetic moment of the molecule, different strategies can be adopted. The efforts to slow down magnetic relaxation in SMM have thus far relied on the synthesis of polynuclear molecules with a large number of metal ions [47, 76] or on modifying the ligand field strength in order to enhance the magnetic anisotropy energy barriers [81]. These approaches have been moderately successful. For example, ligand oxidation of $TbPc_2$ has been shown to increase τ from about 10^{-4} to 10^{-3} s at $T = 40$ K [39]. Recently, however, an

alternative strategy has been proposed to stabilize the magnetic moment of paramagnetic molecules against thermal fluctuations [8, 34, 42, 68, 80, 88, 90]. This approach is based on the deposition of planar complexes such as metal-porphyrins and phthalocyanines on ferromagnetic (FM) films. Because of the close proximity to the substrate, the magnetic moment of the metal ions embedded in the plane of such molecules can efficiently couple to the surface magnetization via superexchange and direct exchange paths [8,34,42,90]. Although individual molecules cannot be addressed independently, this approach enables the fabrication of metal-organic layers with stable magnetization up to room temperature [8, 68, 88]. Therefore ultrathin FM molecular layers may be employed in hybrid spin valve structures [12] or as magnetochemical sensors [88].

3.2.1 Sample preparation

The samples were prepared in-situ by molecular beam evaporation of $TbPc_2$ on Ni films in ultra-high-vacuum in a dedicated set-up as described in paragraph 2.7. The $TbPc_2$ coverage was about 0.05 monolayers (ML). FM films with out-of-plane (OP) and in-plane (IP) magnetic anisotropy were obtained by deposition of 13 ML of Ni on Cu(100) and 6 ML of Ni on Ag(100) sputter-annealed single crystals, respectively [33, 71]. Oxidized and reduced Ni surfaces with OP magnetization were prepared by O surfactant growth of Ni on Cu(100) [61] and by evaporating Li on Ni/Cu(100). X-ray absorption spectra (XAS) of N and Tb presented strong linear

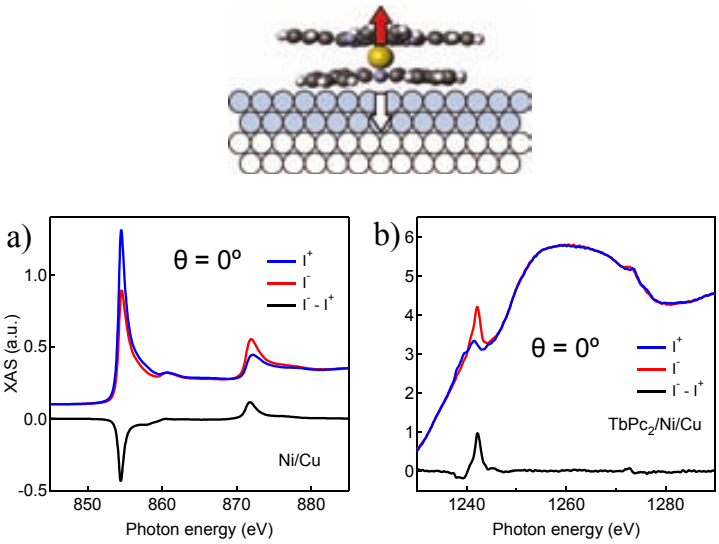

Figure 3.3: (a) Schematic view of $TbPc_2$ on OP Ni/Cu(100). (b) XAS spectra measured at the $L_{2\,3}$ edges of Ni and (c) $M_{4\,5}$ edges of Tb for $TbPc_2$/Ni/Cu(100). The plot show the spectra with positive (I^+) and negative (I^-) circular polarization and the XMCD intensity ($I^- - I^+$) measured at 8 K in remanence. Due to the low $TbPc_2$ coverage, the Tb XAS is superimposed to a strong substrate-dependent background intensity. Such background does not contribute to the XMCD.

dichroism, indicating that the molecules are oriented with the Pc plane parallel to the Ni surface and easy axis perpendicular to it, in agreement with previous measurements of $TbPc_2$ on Cu(100) [76, 87].

3.2.2 Coupling of $TbPc_2$ to Ni substrates

We begin by investigating the coupling of $TbPc_2$ to OP Ni films at remanence. In such a case, the molecule and substrate easy axes are collinear. Figure 3.3 (a), (b) shows the Ni and Tb XAS and XMCD spectra recorded at $T = 8$ K after saturating the magnetization at 5 T along the film normal, and subsequently setting the field to zero. We observe that both Ni and Tb have a strong remanent XMCD intensity, which remains stable over the timescale of the measurements. The sign of the Tb XMCD, however, is opposite with respect to Ni, indicating that $\mathbf{M}_{\mathrm{Tb}}$ and $\mathbf{M}_{\mathrm{Ni}}$ are antiferromagnetically (AFM) coupled.

Element-resolved hysteresis loops provide further insight into the the nature of SMM-substrate coupling. The magnetization curves are measured by recording the peak XMCD intensity at 854.5 (1242.5) eV for Ni (Tb) as a function of applied field. There are different ways to perform such a measurement. The first one is to measure pairs of I^+ and I^- spectra at each field. This is extremely time-consuming for dilute samples, as a single pair of spectra does not provide enough signal-to-noise ratio. Moreover, the need to reverse the photon polarization at each field increases the measuring time considerably. The second method consists in performing two sweeps of the applied magnetic field, one for positive and the other for negative circularly polarized light. During each sweep, only the pre-edge intensity at 845 (1230) eV and the

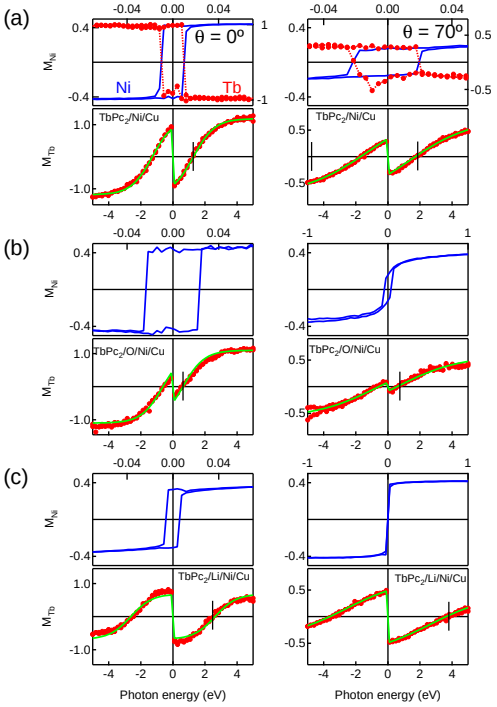

Figure 3.4: Element-resolved hysteresis loops of Ni (top) and Tb (bottom) for (a) $TbPc_2$/Ni/Cu(100), (b) $TbPc_2$/O/Ni/Cu(100) and (c) $TbPc_2$/Li/Ni/Cu(100) measured in normal (left) and grazing (right) incidence at $T = 8$ K. The units of $\mathbf{M}_{\mathrm{Ni}}$ and $\mathbf{M}_{\mathrm{Tb}}$ correspond to the XMCD intensity at the L_3 and M_5 absorption edges (see Fig. 3.3). The solid lines are fits to the data according to Eq. 3.3.

L_3 (M_5) peak intensity at 854.5 (1242.5) eV for Ni (Tb) are measured, thus optimizing the acquisition time for the energy point

where the XMCD is maximum. The peak intensity values are divided by the pre-edge intensity at each field in order to eliminate the dependence of the electron yield on the sample orientation and magnetic field. Finally, the normalized intensity from the first loop is subtracted from the second in order to obtain the XMCD intensity. This is a well-established method to measure magnetization curves using XMCD [25, 27, 31], which gives better results than just plotting the peak intensity as a function of field as done for relatively thick metal films [24]. The curves shown in Fig. 3.4 have been obtained in this way. In order to define a common intensity scale, we have scaled each curve so that the intensity at 5 T matches the XMCD/XAS ratio obtained from the spectra at the same field. This procedure has no influence on the fits of the magnetization curves, since the saturation magnetization is a free parameter of each fit.

We recall here that the XMCD/XAS asymmetry is a self-consistent quantity that can be related to the atomic magnetic moment of the element under investigation. This ratio, defined as $(I^- - I^+)\ [(I^+ + I^-)\ 2]$, can be calculated by integrating whole spectra or part of the spectra, or by taking the ratio of the peak XMCD and XAS intensity at the L_3 (M_5) peaks, where the XMCD is maximum. These two methods are equivalent as long as the XMCD lineshape does not change with applied magnetic field, which is practically always the case as the Zeeman splitting is small with respect to the atomic level spacing due to electron-electron

interactions, crystal field, and charge transfer effects. The peak intensity method works better for dilute samples, since it reduces errors due to the integration of noise in the XMCD baseline and does not require the subtraction of background XAS spectra.

Figure 3.4 (a) shows the out-of-plane ($\theta = 0°$) and in-plane ($\theta = 70°$) magnetization loops of the OP $TbPc_2$/Ni/Cu(100) sample measured by recording the XMCD intensity at the Ni L_3 and Tb M_5 edge as a function of applied field. In the low field region, $\mathbf{M}_{\mathrm{Tb}}$ is aligned antiparallel to the $\mathbf{M}_{\mathrm{Ni}}$, switching direction together with it. However, at higher field, the Zeeman interaction overcomes AFM exchange, inducing a gradual rotation of $\mathbf{M}_{\mathrm{Tb}}$ parallel to $\mathbf{B}$. $\mathbf{M}_{\mathrm{Tb}}$ first changes sign at $B_{exc} = 1\ 2T$, as the external field compensates the exchange coupling to the substrate, and finally ends up parallel to $\mathbf{M}_{\mathrm{Ni}}$. A similar behavior is observed for out-of-plane and in-plane loops, albeit the Tb remanence, B_{exc}, and the magnetization at high-field depend on the orientation of $\mathbf{B}$ with respect to the SMM easy axis.

3.2.3 Tuning the coupling

As the coupling between $\mathbf{M}_{\mathrm{Tb}}$ and $\mathbf{M}_{\mathrm{Ni}}$ is necessarily mediated by the bottom Pc ligand of $TbPc_2$, we tested the possibility of tuning the exchange interaction by modifying the amount of charge transfer between surface and molecule. This can be realized in practice by i) preparing a (2×2) O buffer layer [61] between $TbPc_2$ and Ni, and ii) doping the Ni surface with a strong electron donor such

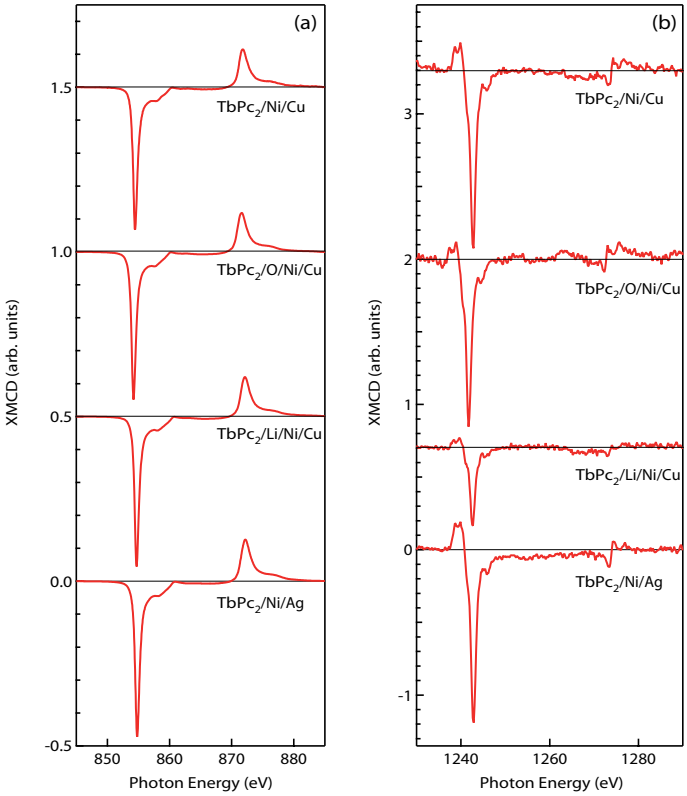

Figure 3.5: (a) Comparison of the Ni XMCD spectra obtained at $B = 5$ T, $T = 8$ K, and $\theta = 0°$ for different substrates. (b) Same for the Tb spectra. The vertical units represent the XMCD/XAS ratio at the L_3 (M_5) edge of Ni (Tb).

as Li. Although we do not control the extent of charge transfer in either case, it is safe to assume that it leads to i) oxidation and ii) a reduction of the Pc ligand.

The effects of charge transfer on the Ni magnetization reported in Fig. 3.4 (b) and (c) are limited to variations of the coercivity, which we ascribe to modifications of the surface magnetocrystalline anisotropy energy. To confirm this deduction, we compare the XMCD spectra of our four samples, since the lineshape is very sensitive to changes of the electronic and magnetic ground state of metal ions [28, 30, 84, 86]. Figure 3.5 (a) reports the Ni XMCD spectra recorded for $TbPc_2$/Ni/Cu(100), $TbPc_2$/O/Ni/Cu(100), $TbPc_2$/Li/Ni/Cu(100), and $TbPc_2$/Ni/Ag(100). The intensity of the XMCD signal is given with respect to the average L_3 XAS intensity, $(I^+ + I^-)$ 2, which has been scaled to 1 for each sample. The spectra show that neither the intensity nor the lineshape of the Ni XMCD change significantly due to either Li or O adsorption. Even though XMCD is sensitive to the first 5-10 surface layers [58], strong changes of the electronic and magnetic properties of the topmost layer would show up in the spectra, as the latter contributes most to the electron yield signal. Since this is not the case, we conclude that the magnetic moment per Ni atom is similar for all the substrates investigated in this study. Note that, in the case of the $TbPc_2$/O/Ni/Cu(100), the $c(2 \times 2)$ $Ni(100)$ layer obtained by O-surfactant growth of Ni on Cu(100) represents a chemisorbed superstructure, not a NiO layer [61].

Furthermore, the exact reproducibility of the Tb XAS and XMCD spectral features proves that the Tb electronic configuration, including its spin (**S**) and orbital (**L**) moment, is not affected

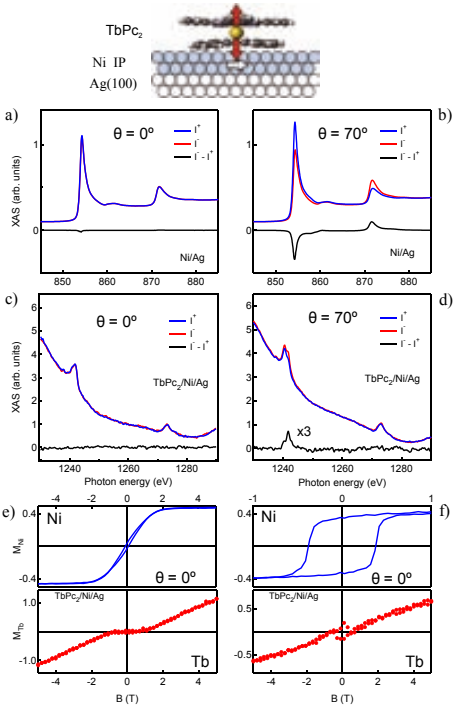

Figure 3.6: a) Schematic view of $TbPc_2$ on IP Ni/Ag(100). XAS and XMCD spectra measured on $TbPc_2$/Ni/Ag(100) at the $L_{2\,3}$ Ni edges b) (c)) and $M_{4\,5}$ Tb edges d) (e)) for $\theta = 0°$ ($\theta = 70°$). Magnetization curves recorded on the same sample on Ni (top) and Tb (bottom) edges at normal f) and grazing incidence g). The units of $\mathbf{M}_{\mathrm{Ni}}$ and $\mathbf{M}_{\mathrm{Tb}}$ correspond to the XMCD intensity at the L_3 and M_5 absorption edges.

by either i) or ii). Figure 3.5 (b) reports the Tb XMCD spectra obtained on the Ni substrates shown in (a). We observe that the

XMCD lineshape does not vary from sample to sample, indicating that the magnetic ground state of Tb is predominantly of $4f^8$ character, in agreement with previous studies of Tb compounds [30,84] and $TbPc_2$ [9, 32, 51, 76]. However, the intensity of the XMCD spectra at 5 T is significantly reduced for $TbPc_2$/Li/Ni/Cu(100) compared to the other samples. Given that the easy axis magnetization of $TbPc_2$/Li/Ni/Cu(100) appears to saturate near 5 T [Fig. 3.4(c)], this effect can possibly be attributed to a reduction of the Tb atomic magnetic moment induced by charge transfer. Indeed, a previous study of the negatively charged $TbPc_2$ moiety has shown that even a very moderate charge transfer to the $4f$ Tb states, of the order of 0.1 electrons, can lead to significant reduction of the XMCD/XAS ratio at finite field [9]. XAS spectra recorded with linearly polarized light also show a reduction of the spectral weight of the M_5 features at 1242 and 1243.2 eV, which is consistent with increased occupancy of the Tb $4f$ states (Fig. 6 (I put the figure?)). This interpretation agrees with our hypothesis of charge donation from Li to $TbPc_2$. Note that, according to Refs. [9] and [35], most of the negative charge of the $TbPc_2$ anion is localized on the Pc ligands, and only a small fraction of it is effectively transferred into the Tb $4f$ states.

On the other hand, the magnetic behavior of $TbPc_2$ changes significantly. The remanent $\mathbf{M}_{\mathrm{Tb}}$ strongly decreases (increases) in $TbPc_2$/O/Ni ($TbPc_2$/Li/Ni) layers compared to $TbPc_2$/Ni, as shown in Fig. 3.4 (a)-(c). Moreover, B_{exc} varies from 0.7 T in

$TbPc_2$/O/Ni to 2.5 T in $TbPc_2$/Li/Ni [Fig. 3.7 (a)], indicating that the exchange coupling energy increases significantly with the amount of charge donated to the Pc ligand.

It is not known with certainty what is happening to the molecule and the amount of charge transfer. We could only make some hypothesis, waiting for future studies. The neutral unsupported TbPc2 ($[TbPc_2]^0$) molecule has two spin systems: one, strongly localized on the metal center and arising from the 4f states, carries a magnetic moment of 5.9 μB, and, in the limit of an isolated Tb^{3+} ion, it would have $J = 6$; the other, delocalized over the two Pc ligands, is determined by the unpaired π electron and is defined by $S = 1\ 2$ [87]. When the molecule is deposited on a metalic surface, it tends to become a charged system ($[TbPc_2]^{-\delta}$) and to saturate the unpaired π orbital. Depending on the amount of charge transfer, this can suppress or enhance the spin density of the ligand. Oxidation (reduction) of the sample has probably the effect of removing (adding) a fraction of the charge to the ligand. If $\delta > 1$, this effect might result in a decrease (increase) of the Ni-Tb coupling mediated by the ligand spin. Further investigations are necessary to unravel this point.

3.2.4 Role of the magnetic anisotropy

Measurements of $TbPc_2$ on IP Ni films, reported in Fig. 3.6, illustrate the case where the molecule and substrate easy axes are orthogonal to each other. XAS and XMCD spectra are shown for

Ni and Tb in remanence for normal (a), (c) and grazing incidence (b), (d). In the case of $\theta = 0°$, no remanence is observed for Tb XMCD, while Ni shows a very small signal. On the contrary, for $\theta = 70°$ (beam parallel to the Ni easy axis), a small peak is measured antiparallel to the Ni one. Although the coupling between $TbPc_2$ and Ni remains AFM, as expected, the remanent Tb XMCD intensity is now strongly reduced compared to the Ni XMCD. Magnetization curves (Fig. 3.6 (e), (f)) confirm this behaviour. Measurements in normal incidence, orthogonal to the Ni easy axis, show that the molecule has zero average magnetization. Only by increasing the magnetic field we are able to force the molecule magnetization to rotate, but without reaching its saturation value. Grazing incidence hysteresis loops reveal the AFM coupling with the substrate, despite the orthogonal configuration of the easy axes, at low fields.

This result shows the importance of matching the substrate and SMM magnetic anisotropy properties to effectively stabilize the SMM magnetization in the absence of external magnetic fields. Notably, this is in contrast with recent theoretical calculations of Mn_{12} on Ni, which postulate that the magnetic easy axis of the SMM/substrate system is dictated by that of the Ni layer [63].

3.2.5 Spin Hamiltonian

The competition between the intrinsic SMM properties, namely the magnetic anisotropy and Zeeman interaction of $TbPc_2$, and

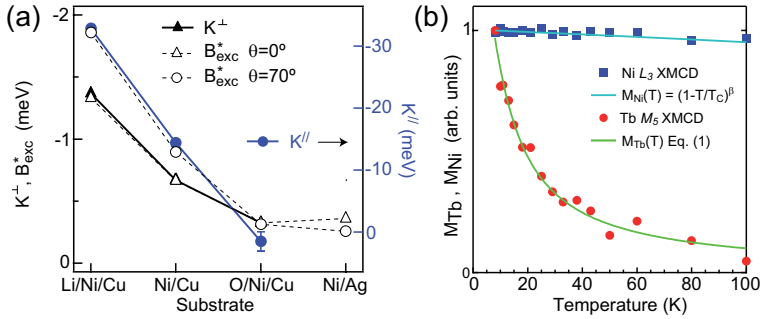

Figure 3.7: (a) Exchange field (B_{exc}) and coupling constant (J_{exc}) derived from Fig. 3.4 and Eq. 3.3, respectively. (b) Temperature dependence of the remanent Ni and Tb XMCD intensity, normalized to the values at T = 8 K. Solid lines represent the calculated magnetization (see text).

AFM exchange to the substrate, can be described using the following Hamiltonian:

$$H = \mu_B(\mathbf{L}+2\mathbf{S})\cdot\mathbf{B} + J_{exc}\mathbf{M}_{\mathrm{Ni}}\cdot\mathbf{S} - \lambda\mathbf{L}\cdot\mathbf{S} - B_2O_2^0 + B_4O_4^0 - B_6O_6^0 \tag{3.3}$$

where μ_B is the Bohr magneton, J_{exc} the exchange coupling constant to Ni, $\lambda = 212$ meV the spin-orbit energy, and the last three terms represent the expansion of the Tb crystal field potential using the Stevens operators O_k^m. As the $TbPc_2$ crystal field is not affected by deposition on metals [75], we take the same coefficients $B_2 = 414$, $B_4 = 228$, and $B_6 = 33$ cm^{-1} as for the free molecule, which give a magnetic anisotropy barrier of about 590 meV [38]. Thus we use Eq. (1) to calculate the expectation

value of $\mathbf{M}_{\mathrm{Tb}} = -\mu_B(\ \mathbf{L}\ + 2\ \mathbf{S}\ )$ as a function of applied field and temperature and fit the curves reported in Fig. 3.4. The fit is restricted to the bottom $J = L + S = 6$ multiplet of $TbPc_2$ [38] and has only two free parameters: J_{exc} and a multiplicative factor that scales $\mathbf{M}_{\mathrm{Tb}}$ to the XMCD intensity. The results, shown as solid lines, capture remarkably well the easy and hard axis behavior of $TbPc_2$ on OP substrates, demonstrating that our model reproduces the main features of the SMM-substrate interaction.

Figure 3.7 (a) compares the values of J_{exc} and B_{exc} measured at $\theta = 0°$ and 70°. We see that J_{exc} varies from -0.3 to -2 meV going from $TbPc_2$/O/Ni to $TbPc_2$/Li/Ni, in agreement with B_{exc}. Moreover, we find that J_{exc} is anisotropic, depending on the angle between $\mathbf{M}_{\mathrm{Tb}}$ and $\mathbf{M}_{\mathrm{Ni}}$ as well as on the substrate. We leave the investigation of this point to future studies, noting that the symmetry of the system, as well as the strong spin-orbit coupling of the Tb $4f$ states, allow for the presence of anisotropic superexchange terms [55].

3.2.6 Dipolar field from the substrate

The antiparallel ordering of the $TbPc_2$ and Ni magnetic moments is attributed to ligand-mediated superexchange coupling. In principle, however, antiferromagnetic coupling can also be attributed to the dipolar field emanating from the Ni surface atoms. Although the dipolar field produced by a continuous magnetization density with either in-plane (IP) or out-of-plane (OP) orientation

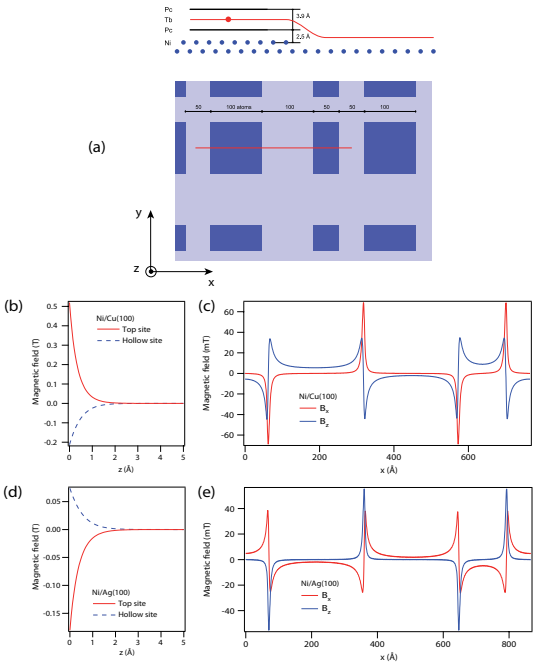

Figure 3.8: (a) Schematic of the Ni surface employed in the calculations of the dipolar field (B_{dip}). Dark blue areas indicate second layer Ni islands, blue dots the position of Ni atoms. (b) B_{dip} as a function of z calculated for a single Ni layer with OP magnetization and lattice spacing pseudomorphic to Cu(100). (c) B_{dip} as a function of x calculated along the red line shown in (a) for OP Ni. (d) B_{dip} as a function of z calculated for a single Ni layer with IP magnetization and lattice spacing pseudomorphic to Ag(100). (c) B_{dip} as a function of x calculated along the red line shown in (a) for IP Ni.

is zero outside an infinite surface plane, the discrete atomic lattice structure of a real surface may give rise to sizeable fields close to the surface [19], the magnitude of which depends also on the x,y position within the surface unit cell as well as on roughness [14,85]. In order to address this point, we have carried out a model calculation of the dipolar field produced by a (100) Ni surface layer made of 2100 by 2100 atoms. The effects of roughness are included by simulating second layer islands of 10 to 20 nm lateral size. A diagram of the simulated Ni surface is shown in Fig. S5 (a). A $TbPc_2$ molecule is shown to scale with the Ni lattice constant. The distance between the Pc ligand and the topmost Ni atoms is taken to be 2.5 Å from density functional calculations of metal-Pc adsorbed on metal surfaces [13, 57], whereas the distance between the bottom and top Pc ligand is taken to be 3.9-4 Å [32]. The number of atoms in the simulation is such that the results can be considered accurate: for instance, adding an additional bottom layer would not change significantly the value of the dipolar field on the surface, due to the exponential decrease of the field with z.

The calculations were done by adding dipolar fields from individual dipoles, giving a resultant field

$$\mathbf{B}_{dip} = \frac{\mu_0}{4\pi} \sum_i \left(3\frac{(\mu \cdot \mathbf{r}_i)\mathbf{r}_i}{r_i^5} - \frac{\mu}{r_i^3} \right) \tag{3.4}$$

where $\mathbf{r}_i$ is the position of the i-th atom, and μ its magnetic moment. For the calculation, we take $\mu = 1\,\mu_B$ to provide a worse case estimate of B_{dip}, given that the magnetic moment of Ni sur-

face atoms is about 0.7 μ_B. The calculations were performed for Ni atoms with out-of-plane (OP) magnetization and Cu(100) lattice spacing [Fig. 3.8 (b) and (c)] as well as for Ni atoms with in-plane (IP) magnetization and Ag(100) lattice spacing [Fig. 3.8 (d) and (e)]. Figures 3.8 (b) and (d) show that B_{dip} decreases exponentially with increasing distance from a homogenous Ni layer, reaching values well below 0.01 T for $z > 2$ Å . Oscillations of B_{dip} moving in the xy plane from on-top to hollow sites are already very small at this distance. Figures 3.8 (c) and (e) report B_{dip} calculated at $z = 4\,45$ Å above the Ni surface plane, along the red line shown in (a). The effects of roughness are most visible at the edges of the islands, where B_{dip} attains a maximum value of about 0.07 T on both OP and IP surfaces. This is still very small compared to the exchange fields evidenced by our study. Moreover, B_{dip} changes sign for molecules on top or between islands, resulting in an average field below 0.002 T. Since our XMCD measurements are sensitive to macroscopic surface areas of the order of $0\,1 \times 1$ mm^2, dipolar fields can have only a very small influence on the magnetic properties of $TbPc_2$ on Ni. We therefore conclude that the antiferromagnetic coupling of $TbPc_2$ on Ni is due to exchange forces.

3.2.7 Temperature dependence

The final study of this experiment is to adress to the magnetic stability of $TbPc_2$ on Ni as a function of temperature. Fig. 3.7

(b) compares $\mathbf{M}_{\mathrm{Tb}}$ and $\mathbf{M}_{\mathrm{Ni}}$ measured at remanence for the OP $TbPc_2$/Ni sample. The solid lines represent $M_{\mathrm{Tb}}(T)$ calculated using Eq. (1) and $M_{\mathrm{Ni}}(T) = (1 - T\ T_C)^{\beta}$, with $T_C = 575$ K and $\beta = 0\ 28 \pm 0\ 04$ [33]. We observe finite remanence of $\mathbf{M}_{\mathrm{Tb}}$ up to $T = 100$ K, showing that coupling with Ni stabilizes $\mathbf{M}_{\mathrm{Tb}}$ well above T_B on a timescale that exceeds by several orders of magnitude the typical $\tau = 10^{-3} - 10^{-1}$ s probed by ac susceptibility measurements of $TbPc_2$ [36, 39]. We also note that XMCD measurements of $TbPc_2$ adsorbed on nonmagnetic substrates report zero remanence at least down to $T = 2$ K [9, 51, 76].

3.3 Summary

In summary, we have proven that SMMs couple antiferromagnetically to FM metal layers through superexchange interactions. Contrary to paramagnetic molecules, $TbPc_2$ do not mimic the substrate magnetization and behave as coupled but separate magnetic units from the underlying FM surface. This coupling depends on the relative orientation of the molecule and substrate anisotrpy axes, superexchange and Zeeman interaction, as our fitting spin hamiltonian demonstrate. The magnitude but not the sign of the exchange coupling energy can be tuned by reducing or oxidizing the substrate. A further result is the enhanced tharmal stability shown by $TbPc_2$, when deposited on a FM layer.

Chapter 4

Coupling of Single Molecule Magnets to antiferromagnetic substrates

This chapter presents the results obtained by depositing $TbPc_2$ on antiferromagnetic (AFM) surfaces. The first paragraph contains a brief overview of exchange bias, the effect at the origin of the coupling between molecules and AFM substrates, while the second paragraph reports our experimental results, which demonstrate the presence or absence of exchange bias on two different AFM substrates: Mn and CoO.

4.1 Exchange bias

4.1.1 Introduction

Exchange bias is an interface effect that arises when a ferromagnet is put in contact with an antiferromagnet. When two magnetic layers interact, several interesting properties can appear. In general, this interaction can be described as an effective magnetic field between the two magnetic materials in physical contact with each other. This field can be a regular field (stray field) or an effective field produced by the quantum mechanical exchange interaction. In the case of exchange bias, the size of the effect can only be explained by assuming an exchange interaction at the FM-AFM interface. This phenomenon was discovered by Meiklejohn and Bean in 1956 [53, 54] in the study of Co particles embedded in their native antiferromagnetic oxide. Above the Nèel temperature (T_N), these coated particles had magnetic properties as expected for pure Co ones. Below the T_N of CoO, if the sample was cooled in an external magnetic field, Meiklejohn and Bean observed a horizontal displacement of the hysteresis loop and an enhacement of the coercivity of the nanoparticles, which they attributed to an exchange interaction between spins of FM Co and AFM CoO.

Initially exchange bias research focused on thin films systems. This was due to the possibility to have: (i) an increased number of FM-AFM combinations compared to nanoparticles; (ii) greater control of the FM-AFM interface; (iii) important tech-

nological applications in the field of magnetic recording, such as magnetic recording heads, spin-valve devices and magnetic tunnel junctions [64]. Spin-valve devices, for example, are made of two ferromagnetic layers: the reference layer, that is pinned by exchange bias to an antiferromagnet, and the sensing layer. If the external field is much weaker then the exchange bias field, the magnetic moment of the reference layer is essentially fixed so that the sensing layer in the sandwich is free to respond to external fields.

In recent years, the continuous demand for miniaturization of devices and for increased density of data storage has renewed the interest in magnetic nanoparticles and nanostructured materials because of their potential for applications in fields such as ultrahigh-density recording and medicine. The main problem of reducing dimensions is the superparamagnetic limit: decreasing the particle sizes, the anisotropy energy becomes comparable to the thermal energy, and thermal fluctuations induce random flipping of the magnetic moment with time so that the nanoparticles lose the magnetic stability. A new prospective application of exchange bias in nanoparticles has recently been developed. Exchange bias has been proposed theoretically as a possible source of magnetization stability to overcome the superparamagnetic limit [43]. Skumryev *et al.* [74] experimentally demonstrate that the magnetic coupling between Co FM nanoparticles with an AFM matrix is a source of a larce magnetic anisotropy. This leads

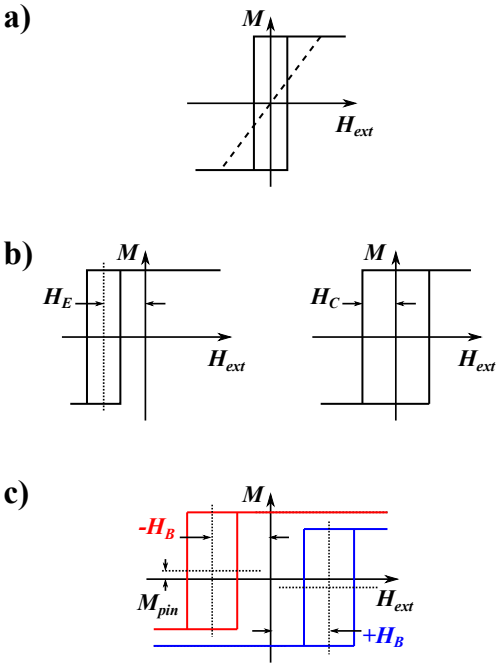

Figure 4.1: (a) Magnetizations curves measured along the easy (solid line) and hard axis (dotted line) of an ideal ferromagnet with uniaxial anisotropy. (b) Hysteresis loops of an ideal FM-AFM system. If the exchange anisotropy is high, the loop is horizontally shifted (left). This correspond to a system with uniderectional exchange anisotropy. On the other hand, for weak exchange anisotropy, only an increase of the coercivity is observed (right). (c) Negative (red) and positive (blue) exchange bias fields, depending on the direction of the loop shift with respect to the setting field. The vertical loop shift originating from pinned moments is also shown.

to a marked improvement of thermal stability of the FM moments and a significant enhancement of the blocking temperature T_B.

The aim of our investigation is to transfer these concepts to magnetic molecules, thereby enhancing the stability of their magnetic moment.

4.1.2 Phenomenology of exchange bias

In this paragraph we present the phenomenon, and get familiar with the terminology associated with exchange bias. Figure 4.1a presents magnetization loops of a conventional FM along the easy and hard axis directions: the curves are symmetric about zero external magnetic field $\mathbf{H_{ext}}$. The anisotropy is assumed to be uniaxial. If a FM is deposited on an AFM and cooled through the T_N in the absence of an external field, the hysteresis loop will still be symmetric with respect to the origin, but the easy axis will be determined by the magnetocrystalline anisotropy of the AFM, not by that of the FM itself [79]. In this case we will speak about uniaxial exchange anisotropy and we will also observe a change in the coercivity of the loop. If an external magnetic field $\mathbf{H_{ext}}$ (assumed to be in the positive direction) is applied or the FM lays in a remanent state, and the sample is cooled below T_N, the magnetization loop may shift horizontally in either the negative or positive field direction, as shown in Fig. 4.1c. This case corresponds to a unidirectional magnetic anisotropy, since the positive and the negative external field directions are no longer

equivalent.

In negative exchange bias (Fig. 4.1c), the FM and AFM moments are aligned in the same direction of the field, hence there is a $J > 0$ exchange coupling constant. The existence of positive exchange bias has been suggested to arise from antiparallel coupling ($J < 0$) between FM and AFM moments, although it is somewhat more complicated. For small cooling fields the FM is aligned along the external field H_{ext}, while the AFM is determind by the antiparallel exchange coupling with the FM. The combination of $J < 0$ and AFM moments that are antiparallel to H_{ext} leads to a preferred FM alignement in the direction of the field, i.e., negative bias. In large cooling fields the Zeeman energy dominates and the moment directions in both FM and AFM are parallel to H_{ext}. When the field is turned off, the moments in the AFM remain frozen (parallel to H_{ext}), but the antiparallel exchange coupling leads to a rotation of the FM moments. The direction of the FM is now antiparallel to H_{ext}, which corresponds to a positive exchange bias. Another interesting finding in FM-AFM systems is the increase in the coercivity of the magnetization curves, as indicated in figure **??**c by a broadening of the loops. This broadening is caused by the coupling of the FM to the AFM at the interface. This happens below T_N, as the AFM orders itself.

In a simplified view, the exchange bias phenomenon can be described in terms of an alignement of the AFM spins at the FM-AMF interface parallel to the FM spins occuring during the field

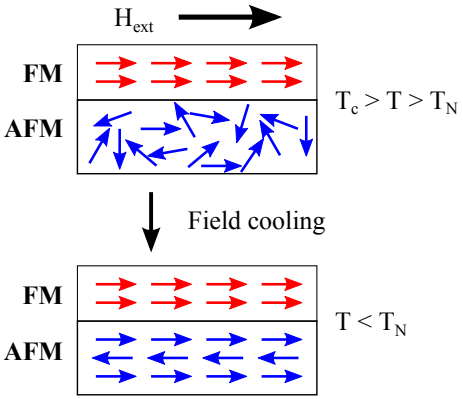

Figure 4.2: Field cooling procedure for a FM in contact with an AFM. FM moments allign with the external field direction and induce ordering on the AFM.

cooling procedure (Fig. 4.2). The coupling between AFM and FM spins exerts an additional torque on the FM spins, which the external field has to overcome. Whithin this intuitive model, one can predict only two different cases, depending on the strengh of the AFM magnetic anisotropy (Fig. 4.1b,4.3). If the AFM anisotropy is small, one should only observe an enhancement of the coercivity, becouse the spins of the FM, rotating, will be able to drug also the AFM ones; for large AFM anisotropies, the FM spins will decouple from the AFM ones, producing only an horizontal shift of the loop. Nevertheless, in general, real systems show both effects, due to roughness, defects, grain size, etc... which induce local variations of the AFM magnetic anisotropy.

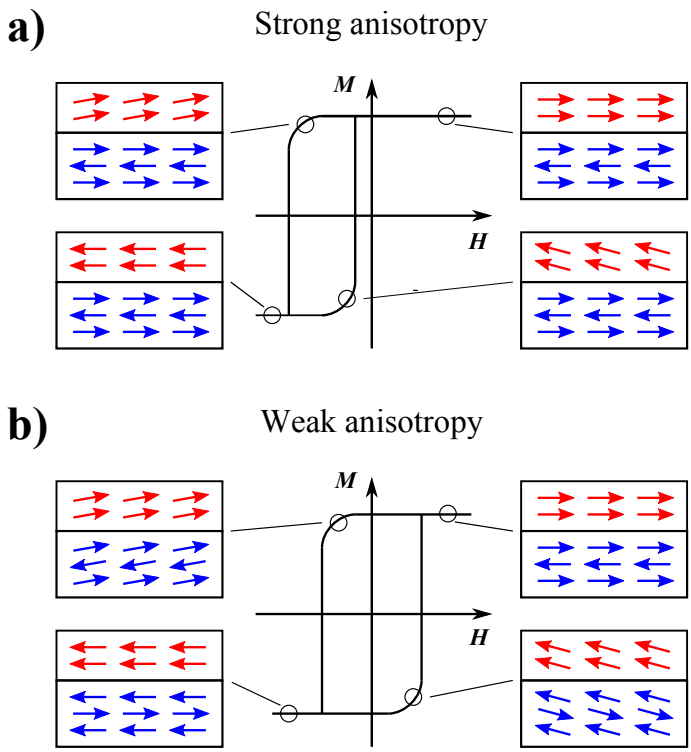

Figure 4.3: (a) For strong exchange anisotropy, the AFM moments do not rotate with the FM, giving an horizontal shift of the hysteresis. (b) For weak anisotropy, FM moments drug the AFM ones, increasing the coercivity of the loop.

This anisotropy is not a constant and has a strong dependence with the temperature. Above T_N, the AFM moments have a random distribution, so that only the FM contribute to the anisotropy. On the other hand below T_N, FM and AFM are cou-

pled and the total anisotropy is given by adding a further contribution. At $T \approx T_N$ we observe a transition region. The coercivity H_C is strongly affected by the exchange anisotropy, and hence by the temperature, and presents a peak just below T_N [59]. This behaviour is intuitively simple to understand. The peak is due to the decrease of AFM anisotropy close to T_N: as the anisotropy decreases, the FM is able to drag increasingly more AFM spins, thus increasing the coercivity. Above T_N the AFM is random, thus it does not hinder the FM rotation.

It is also worth noting that T_N is not always a constant and depends on the AFM thickness (t_{AFM}): in several materials, decreasing the t_{AFM}, passing from bulk to thin film, a decrease of the T_N was observed. In CoO, for example, T_N changes from room temperature in the bulk, to $T_N \approx 0K$ for t_{AFM} 0 [4].Also the exchange bias field presents a thickness dependence. H_E is roughly inversely proportional to the thickness of the FM layer (t_{FM}), but this relation is no longer valid for very thin films, probably because the layer become discontinuous. The depenence of H_E with respect to t_{AFM} is more complicate, due to factors such as the anisotropy, the T_N dependence on t_{AFM}, grain size, etc... and changes from sample to sample [59].

Several models have been proposed to undestand the mechanism of exchange bias. Meiklejohn and Bean presented the first and simplest model [53]. This model assumes an uncompensated antiferromagnetic interface with a net spin and Heisenberg cou-

pling between the AFM and the FM spins. If one also assumes that the AFM does not undergo reversal with the FM, then there will be a unidirectional anisotropy that shifts the hysteresis loop and the displacement can be calculate as

$$H_E = -\frac{J_E}{\mu_0 M_{FM} t_{FM}} \cos(\theta) \tag{4.1}$$

where J_E is the interfacial exchange energy per unit area, M_F the saturation of the magnetization of the FM and θ is the angle between the external magnetic field and the FC direction. However, the exchange bias fields H_E predicted by this model are too big if compared to real measurements [66]. Mauri s model assumes the formation of a domain wall within the AFM that would decrease the exchange energy cost associated with reversal of the FM [52]. The important point to underline is that the presence of the domain wall reduces the expected bias field, making the model predictions consistent with experiments. The weak point, however, is that the model does not work in the limit of very thin AFM so that it is not possible to form a domain wall [66]. Malozemoff proposed another mechanism for exchange anisotropy postulating a random nature of exchange interactions at the interface [49, 50]. This model considers the effect of the interface roughness on a compensated AFM-FM interface. It turns out to be energetically favorable to form domains on the AFM interface surface and these domains lead to a reduction of the H_E with a similar form as the one found by Mauri.

In recent years, X-ray dichroism spectroscopy and microscopy measurements have given a key contribution to the real understanding of the exchange bias phenomenon, providing intercace-specific magnetic informations. It was confirmed that, near the interface, there are uncompensated spins that originate from magnetic atoms in the AFM and that not all uncompensated spins contribute in the same way. Tipically, during the field cooling procedure in an external magnetic field, a small fraction of these uncompensated spins get pinned by the field and by the oredered spins of the FM. If now the external field is applied in the opposte direction, the magnetic moments of the FM start to rotate. Since the AFM is exchage coupled to the FM, a torque will be applied to the AFM spins: the majority of the uncompensated spins will rotate with the FM, contributing to the coercivity, while the pinned spins will remain blocked in their direction, creating bias. This result was demonstrated by Ohldag *et al.* [62], measuring a Co(2nm)/$Ir_{20}Mn_{80}$(50nm) system by XMCD and presenting FM and AFM hysteresis loops, separatley. Besides the horizontal displacement of the loops, a small vertical shift was also observed, as shown in Fig. 4.1c. Since pinned spins cannot be rotated away from their preferred direction by typical external magnetic fields, they will give a small vertical offset to the magnetization curves measured parallel to their preferetial direction. From the asimmetry between vertical loop shift and loop height, the ratio between pinned and rotating uncompensated spins can be determined. As

we will see, the presence of pinned spins is the key also to induce exchange bias inj hybrid molecule/metal systems.

4.2 $TbPc_2$ on AFM substrates: experimental results

As described in chapter 3, we deposited the SMM $TbPc_2$ on a ferromagnetic Ni substrates in order to stabilize the magnetic moment of the molecule as well as demonstrated how the SMMs couple to Ni through the superexchange interaction. A step forward in the control of SMMs would be to demonstrate the coupling between TbPc2 and an AFM substrate. This finding would enable indipendent magnetization reversal of molecular layers with respect to pinning substrate, a first step to design a truly molecular spin valve device. The key phenomenon that would reveal the presence of the coupling is exchange bias, as tipically observed in FM/AFM bilayers or in core shell nanoparticles. However, the possibility of inducing exchange bias between a molecule and an AFM has not been reported thus far. There are actually distinct reasons that put molecular exchange bias into question: (i) Exchange bias is triggered locally by the presence of pinned uncompensated spins in the AFM [60, 62, 82]. As the molecules constitute discrete magnetic elements, there is no mechanism guaranteeing that the sparse pinning centers of an AFM may bias a single molecule, unless this adsorbs on or creates a pinning site. (ii) Biasing is unlikely to

extend from individual sites to a continuous molecular layer, since the magnetic moments of molecules adsorbed next to each other are usually uncoupled [29]. (iii) Thermal fluctuations tend to randomize the orientation of the molecular magnetic moment down to temperatures $T \ll T_N$, which hinders the alignment of the pinned spins in the AFM during the field cooling (FC) process.

Here we present a series of experiments aimed at establishing the presence or absence of molecular exchange bias at the interface between $TbPc_2$ and different types of AFM substrates, namely insulating CoO (paragraph 4.2.1) and metallic Mn thin films (paragraph 4.2.2) deposited on a single crystal Ag(100) surface.

4.2.1 $TbPc_2$ on CoO substrates

We started depositing $TbPc_2$ molecules on CoO, a model type II insulating AFM, grown epitaxially on Ag(100). This choice is motivated by the enhanced XMLD contrast, which enable to determine the orientation of the AFM spins in CoO [91] and also because oxidized Co films exhibit rather large exchange bias and a large interface energy ($\Delta E = 3\ 5 erg\ cm^2$ at 10K) [59].

$TbPc_2$/CoO(10 ML)/Ag sample was grown in-situ, at ID08 beamline of the ESRF by molecular beam epitaxy in ultra-high-vacuum (UHV), by evaporating Co in a pure oxygen atmosphere of 10^{-7} mbar on a clean Ag(100) substrate at room temperature, as described in Refs. [70, 72]. About 0.5 ML of $TbPc_2$ molecules were deposited on the CoO substrate, by sublimation of the molec-

ular powder in UHV. The coverage was calibrated using scanning tunnelling microscopy (Fig. 4.5b).

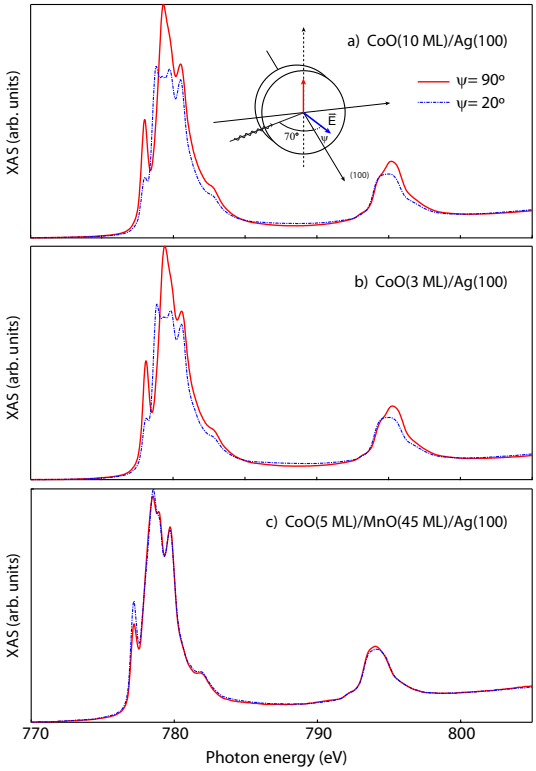

Figure 4.4: Co $L_{2,3}$ linearly polarized x-ray absorption spectra of (a) CoO(10 ML)/Ag(100), (b) CoO(3 ML)/Ag(100), and (c) CoO(5 ML)/MnO(45 ML)/Ag(100) recorded with the electric field vector making an angle $= 20°$ and $90°$ with respect to the surface normal. The x-ray incidence angle is $\theta = 70°$ in both cases.

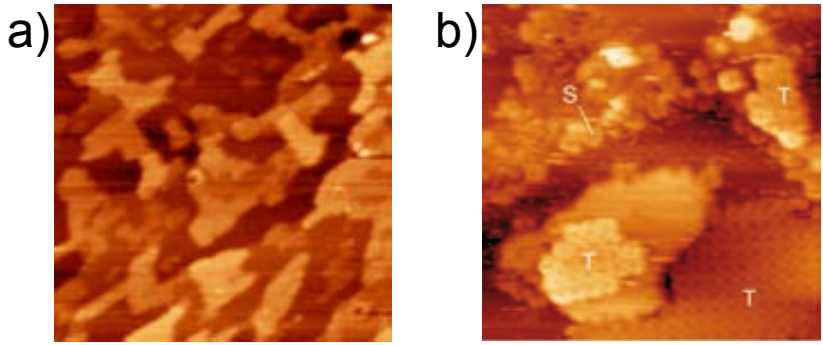

Figure 4.5: (a) STM image of 3 ML CoO/Ag(100). Image size: 150 × 150 nm^2. (b) STM image of $TbPc_2$ deposited on 3 ML CoO/Ag(100) at room temperature. Image size: 30 × 30 nm^2. Molecules on terraces and at steps are indicated by T and S, respectively.

In bulk CoO the spins tend to align close to the (111) direction [41], while in thin films the compressive strain is expected to favor in-plane spin alignment in CoO/Ag(100) [21]. Fig. 4.4a shows that linearly polarized absorption spectra of the CoO (10 ML) agree with those reported in other studies of stoichiometric CoO films [1, 21]. In order to investigate the influence of the substrate on the magnetic behaviour of $TbPc_2$/CoO(10 ML)/Ag, other two samples were prepared: $TbPc_2$/CoO(3 ML)/Ag and $TbPc_2$/CoO(5 ML)/MnO(45 ML)/Ag. The first presents a thinner CoO layer, with clear terraces of ?? nm (Fig. 4.5a); nevertheless it shows a similar linear spectra (Fig. 4.4b), confirming an in-plane alignement. The second sample was grown with the

intent of changing the CoO easy axis. According to Csiszar *et al.* [21], CoO films grown on MnO/Ag(100) experience a large tensile strain, which induces out-of-plane alignment of the Co spins. The signature of this effect is a change of the x-ray linear dichroism spectrum of Co, as reported in Fig. 4.4c.

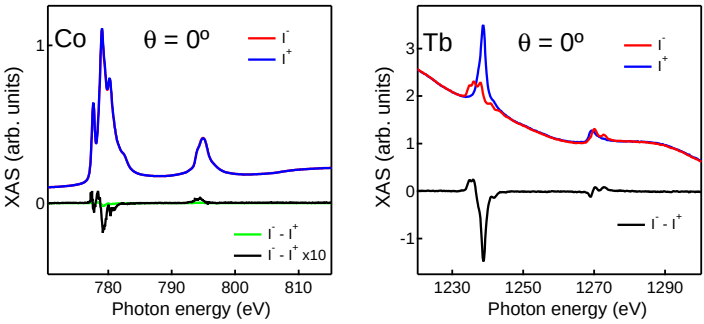

Figure 4.6: (a) Schematics of $TbPc_2$ adsorbed on CoO/Ag(100). (b,c) XAS and XMCD spectra of $TbPc_2$/CoO(10 ML)/Ag recorded at the $L_{2,3}$ Co (b) and $M_{4,5}$ Tb (c) edges after FC at $B = 5$ T, $\theta = 0°$, and $T = 8$ K.

Figure 4.6 shows a schematic of $TbPc_2$ adsorbed on CoO and the experimental geometry. The sketch also underlines the in-plane spin allignement, while it is known that $TbPc_2$ molecule presents an out-plane-plane easy axis, orthogonal to the phtalocyanine planes. This is not the most favorable configuration to expect molecule-substrate coupling, although weak coupling was observed in $TbPc_2$ on in-plane Ni substrates [48].

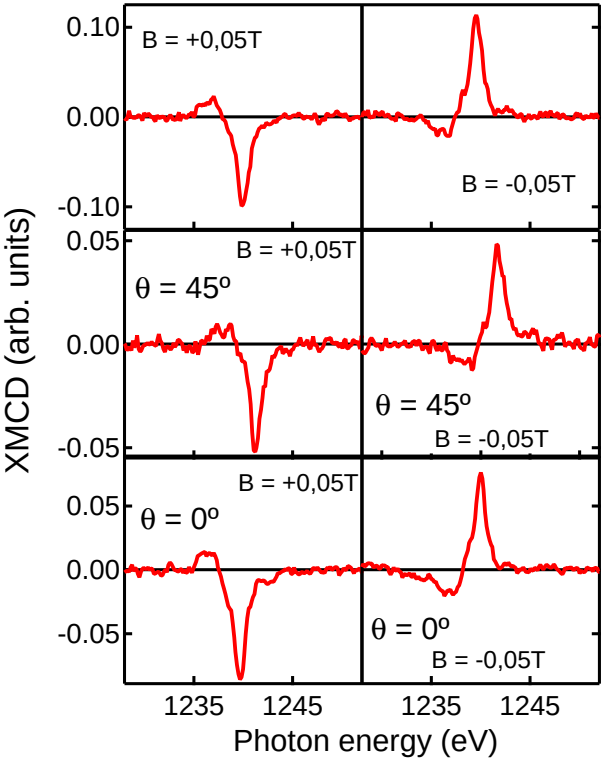

Figure 4.7: XMCD intensity of the M_5 Tb edge measured at $B = \pm 0\,05$ T on $TbPc_2$/CoO(10 ML) (top), $TbPc_2$/CoO(3 ML) (middle), and $TbPc_2$/CoO(5 ML)/MnO(45 ML) (bottom) after FC at B = 5T and $\theta = 0°$ (top), $\theta = 45°$ (middle) and $\theta = 0°$ (bottom), respectively.

Figures 4.6 (b) and (c) show the circularly polarized XAS and XMCD of Co and Tb, respectively, for $TbPc_2$/CoO(10 ML)/Ag

recorded after FC from 300 to 8 K at $B = +5$ T and $\theta = 0°$. CoO presents a very weak field-induced XMCD, as expected for a compensated AFM surface, whereas the Tb magnetic moment is fully saturated. In order to verify the presence of exchange bias, we measured the intensity of the Tb XMCD during a $+B$ $-B$ field sweep around $B = 0$. As shown in Fig. 4.7, spectra recorded at $B = +0\,05$ and -0.05 T reverse sign and have similar intensity, indicating that the magnetization loops are symmetric with respect to the origin. This finding is confirmed by the measurement of a complete magnetization cycle (Fig. 4.8a), which yields a reversible and symmetric loop. Such paramagnetic behavior is consistent with that of $TbPc_2$ molecules deposited on nonmagnetic substrates, which do not show hysteresis at $T = 8$ K [51, 76].

Element resolved magnetization curves were measured by averaging up to 16 XMCD spectra per point and reporting the XMCD intensity at the M_5 edge of Tb as a function of applied magnetic field. This method is extremely time consuming compared to the one reported in paragraph 3.2.2, but was nonetheless preferred over averaging several hysteresis loops recorded at fixed photon energy because of its accuracy and the possibility to detect training effects. Throughout this work, the XMCD signal is presented in units of the average XAS intensity, $(I^+ + I^-)$ 2, which minimizes geometry- and field-induced effects on the electron yield and makes it proportional to the atomic magnetic moment of the element under investigation.

It is worth noting that the Tb loop presents inflection points at $B = \pm 0\ 5$ T, which are reminiscent of the plateaus of the butterfly magnetization curves of $TbPc_2$ in molecular crystals [40]. This points are not immediately visible, therefore we applied a numerical derivative to make them clear. Figure 4.9 shows Tb magnetization during a $+5 \quad -5$ T field sweep of $TbPc_2$/CoO(10ML) and his derivative (green line): the inflection points are indicated by arrows and correspond to the local minima of the derivative signal.

Several reasons may explain the absence of exchange coupling of $TbPc_2$ on CoO. We discuss the most relevant below: 1) The $TbPc_2$ magnetic moment fluctuates during FC, so that the effective exchange field at the SMM/AFM interface averages out as the temperature drops below T_N; 2) If the easy axes of $TbPc_2$ and CoO are perpendicular to each other and the magnetic anisotropy stronger than Tb-Co exchange, the bias field has essentially no effect; 3) The Tb-Co exchange interaction is too weak to be observed.

Although we did not measure T_N during this experiment, hypothesis 1 can be tested by decreasing the thickness of CoO down to 3 ML, which is expected to reduce T_N to about 20 K due to finite-size effects [4]. The middle panels of Fig. 6 show the XMCD spectra of $TbPc_2$/CoO(3 ML)/Ag recorded at $B = \pm 0\ 05$ T after FC at $B = +5$ T and $\theta = 45°$. In this geometry, the out-of-plane and in-plane directions are probed simultaneously. However, the

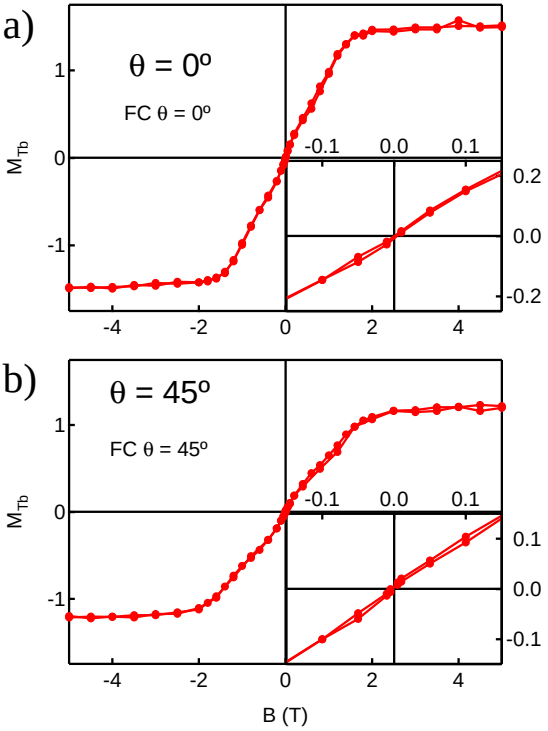

Figure 4.8: (a) Tb magnetization loop measured on $TbPc_2$/CoO(10ML) after FC at $\theta = 0°$ and B = 5T, recorded at $\theta = 0°$ and T = 8K. (b) Tb magnetization loop measured on $TbPc_2$/CoO(3ML) after FC at $\theta = 45°$ and B = 5T, recorded at $\theta = 0°$ and T = 8K. Insets: zoom of the low field region. Units refer to the intensity ratio $2*(I^+ - I^-)/(I^+ + I^-)$ measured at the M_5 Tb edge.

XMCD is still antisymmetric with respect to B, contrary to what would be observed for an exchange biased system. The second hy-

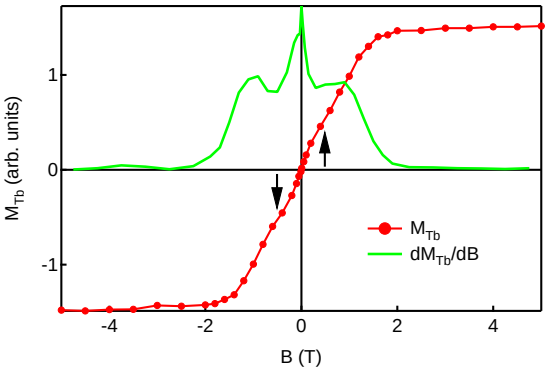

Figure 4.9: Tb magnetization (red line) measured during a +5 −5 T field sweep of $TbPc_2$/CoO(10ML) after FC at $\theta = 0°$ and $B = 5$ T, $T = 8$ K. The green line represents the derivative of the magnetization with respect to the applied field. Inflection points corresponding to local minima of the derivative signal are indicated by arrows.

pothesis was tested by growing 5 ML of CoO on 45 ML of MnO. According to Csiszar *et al.* [21], CoO films grown on MnO/Ag(100) experience a large tensile strain, which induces out-of-plane alignment of the Co spins. The signature of this effect is a change of the x-ray linear dichroism spectrum of Co, as reported in Supplementary Fig. 2. Also in this case, however, the XMCD spectra measured after FC at $B = \pm 0\,05$ T and $\theta = 0°$ do not present significant differences, apart from their sign (Fig. 6 (d), bottom panels). We conclude, therefore, that the coupling between $TbPc_2$ and CoO is too weak to produce sizeable bias effects, at least

within the sensitivity of the present study.

4.2.2 $TbPc_2$ on thin Mn layers

Since the exchange coupling between $TbPc_2$ and a FM was previously found to be larger for pure metal substrates compared to oxidized surfaces [48], we turned our investigation towards metallic AFM.

We opted for elemental Mn deposited on Ag(100), since Mn is expected to have a large magnetic zmoment [11, 69]. Up to 3 ML, the Mn has the tendency to create an MnAg alloy with fcc structure, as Mn substitutes the Ag positions in the fcc lattice. Above 3 ML, a pure Mn phase with bct structure grows on top of the interfacial alloy [70]. The bct Mn deposited on Ag(100) has the tendency to align out-of-plane [46].

We thus prepared a $TbPc_2$/Mn(3 ML)/Ag sample, following a similar procedure as described in paragraph 4.2.1. Figure 4.10 (a) shows STM image of the sample, proving the presence of $TbPc_2$ molecules on top of terraces or close to the steps. The molecules are adsorbed flat on the surface, as reported also in the linear spectra recorded on $M_{4,5}$ edges of Tb at room temperature. The small shoulders observed in the M_5 peaks suggest that maybe a small fraction of the molecules do not present an easy axis perpendicular to the surface [51], but this does not affect the interpretetation of our measurements.

We thus field cool the $TbPc_2$/Mn(3 ML)/Ag sample to 8 K

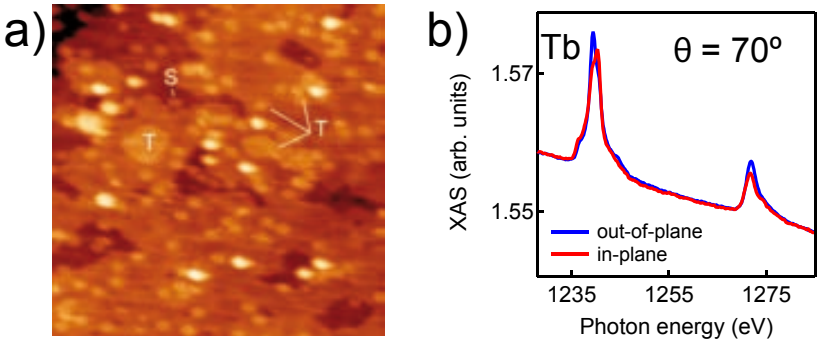

Figure 4.10: (a) STM image of $TbPc_2$ deposited on 3 ML Mn/Ag(100) at room temperature. Image size: 50×50 nm^2. Molecules on terraces and at steps are indicated by T and S, respectively. (b) Linear spectra recorded on $M_{4,5}$ edges of $TbPc_2$/Mn(3 ML)/Ag(100) sample at room temperature, probing in-plane and out-of-plane directions.

at $B = +5$ T and $\theta = 0°$. Figure 4.11 shows that the field-induced XMCD measured at the $L_{2,3}$ Mn edges is extremely small compared to paramagnetic Mn samples measured in similar conditions [26]. This indicates that the Mn layer is an AFM, although we cannot distinguish between a layered AFM structure and in-plane AFM order [69]. By reducing B from +5 to +0.05 T, we observe a ten fold reduction of the XMCD intensity. Most importantly, when reversing the field to $B = -0.05$ T, the sign of the XMCD remains constant, whereas the XMCD intensity measured at -5 T is smaller by 14 % with respect to that measured at +5 T [Fig. 4.11 (b)]. This behavior suggests the presence of uncom-

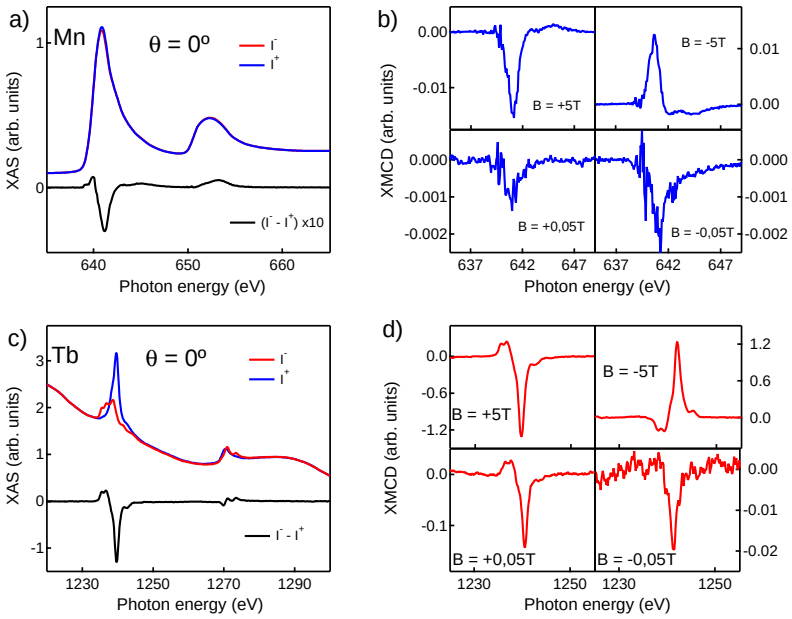

Figure 4.11: XAS and XMCD spectra of $TbPc_2$/Mn(3 ML)/Ag recorded after FC at $B = 5$ T, $\theta = 0°$, and $T = 8$ K. (a) $L_{2,3}$ Mn edges. (b) XMCD intensity at the L_3 Mn edge as a function of applied field. (c) $M_{4,5}$ Tb edges. (d) XMCD intensity at the M_5 Tb edge as a function of applied field.

pensated Mn spins, part of which rotate with the field and part pinned parallel to the FC direction. The vertical shift of the Mn magnetization loop, shown in Fig. 4.12 (a), confirms this hypothesis. The ratio between loop shift and height indicates that about 7% of the total uncompensated moments are pinned. By assuming

a magnetic moment of 3.5 μ_B per Mn atom [45], and correcting the spin moment obtained using the XMCD sum rule [17] for the overlap between the L_3 and L_2 Mn edges [26], we estimate that the percentage of uncompensated spins (pinned and unpinned) is about $(3 \pm 1)\%$ of the total Mn coverage.

The remaining point is whether the $TbPc_2$ molecules couple to the pinned Mn spins, leading to exchange bias. Figure 4.11 shows the XAS and XMCD spectra of Tb measured after FC, which are very similar to those reported for CoO [Fig. 6]. Yet, we find that the Tb XMCD does not reverse going from $B = +0\ 05$ T to $-0\ 05$ T and keeps the same sign as Mn [Fig. 4.11]. The measurement of the Tb magnetization loop provides final evidence of exchange bias in this system. Figure 4.8 reveals that, while $TbPc_2$ on CoO presents a closed loop, the magnetization of $TbPc_2$ on Mn is hysteretic and exhibits finite remanence and coercivity $H_C = 44 \pm 4$ mT. Furthermore, the Tb magnetization is negatively shifted along the field axis by an amount $H_E = -22 \pm 4$ mT. The sign of the shift is consistent with the parallel alignment of the Tb magnetic moment and pinned Mn spins evidenced in Figure 4.11.

From the skewed shape of the loop and the small remanence value, it is evident that only a small fraction of the $TbPc_2$ molecules is exchange-coupled to the substrate, consistently with the presence of a small percentage of pinned spins. This is very different from the case of $TbPc_2$ deposited on Ni, where all the molecules are coupled to the FM and a squared hysteresis loop

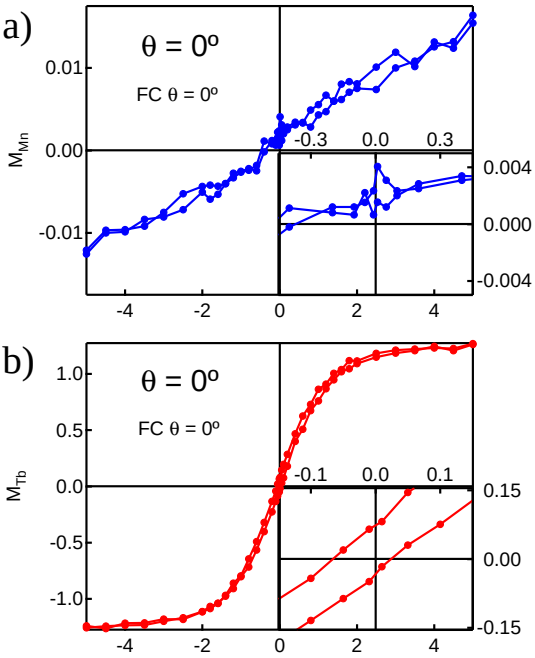

Figure 4.12: Magnetization loops of Mn (a) and Tb (b) measured on $TbPc_2$/Mn(3ML)/Ag(100), after FC at $\theta = 0°$ and $B = 5$ T, recorded at $\theta = 0°$ and $T = 8$ K. Inset: zoom of the low field region. Units refer to the intensity ratio $2*(I^+ - I^-)/(I^+ + I^-)$ measured at the L_3 Mn edge (a) and M_5 Tb edge (b).

with 100% remanence is observed [48]. As XMCD averages over a macroscopic sample area, it is likely that both H_E and H_C would be much larger if measured at the single molecule level. We note

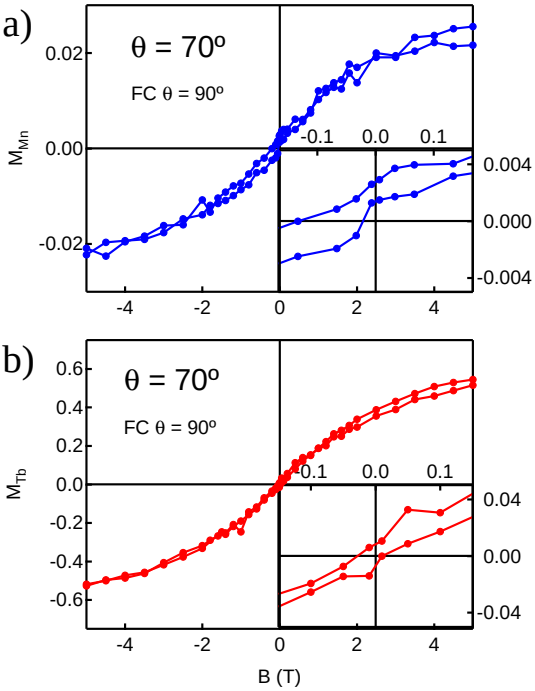

Figure 4.13: Magnetization loops of Mn (a) and Tb (b) measured on $TbPc_2$/Mn(3ML)/Ag(100), after FC at $\theta = 90°$ and $B = 5$ T, recorded at $\theta = 70°$ and $T = 8$ K. Inset: zoom of the low field region. Units refer to the intensity ratio $2^*(I^+ - I^-)/(I^+ + I^-)$ measured at the L_3 Mn edge (a) and M_5 Tb edge (b).

also that the blocking temperature of $TbPc_2$ deposited on metal substrates, measured on the timescale of XMCD experiments, is about 2 K [51], below the minimum temperature reached in this

study (8 K). Therefore, the alignment of the pinned spins must occur in the paramagnetic regime due to the field-induced magnetization of $TbPc_2$ [15]. Once AFM order has set in, the uncompensated exchange field from the substrate inhibits the relaxation of the Tb magnetic moment, giving rise to hysteresis.

A second $TbPc_2$/Mn/Ag(100) sample was prepared and FC at $\theta = 90°$ and $B = +5$T, to investigate the effect of the field cooling direction. Hysteresis loops are reported in Fig. 4.13 (a), (b). In this case we observed a significant reduction of the vertical shift of the Mn loop compared to Fig. 4.12: the curve intercepts the ordinate axis at $0\,0012 \pm 0\,0012$. The shift of the Tb loop is also reduced to $0\,009 \pm 0\,009$ T, consistently with the tendency of the $TbPc_2$ to magnetize out-of-plane. We note also that magnetic anisotrpopy energy of the Mn thin film is expected to be low, so that it may be possible to induce in-plane pinned spins in this system.

Probably the small contribution is due to the small out-of-plane component we had measuring at $\theta = 70°$. In any case, we can state that moleules could easly couple with substrate when the two easy axis are colliner; when they are orthogonal, the coupling is weaker or absent.

4.3 Summary

In summary, we have observed exchange bias in a SMM/AFM system. The magnetization of $TbPc_2$ deposited on CoO and Mn thin films, FC to 8 K, present significant differences: the first is typical of paramagnetic $TbPc_2$, whereas the second is an hysteretic loop shifted to negative field. The Mn magnetization loop reveals the presence of both pinned and unpinned spins, with the former aligned parallel to the FC direction. Thus, molecular scale magnets are able to induce exchange bias when deposited on AFM films. From the shape of the $TbPc_2$ magnetization curve, we infer that exchange bias occurs at the level of single molecules.

Chapter 5

MnPc deposited on several substrates

This chapter presents a series of measurements of the same paramagnetic metal-organic molecule, the Mn phthalocyanine (MnPc), deposited on different substrates. The first part of the chapter shows the results on different conditions, like the bulk MnPc in a powder or evaporated on another layer of molecules (CuPc), or on clean metallic substrates, while the second part focuses on the interaction with magnetic layers and it investigates the coupling between molecule and the surface.

5.1 MnPc powder

The main reason for studying the MnPc powder sample is to have a bulk reference to compare the spectra recorded on MnPc thin films (1ML) on metallic substrates. MnPc powder is also interesting because, in the so called β-form, it presents ferromagnetism at low temperature. β-MnPc consists of a stacking arrangement of the planar molecules along the monoclinic b axis. Each Mn atom lies directly above or below the N atoms of the adjacent parallel MnPc molecules. The distance between Mn and N atoms is 3 38Å, which is shorter than that in other β-crystals of MPc s molecules. The ferromagnetic behaviour is explained qualitatively by the 90° super-exchange interaction between nearest-neighboring Mn atoms via the N π orbitals of the Pc ring [5, 7, 44, 92].

MnPc powder sample was not prepared by using molecular beam epitaxy. The sample was made outside the chamber, glueing MnPc powder (Sigma Aldrich) with carbon tape to the sample holder, and afterwards inserted in the chamber. Figure 5.1c shows the linear spectra recorded at room temperature, along in-plane and out-of-plane directions. As expected, the two spectra are almost perfectly superposed: there is no preferential direction and the molecules are randomly distributed in all directions.

Figure 5.1a,b reports circular polarized absorption spectra and the difference. The sample was measured after cooling down to $T = 8$K, with a magnetic field applied of $B = 5$T. The shape of

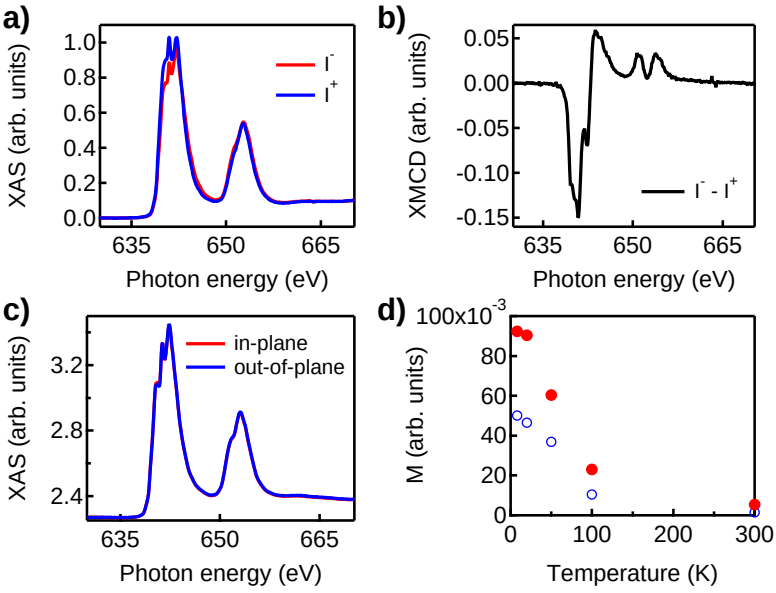

Figure 5.1: XAS (a) and XMCD (b) spectra of the MnPc powder measured at $\theta = 20°$, B = 5T and T = 8K. Linear absorption spectra (c) recorded at $\theta = 70°$ and T = 300K. Temperature dependence of the magnetic moment (d) measured cooling down in field the sample. The magnetic moments are estimated considering the L_3 edge area normalized to the one of the average absorption spectra.

the XMCD spectrum, measured at $B = 5$T, agrees with the one reported in reference [44]. In their work, Kataoka *et al.* observe a change in the XMCD shape between high fields (2,4 and 8T) and low field (0 1T). They explain this change by supposing the presence of both paramagnetic, due to different crystalline phases or impurities in the powder, and ferromagnetic, provided by Mn ionic states, contributions. This interpretation is a little puzzling for several reasons: firstly, they claim to use β-MnPc powder, purified by vacuum sublimation, and they confirm the purity using MALDI-TOF-MS method; second, if there are both paramagnetic and ferromagnetic contributions, both will appear at low fields as at high fields, and the FM one will have to dominate.

We also measured the temperature dependence of the magnetization 5.1d, approximating the magnetic moment with the area of the L_3 edge normalized to the one of the average absorption spectrum. The behaviour is qualitatively similar to the one reported in previous works [5, 7, 44, 92], but we have no sharp transition at $T = 8$ 6K [44, 92]. This is probably due to the fact that our powder is not purified, presenting a blend of crystalline phases.

Considering our measurements, we could not deduce the ground state, although our spectra look the same as that of the MnPc powder with $S = 3$ 2 and an ^4E_g ground state. Further measurements and, above all, calculations are needed to verify this speculation.

5.2 MnPc on non magnetic substrates: CuPc/Ag(100) and Ag(100)

After measuring the MnPc powder, which could be considered as a free molecule neglecting molecule-molecule interactions, we decided to prepare different samples, with the aim of discovering how MnPc spectra are influenced by different substrates. The sample preparation process was the same, as described in paragraph 2.7: sputter-annealing cycles to clean the Ag(100) single crystal, MBE of MnPc to form a $\leq$1ML thick film of molecules on Ag; in the case of the MnPc/CuPc/Ag(100) we first deposited a 1ML of CuPc, and then we grew on top a second layer ($0\ 6 - 1$ML) of MnPc.

Linear spectra are reported in figure 5.2. The spectra of the left column referred to Mn edge, while the ones in the right column to the N K-edge. The first information we can infer is that the MnPc molecules stay flat on the surface, as expected for transition metal phthalocyanine (TMPc) on Ag(100) [56]. The linear spectra are not normalized, so the intensity of the L and K edges are proportional to the coverage, as we can notice in figure 5.2d for MnPc/CuPc/Ag.

To support our deductions on the linear spectra, we can also consider the STM and LEED images, recorded during the sample preparation. The main reason was to check the substrate quality and to calibrate the molecule deposition. The images are taken at room temperature and in UHV condition ($< 5 \cdot 10^{-10}$mbar).

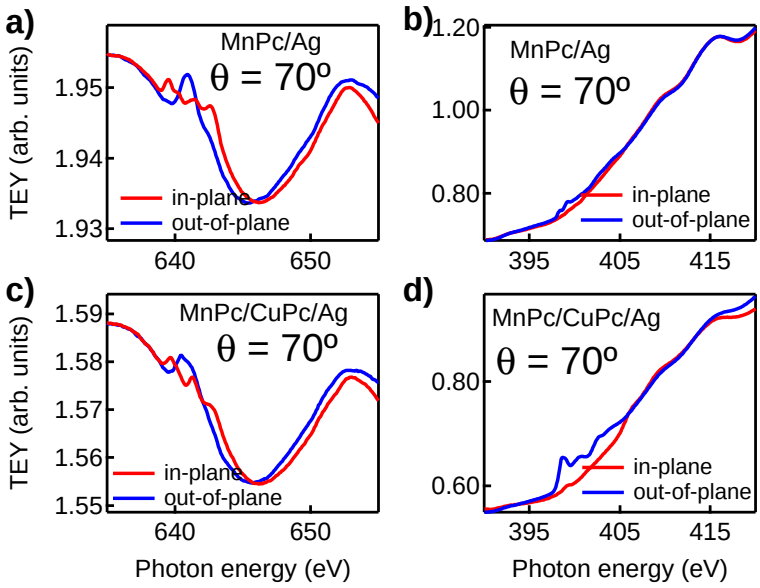

Figure 5.2: Linear in-plane and out-of-plane spectra of the MnPc/Ag (a and b) and MnPc/CuPc/Ag (c and d) samples, recorded at the Mn (left column) and N (right column) edges, with T = 300K and $B = 0$ 1T.

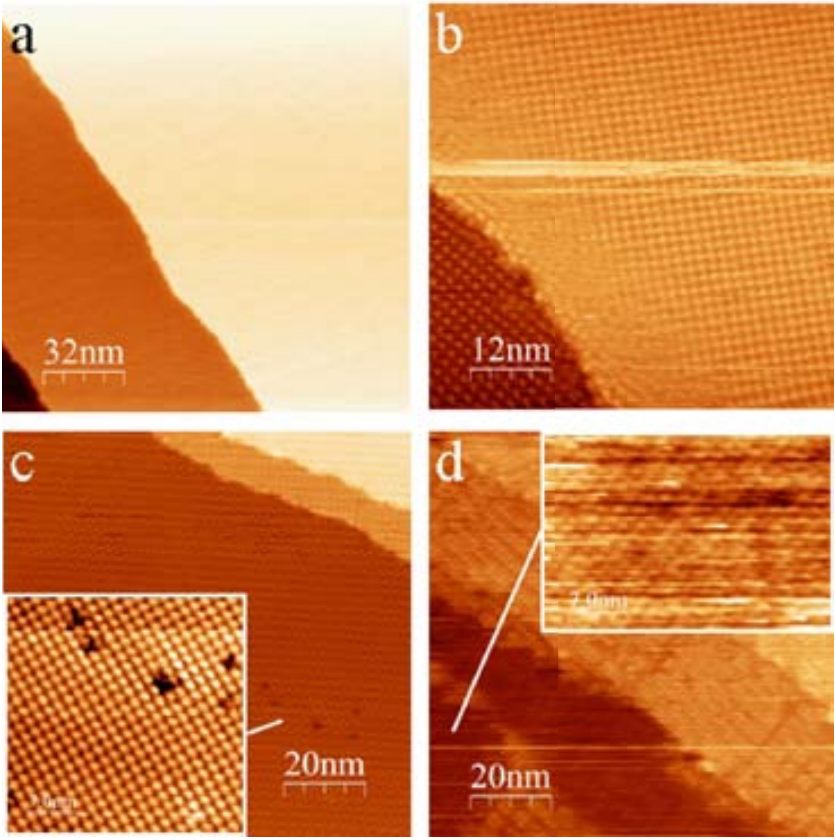

Figure 5.3: STM images recorded on clean Ag(100) (a), on MnPc/Ag(100) (b), on CuPc/Ag(100) (c) and on MnPc/CuPc/Ag(100). The scale is reported in the figure. Figures c and d show also a zoom of the image.

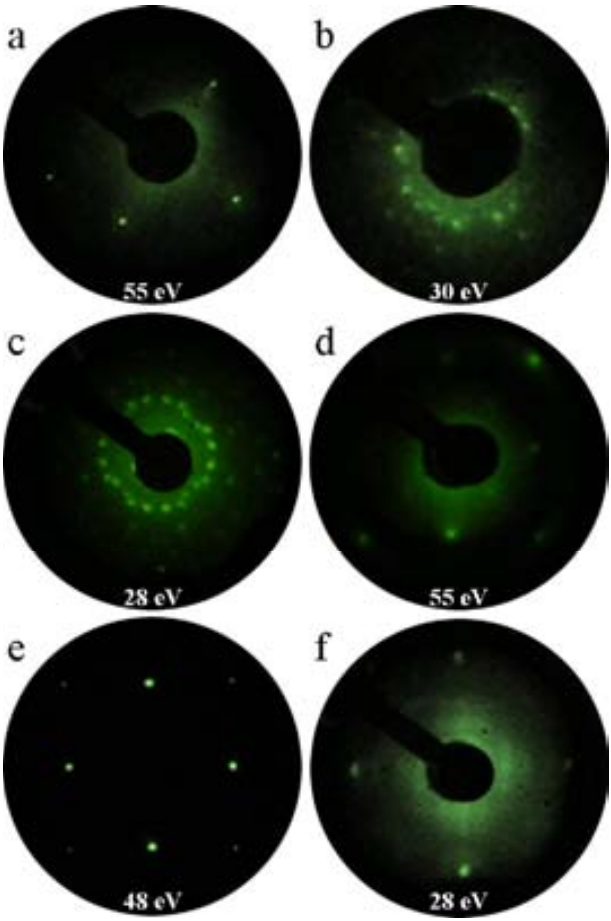

Figure 5.4: LEED images recorded on Ag(100) (a), on MnPc/Ag(100) (b), on CuPc/Ag(100) (c), on Ni/Ag(100) (d), on NiO/Ag(100) (e) and on MnPc/NiO/Ag(100) (f). The measurement energy is reported below each image.

Figure 5.3a shows the clean Ag(100) surface with clear terraces, while figure 5.3b presents the same surface after the deposition of MnPc: the molecules adsorb planar to the Ag(100) surface and self-assable in an ordered structure, in agreement with the linear spectra. In figure 5.4 we also report the low electron energy diffraction (LEED) images: the one for the Ag(100) surface present very few defined and bright spots, sign of the ordered Ag single crystal, while the LEED for the MnPc layer shows many more spots a little faded, that represent the ordered molecules on the surface. The same happened with CuPc on Ag(100): in the STM image (figure 5.3c) the CuPc molecules form an ordered layer and in the LEED image (figure 5.4c) we observe a more defined spots compared to the MnPc/Ag sample, but with a comparable pattern. Some problems arise when we put MnPc on top of the CuPc layer, because at this temperature the molecules move and interact with to bottom ones, giving a messed image (figure 5.3d) as a result. Nevertheless one can still recognize some pattern (see the zoom) and molecules on top.

For each sample we also recorded absorption spectra with circular polarized light (figure 5.5), at $\theta = 0°$ and $\theta = 70°$, after cooling down the sample to $T = 8$K with an applied field of $B = 5$T. XAS spectra of TMPcs on Ag are affected by a huge background, as also observed for $TbPc_2$ [48], and this can affect the estimation of the orbital and spin magnetic moments, since it is not possible to calculate the area of the average absorption spectrum. All the

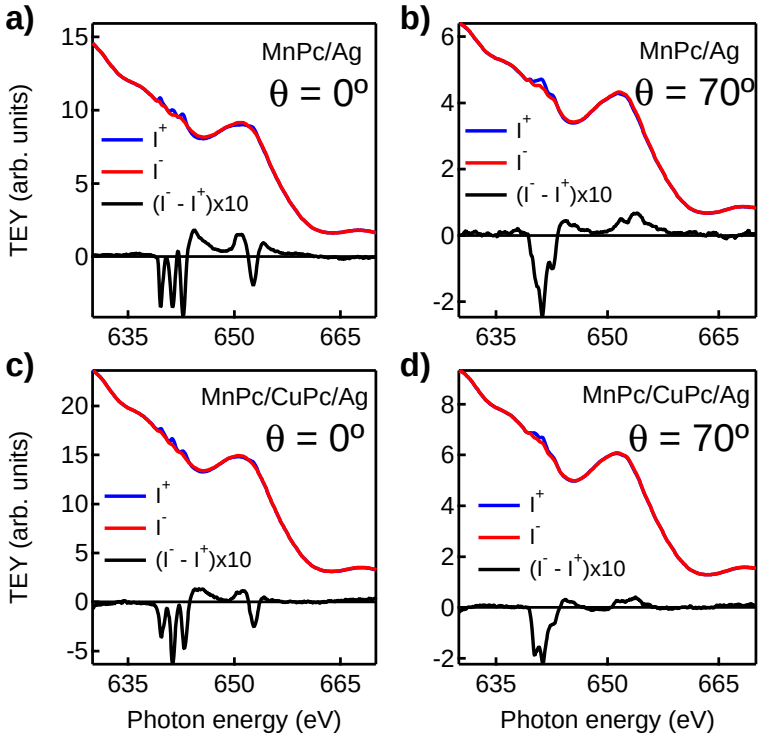

Figure 5.5: XAS and XMCD spectra of the MnPc/Ag (a and b) and MnPc/CuPc/Ag (c and d) samples, recorded at the Mn (left column) and N (right column) edges, with T = 8K and $B = 5$T.

spectra presented in figure 5.5 are normalized to the area of the L_3 edge of the average spectrum, calculated after subtracting a line around the edge in order to roughly eliminate the background. We chose this normalization instead of using the peak height because of the shape of the L_3 edge with multiple features and not a single peak. Figures 5.5a,b show XAS and XMCD spectra measured at the $L_{3,2}$ edges of Mn for MnPc/Ag(100). The XMCD spectrum at $\theta = 0°$ presents a peculiar shape, with the L_3 edge splitted into three distinguished peaks. The peaks blend together forming a single one with shoulders at $\theta = 70°$. The XMCD spectra are multiplied by a factor 10 in order to be visible. Things change slightly if we insert a monolayer of CuPc molecules between MnPc and the Ag(100) substrate (figure 5.5c,d). The shape of the XMCD still shows three peaks, but the first and third ones are smaller. This change in the spectra is a mark of the weakening of the interaction with the substrate: since MnPc sit on top of a layer of CuPc molecules, we could thick as they are almost free molecules. In order quantify the strength and the type of interaction with the substrate and neighbour molecules and to explain the shape of the XMCD spectra, we need the support of theoretical calculations.

5.3 MnPc on magnetic substrates

Me-Pc are paramagnetic molecules. One possible way to control the magnetic moment of the 3d metal center is to evaporate these

molecules on magnetic substrates. By exploiting XMCD element selectivity, Sheybal et al. showed for the first time that a manganese(III)tetraphenylporphyrin chloride (MnTPPCl) monolayer, when deposited on ferromagnetic Co substrate, presents a clear ferromagnetic exchange coupling [68]. After this work, other groups attempted to explore the nature of the exchange coupling, showing that the mechanism is an indirect superexchange mediate through N atoms [90]; moreover, they tried to tune and control the coupling by depositing, for example, an oxygen interlayer that modifies the coupling from ferromagnetic to an antiferromagnetic one [8, 20] or through a chemical switch of the coupling [88].

The coupling between paramagnetic MnPc molecules and a ferromagnetic Ni substrate is, then, easily predictable (paragraph 5.3.1), although it has no concrete application to real devices. Indeed, since all the molecules are coupled mimicking the substrate magnetization direction, it is not possible to control the magnetic moment of a single MnPc with respect to the other ones. As previously reported in chapter 4, it would be much more challenging to demonstrate the coupling of MnPc molecules with an antiferromagnetic substrate, measuring the presence of exchange bias in the sample. This is not an easy task to proof, as argued in paragraph 4.2; moreover, it should be noted that in this paragraph we are considering paramagnetic molecules instead of SMMs. On the other hand, it is also true that exchange bias was also recorded in ferromagnet in the paramagnetic state with $T_C < T_N$ [15].

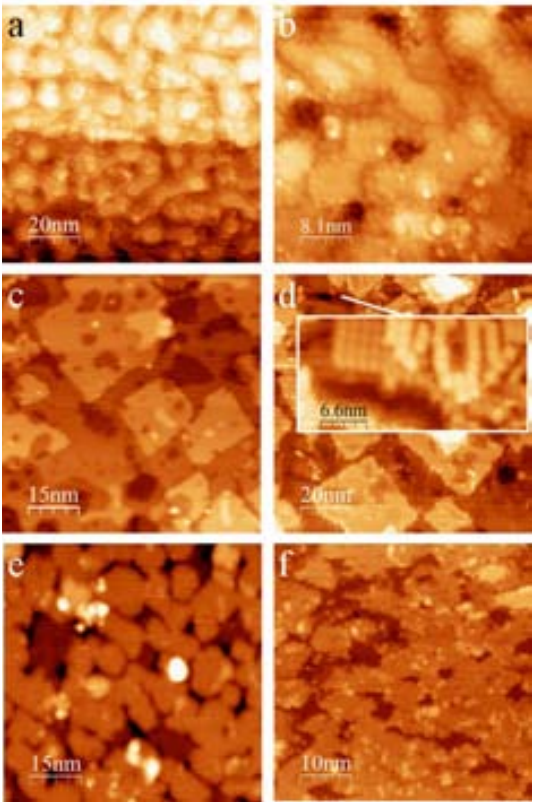

Figure 5.6: STM images recorded on Ni/Ag(100) (a), on MnPc/Ni/Ag(100) (b), on NiO/Ag(100) (c), on MnPc/NiO/Ag(100), on CoO/Ag(100) (e) and MnPc/CoO/Ag(100) (f). The scale is reported in the figure. Figure d shows a zoom of the image.

5.3.1 MnPc on ferromagnetic Ni film

MnPc molecules were evaporated on a Ni film, with a thickness between 10 and 20ML, grown on Ag(100) single crystal; these formed an almost complete ML. The STM images (figure 5.6a,b) show that Ni forms islands in the range of 10nm, large enough to put some molecules on top. The image taken after the evaporation of MnPc it is more difficult to describe, given that the molecules are moving as for MnPc/CuPc/Ag. The LEED image is taken at high energy, so what we see in figure 5.4 comes from the Ni substrate.

The molecules are not ordered on the surface but, at least, we can be sure of their presence. The linear spectra (not shown), with electric field probing in-plane and out-of-plane direction, prove that MnPc molecules also adsorb flat on Ni surface.

Ni film on Ag(100) is a ferromagnet with an in-plane easy axis, as one can see from the remanent spectra in figure 5.7a,b and also from the shape of the Ni hysteresis loops, recorded with normal and grazing incidence (Fig. 5.7e,f). This figure also reports absorption spectra recorded on L3 2 Mn edges at $B = 5$T and $B = 1$ 1T for $\theta = 0°$ and $\theta = 70°$, respectively. The XMCD spectrum at normal incidence presents the typical three peaks, as observed in paragraph 5.2, while in grazing incidence the peaks blend together. The XMCD spectra represented by solid lines were measured in remanence, after applying a $B = 5T$ magnetic

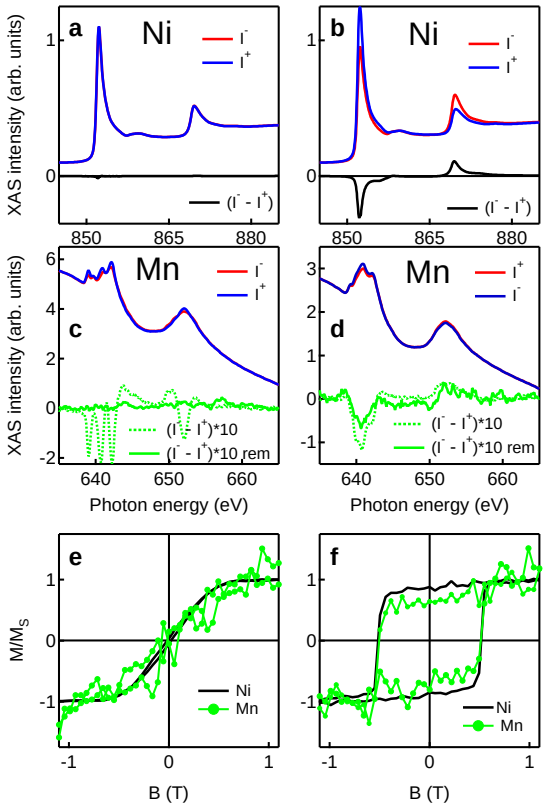

Figure 5.7: XAS, XMCD and hysteresis loops of the MnPc/Ni/Ag(100) sample, recorded on Ni and Mn L_3 edges at $\theta = 0°$ (left column) and $\theta = 70°$ (right column) at $T = 8K$. Ni spectra are measured in remanence after application of $B = 5T$ (a and b). Mn spectra, on the other end, are recorded at the saturation field, and we also add the XMCD spectra (solid line) in remanence (c and d). Magnetization curves were normalized to the saturation value to allow to compare the shape of Mn and Ni loops (e and f). All the XAS and XMCD spectra were normalized to the absorption average peak height.

field. The fact that the paramagnetic MnPc shows a clear XMCD peak in remanent field (Fig. 5.7d) is a proof that the molecule has a magnetic moment.

In figure 5.7e,f the loops recorded on Ni and Mn L_3 edge are reported. They were both normalized to the saturation value, allowing us to compare their shapes. Despite the noise of the Mn measurements, the hystereses almost perfectly overlapped, giving the same value of the coercivity at $\theta = 70°$. Hysteresis loops clearly demonstrate that MnPc is magnetized and that its magnetization mimics the one of the Ni substrate, since molecule and substrate are coupled. This behaviour is not new and it is predictable, since similar measurements were done on similar systems [8, 20, 48, 68, 90].

5.3.2 MnPc on antiferromagnetic oxide layers

This paragraph focuses the attention on proving the presence of exchange bias between paramagnetic MnPc molecules and AFM oxide layers. We studied two different samples, MnPc/NiO/Ag(100) and MnPc/CoO/Ag(100). Both were prepared in the same chamber, characterized by STM and LEED to check the oxide growth and the presence of molecules on the surface, and after that transfered in the XAS end station under UHV condition (see paragraph 2.7). NiO and CoO are supposed to be type II insulating antiferromagnets, but we need to be sure about their magnetic properties. XMCD is not the good technique to characterize these films, since

it is sensitive to the expectation value of the local magnetic moment M that vanishes for antiferromagnets. XNLD and XMLD on the other hand are proportional to the $\langle M^2 \rangle$ and for this reason we could observe a linear dichroic signal.

MnPc/NiO/Ag(100)

The first sample we take into account is the MnPc/NiO/Ag(100). The oxide layer has a thickness of 4ML, while there is only 1ML of molecules deposited. Figure 5.6c reports the STM image of the clean NiO layer and we notice that is similar to the images taken in our laboratory before the beamtime: the NiO presetns squared islands of different dimensions, some of 15-20nm other smaller. The LEED image (figure 5.4) with very well defined spots confirms that there is a quite ordered structure. After the evaporation of MnPc the LEED pattern change: the brighter spots of NiO structure become feeble, and some blended light appear in the center. There are no defined spots, as in the case of MnPc/Ag or CuPc/Ag, because there are no ordered structure in the molecules, since there are a lot of islads, all orented in different ways. The STM image (figure 5.6d) confirms this observation, and also shows that there is a formation of a second layer of MnPc (see the zoom) in some part of the sample. We have to take into account this fact when we will comment on XAS and XMCD spectra: some of the MnPc will act as almost free molecules, like in the case of MnPc/CuPc/Ag sample.

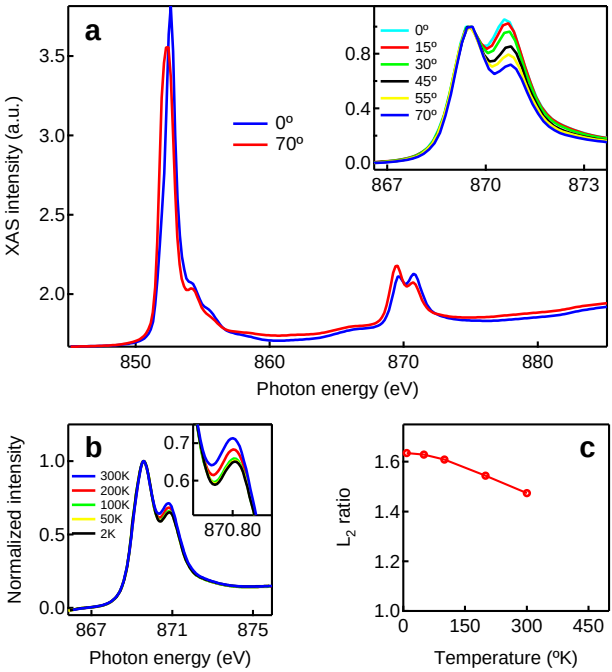

Figure 5.8: Angle and temperature dependence of the NiO substrate in the sample MnPc/NiO/Ag(100). (a) Linear spectra at normal and grazing incidence measured at the $L_{3,2}$ Ni edges at $T = 300K$. The inset shows the angle dependence of the L_2 edge second feature when the first feature is normalized to 1. (b) Temperature dependence of the second peak of the L_2 edge, when the spectra are normalized to the first peak height. (c) L_2 peaks ratio trend with respect to the temperature.

To characterize the NiO substrate we repeated the same measurements done before in references [2,3,91]. Figure 5.8 reports the L_2 edge angle and temperature dependence: the effects are quite small but well reproducible. Fig. 5.8a shows the linear horizontal spectra at normal and grazing incidence, recorded at room temperature. The inset on the top reports a zoom on the L_2 edge with the angle dependence, after normalizing the first feature to 1. Fig. 5.8b presents the temperature dependence of the L_2 edge, with a zoom on the second peak in the inset. The L_2 ratio between the two peaks, plotted with respect to the temperature, is reported in fig. 5.8c, showing a similar behaviour compared to previous measurements. Despite these similarities, we have to take into account few details. Since we did not heat our sample above the room temperature, we do not know the Néel temperature of the sample and we cannot be sure to have a completely aligned antiferromagnet when we cool down in field. For bulk NiO, $T_N \approx 520K$, but it is true that the latter drastically decreases by making the oxide thinner: for 5ML, it was reported that $T_N \approx 290K$ [2]. Another reference [3] reports a $T_N = 390K$ for 3ML of NiO. This implies that our sample is just at T_N or very close when we are at room temperature, but we have no proof of that. We can only suppose that our sample is antiferromagnetic, since the behaviour of the L_2 ratio vs temperature is similar, but the AFM domains are probably not completely aligned.

Aware of this, we continued the study of the sample measur-

ing circularly polarized spectra. The idea has been to search for exchange bias to prove the coupling of the MnPc molecule with the antiferromagnetic oxides, although $TbPc_2$ does not show any shift in the hysteresis loop (paragraph 4.2.1). This is a rather different system compared to $TbPc_2$ deposited on an oxide surface. First, we are considering now a paramagnetic molecule instead of a SMM, though it shows magnetic behaviour only at very low temperature. Second, the distance between Mn atom and the oxide surface could reasonably estimated to be approximately in the range $2\ 5 - 3\ 5$Å [22, 56], less then the distance of Tb atom to the surface, since $TbPc_2$ has an apparent height of 3Åand the rare earth sit in the middle [87]; moreover, it is important to take into account that for $TbPc_2$ and the surface there is the phtalocyanine that act as a spacer. The values reported refer to calculations that consider metallic surfaces, so that our systems could be slightly different. To our current knowledge, there is no written evidence of attempts to estimate the distance between molecules and oxide surfaces. Third, MnPc has no strong anisotropy as found in $TbPc_2$, so it has the chance to couple also with substrates with in-plane magnetic moments direction.

Figure 5.9 presents the XAS and XMCD spectra for this sample, recorded at the higher field available ($B = \pm 5$T), for both normal and grazing incidence, after field cooling with the positive maximum field applied at $\theta = 70°$. The spectra are normalized to the value of the XAS average area of the L_3 peak, estimated

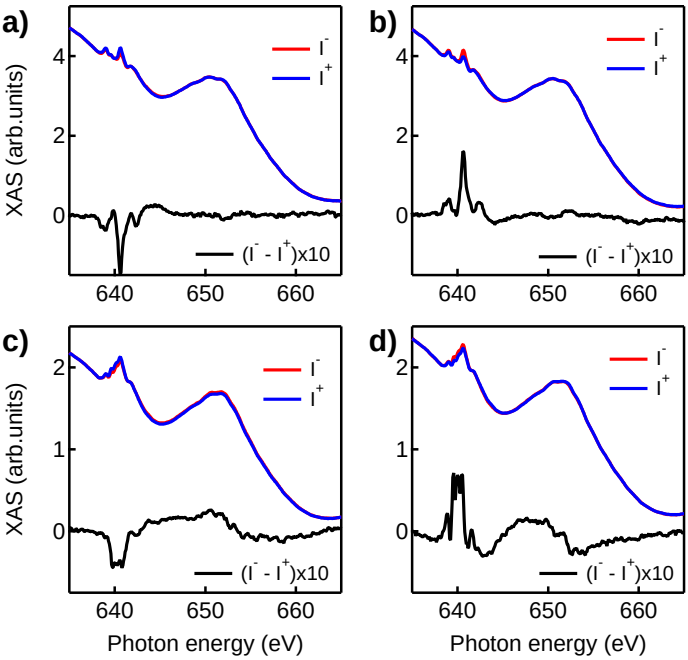

Figure 5.9: XAS ans XMCD spectra of the MnPc/NiO/Ag sample recorded at the $L_{3,2}$ Mn edges for $\theta = 0°$ (a and b) and $\theta = 70°$ (c and d), at $B = +5T$ (a and c) and $B = -5T$ (b and d). XMCD spectra were multiply by a factor 10 to be more visible.

after subtracting a line around the edge. In the figure, the XMCD is multiplied by a factor 10 in order to better visualize the shape and the peak height. The XMCD spectra at grazing incidence present an imbalance in the L_3 peak height, suggesting a possible exchange bias. However, the quality of measurements should also be taken into account. First of all, the two spectra at $B = \pm 5$T (Fig. 5.9c,d) present two different shapes, while we expected the same shape, but with opposite sign. Focusing then on the single spectrum, it is clear that in both cases the quality of the spectrum is low, with unusual bumps. The XAS spectra for the two polarizations were obtained averaging few scans, probably with some artifacts. On the contrary, the spectra at normal incidence do not show an unusual shape, presenting a specular shape at the two opposite filed. The peak height is almost the same for the two fields. Since no hysteresis loops were recorded on this sample, it is not possible to comment about the presence or absence of exchange bias. Further investigation is needed in order to deduce some conclusions about exchange bias.

MnPc/CoO/Ag(100)

This sample was prepared through the same process described more in details in paragraph 4.2.1: 10ML of CoO were grown epitaxially on a sputtered annealed Ag(100) surface and 0 8ML of MnPc molecules were evaporated on top. STM were used to check the quality of the sample and the presence of molecules on

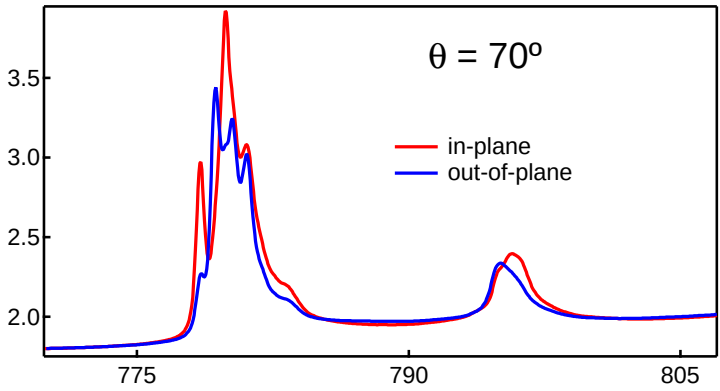

Figure 5.10: Linear in-plane and out-of-plane spectra on Co edges recorded at $\theta = 70°$, $B = 0$T and $T = 8$K.

top of the CoO. Figure 5.6e shows a nice structure with ordered islands of the same round shape and size, while figure 5.6f is less clear. As before, the molecules are moving on the surface and it is difficult to see them; also in this case there are some molecules on top of the other ones, but there is no evidence that they are forming cluster structures like in the MnPc/NiO/Ag sample.

In order to prove the AFM character of the oxide, we recorded linear polarized X-ray spectra at the Co edge, shown in figure 5.10. If we compare this linear spectra with figure 4.4 and other published works [1, 21], we notice that there are almost no differences, giving the proof that the CoO is antiferromagnetic.

Since CoO grown on Ag(100) with magnetic moments along

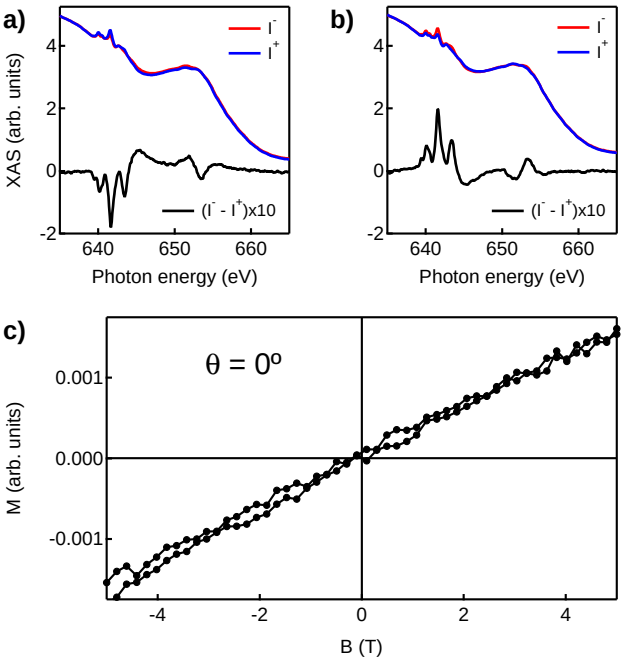

Figure 5.11: XAS and XMCD spectra of MnPc/CoO/Ag(100) recorded on Mn edges at $\theta = 0°$, $B = \pm 5$ (a and b, respectively) and $T = 8$K. Hysteresis loop recorded at the same angle and temperature (c).)

in-plane direction, the sample was field cooled to 8K at $\theta = 90°$ and $B = 5$T.

Measurements performed at $\theta = 0°$ are reported in figure 5.11. The XAS and XMCD spectra are normalized to the L_3 peak are of the XAS average spectrum, while the hysteresis point correspond to the height of the central peak of the L_3 edge divided by the

XAS average correspondent value. Figure 5.11a,b shows spectra recorded at $B = \pm 5$T. The shape is well reproducible and the two XMCD are specular to the abscissa. No sign of imbalance are detected. This is confirmed by the hysteresis loop in figure 5.11c, which is symmetrical to the origin without any trace of exchange bias.

Measuring along the field cool direction, we notice that the L_3 peak height of the XMCD spectra recorded at $B = +5$T and $B = -5$T does not show differences at the two opposite fields (Fig. 5.12a,c). This would suggest the absence of a shift in the hysteresis loop and, hence, the absence of a coupling between the oxide surface and the MnPc molecule, as for NiO. Surprisingly, the loop reported in figure 5.12e presents an imbalance, which denies the information of the spectra. It is worth noting that the hystereses shown in this chapter are measured in the same way described in paragraph 3.2.2. The value of the L_3 peak height, divided by the pre-edge value during a forward and backward sweep of the magnetic field, was thus measured. Recording two hysteresis loop for right and left circular polarized light and subtracting them, we obtained a loop that is approximately proportional to the magnetic moment. This is a faster method compared to the one reported in paragraph 4.2.1, but it sometimes lacks accuracy, especially if the measurements present some problems, like small drifts in energy during time.

To shade light on the interpretation of our spectra and loop,

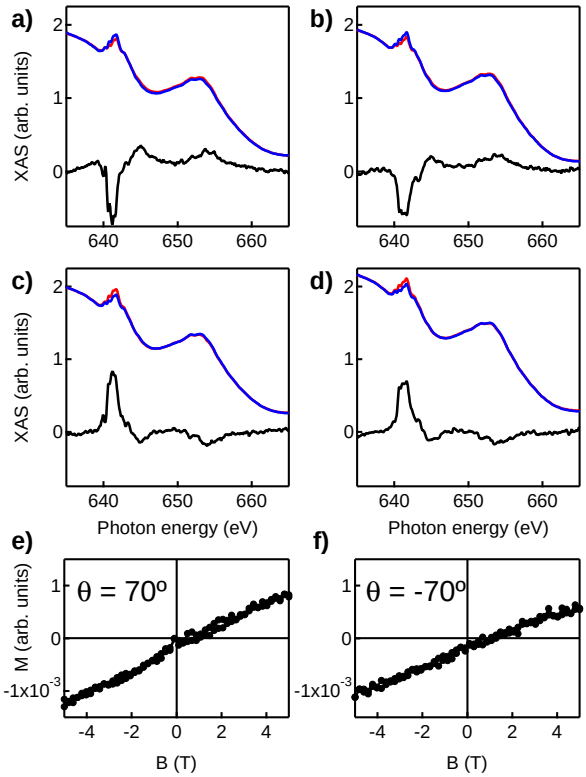

Figure 5.12: XAS and XMCD spectra of MnPc/CoO/Ag(100) recorded on Mn edges at $\theta = \pm 70°$ (a,c and b,d, respectively), $B = \pm 5$ (a,b and c,d, respectively) and $T = 8$K. Hysteresis loop recorded at the same temperature at $\theta = \pm 70°$ to check if the shift is real or an artifact (e,f).

we decided to perform the same measurements, but at the angle of $\theta = -70°$: what we expected, in the case of exchange bias, was that the direction of the shift would change [62]. Figure 5.12f shows a magnetization curve with a positive shift as for $\theta = 70°$ loop. Also, the spectra (Fig. 5.12b,d) at $B = \pm 5$T did not exhibit any huge imbalance. Thus, we could safely conclude that no exchange bias was detected on MnPc/CoO/Ag(100) sample, as for NiO substrate, and the detected shift in the loops were just artifacts.

5.4 Shape comparison and estimation of magnetic moment

Considering only XAS and XMCD spectra of MnPc deposited on several different substrates it is not enough to reach a deep insight of the interaction between molecule and substrate. Further measurements and theoretical modeling of the system are mandatory for a complete understanding. Despite this preliminary remarks, we believe we can extract some useful observations from our first raw analysis.

First of all, it is interesting to start comparing the shapes of the XMCD spectra recorded. Figures 5.13 and 5.14 report the XMCD spectra for all the sample presented in paragraph **??** and 5.3, measured at $\theta = 0°$ and $\theta = 70°$ respectively, with $B = 5$T and $T = 8$K. We also add the powder sample in both figures

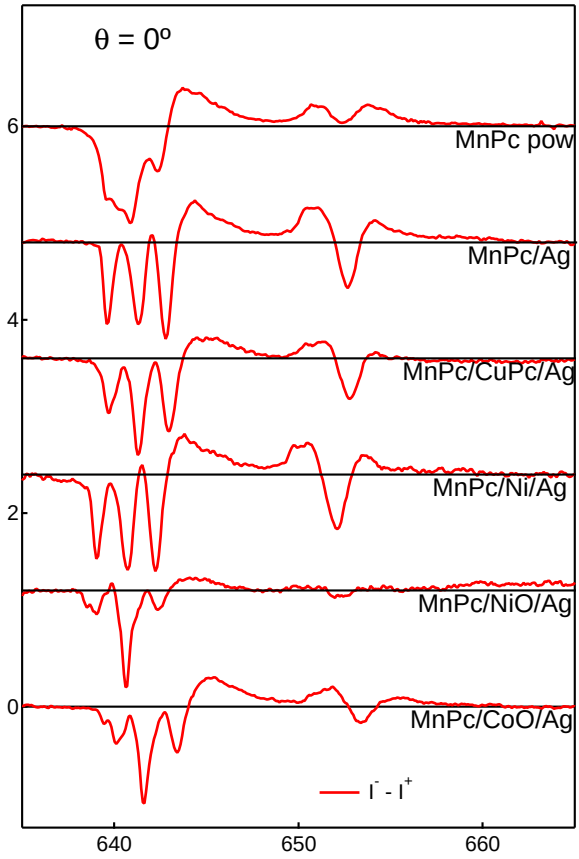

Figure 5.13: XMCD spectra recorded on Mn edges for all the MnPc samples, measured at $\theta = 0°$, $B = \pm 5$ and $T = 8$K. The spectra are normalized to the height of the taller peak of the L_3 edge, so that it is easier to compare the shape.

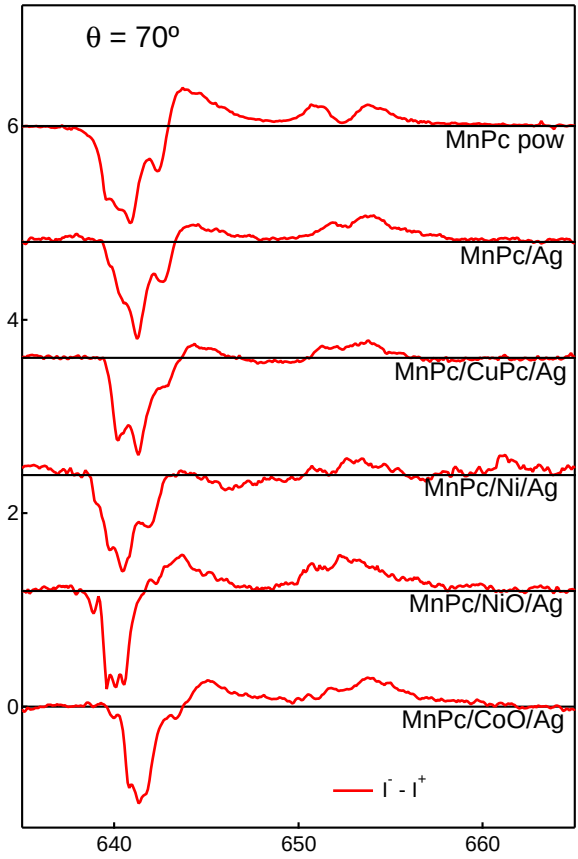

Figure 5.14: XMCD spectra recorded on Mn edges for all the MnPc samples, measured at $\theta = 70°$, $B = \pm 5$ and $T = 8$K. The spectra are normalized to the height of the taller peak of the L_3 edge, so that it is easier to compare the shape.

although it was measured only at $\theta = 20°$, thought the spectum does not change with the angle. Focusing on figure 5.13, one could clearly distinguish three groups considering the shape: MnPc on Ag(100) and on Ni/Ag(100), with a three peaks L_3 edge with almost the same height; MnPc on CuPc/Ag(100), with the first and the third peak of half height with respect to the second one; MnPc on NiO/Ag(100) and CoO/Ag(100), with the side peaks much smaller. Transition metal phthalocyanines (TMPc) deposited on Ag(100) hybridize with the substrate. In the case of FePc and CoPc, the molecular orbital (MO) a_{1g}, that has a dominant d_{z^2} character, strongly hybridizes with the Ag-sp_z states; for NiPc and CuPc, since the a_{1g} orbital is occupied, the hybridization is much smaller. In this system charge transfer occurs from the substrate to the molecules: in the case of FePc and CoPc it induces a charge reorganization, while it adds an electron to the ligand π orbitals in NiPc and CuPc [56]. In the case of MnPc we can safely assume that the molecule behave similarly to FePc and CoPc, hybridizing strongly with the Ag(100) and receiving an extra charge from the substrate. Since the spectrum shape is equal to that of MnPc/Ag(100), MnPc/Ni/Ag(100) should have the same electronic configuration, so we assume that MnPc strongly hybridize also on Ni and there is charge transfer from substrate to the molecule. The second group of spectra represents the free MnPc molecules: when there is a CuPc layer between Ag(100) surface and MnPc layer, we can presume that MnPc does not interact

with Ag and there is no charge transfer. MnPc powder spectrum can be added to this group, although the shape seems to be different; this is the effect of a distribution of the molecules along all the directions. Summing the spectra of the MnPc/CuPc/Ag(100) at $\theta = 0°$ and $\theta = 70°$, we almost reproduce the same feature of the powder spectrum (figure not shown). When MnPc is deposited on oxide thin films, like NiO and CoO, we observe that the trend of the XMCD spectra is followed, with a further decreasing of the side peaks height. We can then think that, in the case, the MnPc is oxidized and probably the charge transfer take place from the molecule to the substrate. The same happens in figure 5.14, although the almost decoupled group and the oxide one are less distinguishable.

It is now interesting to see how the magnetic moment of the MnPc molecule change with the different substrates. As seen before (paragraph 5.2), it is difficult to apply the sum rules due to the huge background. To overcome this hindrance we try to give an estimation of the amount of XMCD. In general, people use to normalize the XMCD L_3 peak height to the correspondent peak of the XAS average (or sum) spectrum. In this case, given the particular L_3 lineshape with three distict peaks, we opted for the ratio between the XMCD L_3 edge area normalized to the XAS average L_3 area. Figure 5.15 reports the values of the $XMCD_{area}$ XAS_{area} as a function of the substrate, both for $\theta = 0°$ and $\theta = 70°$, $B = 5$T and $T = 8$K. MnPc molecule is paramagnetic, but in the β-form

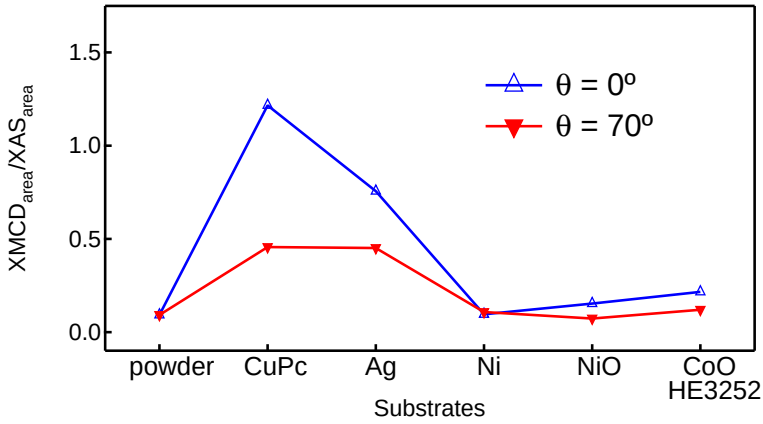

Figure 5.15: XMCD L_3 edge area normalized to the correspondent XAS L_3 edge area spectra recorded on Mn edges for all the MnPc samples, measured at $\theta = 70°$, $B = \pm 5$ and $T = 8$K.

it was found that there is a transition and the molecules become FM below 8 6K [7,44]. The first two points in the plot correspond to the cases closest to the free molecule, so we expect a perfectly paramagnetic behaviour and similar values of the magnetic moment with a magnetic field of $B = 5$T. The estimated magnetic moment is one order of magnitude bigger for MnPc monolayer on top of CuPc. The only plausible explanation is that the MnPc powder is AFM at low temperature, probably due to the presence of mixed β-form crystals oriented in opposite directions. The next two points in the plot belong to MnPc on Ag(100) and MnPc on Ni/Ag(100), which share the same L_3 lineshape. Also in this case there is a huge difference between the magnetic moments and, unexpectedly, MnPc on Ni presents the smaller moment. This is strange, since in paragraph 5.3.1, it was observed that MnPc is ferromagnetically coupled to the substrate, presenting the same hysteresis loops as Ni. Also, we find no differences between the moment at $\theta = 0°$ and $\theta = 70°$. This is not easy to explain, since we have no other data neither calculations, but we can at least formulate some plausible speculations. The first thing we can think is that the total spin ground state is different in the two cases. Mn ion in the MnPc molecule has a D_{4h} symmetry and has a $S = 3$ 2 ground state spin. Despite what was observed for FePc and CoPc, it could well be that, when deposited on a Ag(100) surface, the possible charge transfer is directed towards the ligand π orbitals instead to the transition metal. This is because MnPc, compared

to the other two phthalocyanine, is in a more stable configuration, having the d orbitals half filled. If the ligand spin is parallel to the TM spin we will have a total spin $S = 2 - \delta$ or, while in the opposite case, $S = 1 + \delta$, where $0 \leq \delta \leq 1$ and $1 \;\; 2 - \delta$ represents the fraction of charge transfer. The same consideration could also be done with the Ni substrate. If the spin on the ligand and the spin on the TM are parallel for Ag substrate, and antiparallel in the case of Ni, then we will find a bigger moment in one case with respect to the other one. One would expect a parallel allignement for MnPc on Ni, since the molecule is coupled ferromagnetically to the substrate, but this is not in contrast: the total spin can be aligned with the Ni magnetization, but decreased by the one sitting on the ligand. A second possible explication could be the presence of a Kondo effect in the MnPc/Ni/Ag(100) sample that partially screens the Mn magnetic moment: this is a quite daring hypothesis because normally the Kondo effect does not show up in ferromagnetic material, although in some particular geometries it was observed [16]. The last two points in figure 5.15 are the magnetic moments of the oxides sample. In this case the moments are very low, compared to the one of the Ni sample, and have a similar behaviour. Earlier on we safetly assumed that MnPc on these substrates is subject to an oxidation process that probably lead to a reduction of the total spin. We think than what we observe in figure 5.15 for the oxides substrates is in agreement with our hypotheses.

5.5 Summary

In this chapter we presented a systematic study of the same metal-organic molecule deposited in many different substrates. This study is still in its first stage and needs the support of further measurements and calculations. What we observed is that MnPc electronic structure is highly affected by the substrate and that the main mechanism that induce changes is likely charge transfer. In the case of magnetic substrates, we observed that MnPc ferromagnetically couples to a ferromagnetic Ni substrate, with Mn and Ni hysteresis loops perfectly overlapped. On AFM substrates, as NiO and CoO, no evidence of exchange bias was reported, although in one case we did not measure the hysteresis loop because we were unsure about the substrate and in the other one our measurements were affected by an artifact. This does not mean that MnPc could not couple to an AFM substrate. Finally, we tried to give an estimated value of the magnetic moment to each sample, finding big values for MnPc/CuPc/Ag and MnPc/Ag. This is unexpected because samples that show an almost equal XMCD spectrum, and, thus, electronic configuration, seem to have a very different magnetic moment. We tried to qualitatively give plausible explanations, but no conclusions can be drawn.

Chapter 6

Conclusions

This dissertation reports a series of experiments aimed to charectering and understanding the magnetic interaction between metal-organic molecules and magnetic substrates. We focus on two different molecules, the SMM bis-phthalocyaninato terbium ($TbPc_2$) and manganese phthalocyanine (MnPc). We prove that the magnetic moment of the $TbPc_2$ deposited on Ni is coupled antiparallel to that of the Ni substrate. The coupling depends on the relative direction of the easy axis of the molecule, which is out-of-plane, and the substrate. When the two easy axes are parallel, the magnetic moment of the $TbPc_2$ is stabilized by the interaction of the substrate and we observe a squared hysteresis loop with saturated magnetic remanence at zero applied field. Depending on the strength of the applied magnetic field, it is possible to increase the Zeeman interaction to compensate and eventually

overcome the exchange interaction, forcing the magnetic moments of Tb to align parallel to Ni. By oxidizing or reducing the magnetic surface, on the other hand, we showed that the strength of the exchange coupling can be significantly reduced or increased, respectively. The coupling also enhances the thermal stability of the $TbPc_2$ magnetic moment and we observe a finite remanent magnetization up to 100K, two orders of magnitude higher with respect to that of isolated $TbPc_2$. Moreover, if the $TbPc_2$ easy axis is orthogonal to that of the Ni layer, we note a frustration effect, since the molecule magnetization cannot align with the substrate, and the hysteresis loop shows zero remanence at zero applied field. The mechanism driving the coupling has to be clarified, but, considering our measurements, we suggest that a superexchange interaction between Tb and Ni mediated by the bottom Pc ligand is responsible of the reported effects.

Chapter 3 presents a series of experiments aimed at demonstrating the presence or absence of exchange bias between $TbPc_2$ and AFM substrates. No sign of exchange bias is observed for $TbPc_2$ on CoO films, showing a paramagnetic hysteresis loop symmetric with respect to the origin. We also tried to decrease the Néel temperature of the AFM layer, growing a 3ML thin substrate, and change the orientation of the Co easy axis, growing CoO on top of MnO, but none of these attempts changed the result. We then conclude that the exchange coupling for this system is absent or too weak to be measured. On the other hand, we found that

$TbPc_2$ couples to AFM Mn substrates. Hysteresis loops measured at the Tb edge are shifted towards negative fields, though the effect is small, and present an hysteretic shape, proving the presence of exchange bias. Magnetization curves recorded on the Mn edge show a vertical shift due to uncopensated pinned spins. From the shift we exstimate that only a 7% of the uncompensated spins are pinned. Mn and Tb loops are consistent: only molecules coupled to pinned spins contribute to the exchange bias, while the rest do not.

The last chapter presents a systematic study of XAS and XMCD spectra of MnPc at the interface with both magnetic and non magnetic substrates. By performing a comparative analysis of the XMCD shape, we find a trend going from metallic to oxide substrates, which demonstrates how MnPc electronic structure is affected by the surface layer. We assume that the main mechanism that induce changes is likely charge transfer. The magnetic moment of each sample is also estimated, when the higher magnetic field is applied. Surprisingly, samples with the same XMCD shape and, thus, electronic configuration, like MnPc/Ag and MnPc/Ni/Ag, show a difference of one order of magnitude. Concerning the interaction with magnetic substrates, MnPc is FM coupled to the Ni layer and its magnetic moment completely mimics the Ni magnetization, as also observed for similar paramagnetic molecules. As for $TbPc_2$, no signs of exchange bias appear when MnPc in evaporated on oxide AFM surface.

From these results we conclude that $TbPc_2$ are very promising SMMs for building metal/organic hybrid layers. The fact that this molecule behaves as a coupled but independent magnetic unit, the enhanced termal stability and the possibility to tune its coupling to a metallic substrate make SMM-FM systems very interesting for applications in hybrid devices. Furthermore, the demonstration of the coupling between single molecules and single pinned spins opens to the possibility of exploiting this interaction to build spin valve devices and spin filters, where the molecular magnetic moment is simultaneously stabilized and biased by unidirectional exchange coupling.

This work represents a starting point because a lot of things need to be done and, above all, understood. Studies of SMMs coupled to magnetic surfaces are at the first stage, especially the coupling SMM-AFM, since what we present here, at our present knowledge, is the first observation of exchange bias in such a system. Future experiments may address to deeply understand the coupling mechanisms between molecules and magnetic substrates. Even in the case of much more studied molecules, such as the Me-Pc, it is difficult to draw conclusions without the support of further measurements and calculations. Once this step is completed, efforts have to focus on experimenting other types of SMMs on different FM and AFM surfaces, in order to check if also other molecules behave in a similar way and also to improve the observed properties, such as the magnetic moment control and stability.

Publications

- A. Lodi Rizzini, C. Krull, J.J. Kavich, A. Mugarza, P. Moras, P. Sheverdyaeva, F. Yakhou, S. Stepanow, and P. Gambardella, **" "**, *in preparation*.

- A. Lodi Rizzini, C. Krull, T. Balashov, A. Mugarza, C. Nistor, F. Yakhou, V. Sessi, S. Klyatskaya, M. Ruben, S. Stepanow, and P. Gambardella, **"Exchange bias of single molecule magnets: $TbPc_2$ coupled to Mn and CoO antiferromagnetic films"**, *submitted*.

- S. K. Arora, B. J. O Dowd, C. Nistor, T. Balashov, B. Ballesteros, A. Lodi Rizzini, J. J. Kavich, S. S. Dhesi, P. Gambardella, and I. V. Shvets, **"Structural and magnetic properties of planar nanowire arrays of Co grown on oxidized vicinal silicon (111) templates"**, *J. Appl. Phys.*, **111**, 07E342 (2012)

- A. Lodi Rizzini, C. Krull, T. Balashov, J.J. Kavich, A.

Mugarza, P.S. Miedema, P.K. Thakur, V. Sessi, S. Klyatskaya, M. Ruben, S. Stepanow, and P. Gambardella, **"Coupling single molecule magnets to ferromagnetic substrates"**, *Phys. Rev. Lett.*, **84**, 177205 (2011).

- C. Nistor, T. Balashov, J.J. Kavich, A. Lodi Rizzini, B. Ballesteros, G. Gaudin, S. Auffret, B. Rodmacq, S.S. Dhesi, and P. Gambardella, **"Orbital moment anisotropy of Pt/Co/AlOx heterostructures with strong Rashba interaction"**, *Phys. Rev. B*, **84**, 054464 (2011).

- M. Ghidini, A. Lodi Rizzini, C. Pernechele, M. Solzi, R. Pellicelli, G. Zangari, P. Vavassori, **"Growth rate dependence of the extrinsic magnetic properties of electrodeposited CoPt films"**, *J. Mag. Magn. Mat.*, **322**, 1576-1580 (2010).

- G. Boero, S. Rusponi, J. Kavich, A. Lodi Rizzini, C. Piamonteze, F. Nolting, C. Tieg, J. Thiele, and P. Gambardella, **"Longitudinal detection of ferromagnetic resonance using x-ray transmission measurements"**, *Rev. Sci. Instr.*, **80**, 123902 (2009).

Bibliography

[1] R. Abrudan, J. Miguel, M. Bernien, C. Tieg, M. Piantek, J. Kirschner, and W. Kuch. Structural and magnetic properties of epitaxial fe coo bilayers on ag(001). *Phys. Rev. B*, 77(1):014411 , January 2008.

[2] D. Alders, J. Vogei, C. Levelut, S. D. Peacor, T. Hibma, M. Sacchi, L. H. Tjeng, C. T. Chen, G. van der Laan, B. T. Thole, and G. A. Sawatzky. Magnetic x-ray dichroism study of the nearest-neighbor spin-spin correlation function and long-range magnetic order parameter in antiferromagnetic nio. *EPL (Europhysics Letters)*, 32(3):259 , 1995.

[3] S. Altieri, M. Finazzi, H. H. Hsieh, M. W. Haverkort, H.-J. Lin, C. T. Chen, S. Frabboni, G. C. Gazzadi, A. Rota, S. Valeri, and L. H. Tjeng. Image charge screening: A new approach to enhance magnetic ordering temperatures in ultrathin correlated oxide films. *Phys. Rev. B*, 79(17):174431 , May 2009.

[4] T. Ambrose and C. L. Chien. Finite-size effects and uncompensated magnetization in thin antiferromagnetic coo layers. *Phys. Rev. Lett.*, 76(10):1743 1746, March 1996.

[5] Kunio Awaga and Yusei Maruyama. High-pressure effects on the canted ferromagnetism in manganese(ii) phthalocyanine. *Phys. Rev. B*, 44(6):2589 2594, August 1991.

[6] M. N. Baibich, J. M. Broto, A. Fert, F. Nguyen Van Dau, F. Petroff, P. Etienne, G. Creuzet, A. Friederich, and J. Chazelas. Giant magnetoresistance of (001)fe/(001)cr magnetic superlattices. *Phys. Rev. Lett.*, 61(21):2472 2475, November 1988.

[7] C. G. Barraclough, R. L. Martin, S. Mitra, and R. C. Sherwood. Paramagnetic anisotropy, electronic structure, and ferromagnetism in spin s = (3/2) manganese(ii) phthalocyanine. *J. Chem. Phys.*, 53(5):1638 1642, September 1970.

[8] M. Bernien, J. Miguel, C. Weis, Md. E. Ali, J. Kurde, B. Krumme, P. M. Panchmatia, B. Sanyal, M. Piantek, P. Srivastava, K. Baberschke, P. M. Oppeneer, O. Eriksson, W. Kuch, and H. Wende. Tailoring the nature of magnetic coupling of fe-porphyrin molecules to ferromagnetic substrates. *Phys. Rev. Lett.*, 102(4):047202 , January 2009.

[9] R. Biagi, J. Fernandez-Rodriguez, M. Gonidec, A. Mirone, V. Corradini, F. Moro, V. De Renzi, U. del Pennino,

J. C. Cezar, D. B. Amabilino, and J. Veciana. X-ray absorption and magnetic circular dichroism investigation of bis(phthalocyaninato)terbium single-molecule magnets deposited on graphite. *Phys. Rev. B*, 82(22):224406 , December 2010.

[10] G. Binasch, P. Grnberg, F. Saurenbach, and W. Zinn. Enhanced magnetoresistance in layered magnetic structures with antiferromagnetic interlayer exchange. *Phys. Rev. B*, 39(7):4828 4830, March 1989.

[11] S Blugel and P. H Dederichs. Ferromagnetism and Antiferromagnetism of 3d Metal Overlayers on Noble-Metal Substrates. *Europhys. Lett.*, 9(6):597 602, July 1989.

[12] Lapo Bogani and Wolfgang Wernsdorfer. Molecular spintronics using single-molecule magnets. *Nature Mater.*, 7(3):179 186, March 2008.

[13] Jens Brede, Nicolae Atodiresei, Stefan Kuck, Predrag Lazić, Vasile Caciuc, Yoshitada Morikawa, Germar Hoffmann, Stefan Blugel, and Roland Wiesendanger. Spin- and energy-dependent tunneling through a single molecule with intramolecular spatial resolution. *Phys. Rev. Lett.*, 105(4):047204 , July 2010.

[14] Patrick Bruno. Dipolar magnetic surface anisotropy in ferromagnetic thin films with interfacial roughness. *J. Appl. Phys.*, 64(6):3153 3156, September 1988.

[15] J. W. Cai, Kai Liu, and C. L. Chien. Exchange coupling in the paramagnetic state. *Phys. Rev. B*, 60(1):72 75, July 1999.

[16] M. Reyes Calvo, Joaquin Fernandez-Rossier, Juan Jose Palacios, David Jacob, Douglas Natelson, and Carlos Untiedt. The kondo effect in ferromagnetic atomic contacts. *Nature*, 458(7242):1150 1153, April 2009.

[17] Paolo Carra, B. T. Thole, Massimo Altarelli, and Xindong Wang. X-ray circular dichroism and local magnetic fields. *Phys. Rev. Lett.*, 70(5):694 697, February 1993.

[18] C. T. Chen, Y. U. Idzerda, H.-J. Lin, N. V. Smith, G. Meigs, E. Chaban, G. H. Ho, E. Pellegrin, and F. Sette. Experimental confirmation of the x-ray magnetic circular dichroism sum rules for iron and cobalt. *Phys. Rev. Lett.*, 75(1):152 155, July 1995.

[19] Per Helvig Christensen and Steen Mrup. On the magnetic dipole fields at surface atoms. *Journal of Magnetism and Magnetic Materials*, 35(13):130 132, March 1983.

[20] Dorota Chylarecka, Christian Wackerlin, Timur K. Kim, Kathrin Muller, Frithjof Nolting, Armin Kleibert, Nir-

malya Ballav, and Thomas A. Jung. Self-assembly and superexchange coupling of magnetic molecules on oxygen-reconstructed ferromagnetic thin film. *J. Phys. Chem. Lett.*, 1(9):1408 1413, April 2010.

[21] S. I. Csiszar, M. W. Haverkort, Z. Hu, A. Tanaka, H. H. Hsieh, H.-J. Lin, C. T. Chen, T. Hibma, and L. H. Tjeng. Controlling orbital moment and spin orientation in coo layers by strain. *Phys. Rev. Lett.*, 95(18):187205 , October 2005.

[22] D. G. de Oteyza, A. El-Sayed, J. M. Garcia-Lastra, E. Goiri, T. N. Krauss, A. Turak, E. Barrena, H. Dosch, J. Zegenhagen, A. Rubio, Y. Wakayama, and J. E. Ortega. Copper-phthalocyanine based metal organic interfaces: The effect of fluorination, the substrate, and its symmetry. *J. Chem. Phys.*, 133(21):214703 6, December 2010.

[23] B. Dieny, V. S. Speriosu, S. S. P. Parkin, B. A. Gurney, D. R. Wilhoit, and D. Mauri. Giant magnetoresistive in soft ferromagnetic multilayers. *Phys. Rev. B*, 43(1):1297 1300, January 1991.

[24] J. Dresselhaus, D. Spanke, F. U. Hillebrecht, E. Kisker, G. van der Laan, J. B. Goedkoop, and N. B. Brookes. Antiferromagnetic coupling of mn adsorbates to fe(100). *Phys. Rev. B*, 56(9):5461 5467, September 1997.

[25] P Gambardella. Magnetism in monatomic metal wires. *Journal of Physics: Condensed Matter*, 15(34):S2533 , 2003.

[26] P. Gambardella, H. Brune, S. S. Dhesi, P. Bencok, S. R. Krishnakumar, S. Gardonio, M. Veronese, C. Grazioli, and C. Carbone. Paramagnetic mn impurities on ge and gaas surfaces. *Phys. Rev. B*, 72(4):045337 , July 2005.

[27] P. Gambardella, A. Dallmeyer, K. Maiti, M. C. Malagoli, W. Eberhardt, K. Kern, and C. Carbone. Ferromagnetism in one-dimensional monatomic metal chains. *Nature*, 416(6878):301 304, March 2002.

[28] P. Gambardella, S. S. Dhesi, S. Gardonio, C. Grazioli, P. Ohresser, and C. Carbone. Localized magnetic states of fe, co, and ni impurities on alkali metal films. *Phys. Rev. Lett.*, 88(4):047202 , January 2002.

[29] Pietro Gambardella, Sebastian Stepanow, Alexandre Dmitriev, Jan Honolka, Frank M. F. de Groot, Magali Lingenfelder, Subhra Sen Gupta, D. D. Sarma, Peter Bencok, Stefan Stanescu, Sylvain Clair, Stephane Pons, Nian Lin, Ari P. Seitsonen, Harald Brune, Johannes V. Barth, and Klaus Kern. Supramolecular control of the magnetic anisotropy in two-dimensional high-spin fe arrays at a metal interface. *Nature Mater.*, 8(3):189 193, March 2009.

[30] J. B. Goedkoop, B. T. Thole, G. van der Laan, G. A. Sawatzky, F. M. F. de Groot, and J. C. Fuggle. Calculations of magnetic x-ray dichroism in the 3d absorption spectra of rare-earth compounds. *Phys. Rev. B*, 37(4):2086 2093, February 1988.

[31] Eberhard Goering, Alex Fuss, Wibke Weber, Judith Will, and Gisela Schutz. Element specific x-ray magnetic circular dichroism magnetization curves using total electron yield. *J. Appl. Phys.*, 88(10):5920 5923, November 2000.

[32] Mathieu Gonidec, Roberto Biagi, Valdis Corradini, Fabrizio Moro, Valentina De Renzi, Umberto del Pennino, Domenico Summa, Luca Muccioli, Claudio Zannoni, David B. Amabilino, and Jaume Veciana. Surface supramolecular organization of a terbium(iii) double-decker complex on graphite and its single molecule magnet behavior. *J. Am. Chem. Soc.*, 133(17):6603 6612, April 2011.

[33] F. Huang, M. T. Kief, G. J. Mankey, and R. F. Willis. Magnetism in the few-monolayers limit: A surface magneto-optic kerr-effect study of the magnetic behavior of ultrathin films of co, ni, and co-ni alloys on cu(100) and cu(111). *Phys. Rev. B*, 49(6):3962 3971, February 1994.

[34] C. Iacovita, M. V. Rastei, B. W. Heinrich, T. Brumme, J. Kortus, L. Limot, and J. P. Bucher. Visualizing the spin of in-

dividual cobalt-phthalocyanine molecules. *Phys. Rev. Lett.*, 101(11):116602 , September 2008.

[35] Naoto Ishikawa. Single molecule magnet with single lanthanide ion. *Polyhedron*, 26(911):2147 2153, June 2007.

[36] Naoto Ishikawa, Miki Sugita, Tadahiko Ishikawa, Shin-ya Koshihara, and Youkoh Kaizu. Lanthanide double-decker complexes functioning as magnets at the single-molecular level. *J. Am. Chem. Soc.*, 125(29):8694 8695, June 2003.

[37] Naoto Ishikawa, Miki Sugita, Tadahiko Ishikawa, Shin-ya Koshihara, and Youkoh Kaizu. Mononuclear lanthanide complexes with a long magnetization relaxation time at high temperatures: A new category of magnets at the single-molecular level. *J. Phys. Chem. B*, 108(31):11265 11271, June 2004.

[38] Naoto Ishikawa, Miki Sugita, Tomoko Okubo, Naohiro Tanaka, Tomochika Iino, and Youkoh Kaizu. Determination of ligand-field parameters and f-electronic structures of double-decker bis(phthalocyaninato)lanthanide complexes. *Inorg. Chem.*, 42(7):2440 2446, March 2003.

[39] Naoto Ishikawa, Miki Sugita, Naohiro Tanaka, Tadahiko Ishikawa, Shin-ya Koshihara, and Youkoh Kaizu. Upward temperature shift of the intrinsic phase lag of the magnetization of bis(phthalocyaninato)terbium by ligand oxidation

creating an s = 1/2 spin. *Inorg. Chem.*, 43(18):5498 5500, August 2004.

[40] Naoto Ishikawa, Miki Sugita, and Wolfgang Wernsdorfer. Quantum tunneling of magnetization in lanthanide single-molecule magnets: Bis(phthalocyaninato)terbium and bis(phthalocyaninato)dysprosium anions. *Angew. Chem.*, 44(19):2931 2935, 2005.

[41] W. Jauch, M. Reehuis, H. J. Bleif, F. Kubanek, and P. Pattison. Crystallographic symmetry and magnetic structure of coo. *Phys. Rev. B*, 64(5):052102 , July 2001.

[42] S. Javaid, M. Bowen, S. Boukari, L. Joly, J.-B. Beaufrand, Xi Chen, Y. J. Dappe, F. Scheurer, J.-P. Kappler, J. Arabski, W. Wulfhekel, M. Alouani, and E. Beaurepaire. Impact on interface spin polarization of molecular bonding to metallic surfaces. *Phys. Rev. Lett.*, 105(7):077201 , August 2010.

[43] P. J. Jensen. Magnetic recording medium with improved temporal stability. *Appl. Phys. Lett.*, 78(15):2190 2192, April 2001.

[44] T. Kataoka, Y. Sakamoto, Y. Yamazaki, V.R. Singh, A. Fujimori, Y. Takeda, T. Ohkochi, S.-I. Fujimori, T. Okane, Y. Saitoh, H. Yamagami, and A. Tanaka. Electronic configuration of mn ions in the - molecular ferromagnet -mn ph-

thalocyanine studied by soft x-ray magnetic circular dichroism. *Solid State Communications*, 152(9):806 809, May 2012.

[45] P. Kruger, O. Elmouhssine, C. Demangeat, and J. C. Parlebas. Magnetic structures of bct manganese in the bulk and at the (001) surface. *Phys. Rev. B*, 54(9):6393 6400, September 1996.

[46] S. J. Lee, J. P. Goff, G. J. McIntyre, R. C. C. Ward, S. Langridge, T. Charlton, R. Dalgliesh, and D. Mannix. Perpendicular antiferromagnetic ordering of mn and exchange anisotropy in fe/mn multilayers. *Phys. Rev. Lett.*, 99(3):037204 , July 2007.

[47] Po-Heng Lin, TaraJ. Burchell, Liviu Ungur, LiviuF. Chibotaru, Wolfgang Wernsdorfer, and Muralee Murugesu. A polynuclear lanthanide single-molecule magnet with a record anisotropic barrier. *Angewandte Chemie International Edition*, 48(50):9489 9492, 2009.

[48] A. Lodi Rizzini, C. Krull, T. Balashov, J. J. Kavich, A. Mugarza, P. S. Miedema, P. K. Thakur, V. Sessi, S. Klyatskaya, M. Ruben, S. Stepanow, and P. Gambardella. Coupling single molecule magnets to ferromagnetic substrates. *Phys. Rev. Lett.*, 107(17):177205 , October 2011.

[49] A. P. Malozemoff. Random-field model of exchange anisotropy at rough ferromagnetic-antiferromagnetic interfaces. *Phys. Rev. B*, 35(7):3679 3682, March 1987.

[50] A. P. Malozemoff. Heisenberg-to-ising crossover in a random-field model with uniaxial anisotropy. *Phys. Rev. B*, 37(13):7673 7679, May 1988.

[51] Ludovica Margheriti, Daniele Chiappe, Matteo Mannini, Pierre-E. Car, Philippe Sainctavit, Marie-Anne Arrio, Francesco Buatier de Mongeot, Julio C. Cezar, Federica M. Piras, Agnese Magnani, Edwige Otero, Andrea Caneschi, and Roberta Sessoli. X-ray detected magnetic hysteresis of thermally evaporated terbium double-decker oriented films. *Adv. Mater.*, 22(48):5488 5493, 2010.

[52] D. Mauri, H. C. Siegmann, P. S. Bagus, and E. Kay. Simple model for thin ferromagnetic films exchange coupled to an antiferromagnetic substrate. *J. Appl. Phys.*, 62(7):3047 3049, October 1987.

[53] W. H. Meiklejohn and C. P. Bean. New magnetic anisotropy. *Phys. Rev.*, 102(5):1413 1414, June 1956.

[54] W. H. Meiklejohn and C. P. Bean. New magnetic anisotropy. *Phys. Rev.*, 105(3):904 913, February 1957.

[55] Tru Moriya. Anisotropic superexchange interaction and weak ferromagnetism. *Phys. Rev.*, 120(1):91 98, October 1960.

[56] A. Mugarza, R. Robles, C. Krull, R. Korytr, N. Lorente, and P. Gambardella. Electronic and magnetic properties of molecule-metal interfaces: Transition-metal phthalocyanines adsorbed on ag(100). *Phys. Rev. B*, 85(15):155437 , April 2012.

[57] Aitor Mugarza, Cornelius Krull, Roberto Robles, Sebastian Stepanow, Gustavo Ceballos, and Pietro Gambardella. Spin coupling and relaxation inside molecule-metal contacts. *Nature Commun.*, 2:490 , October 2011.

[58] Reiko Nakajima, J. Sthr, and Y. U. Idzerda. Electron-yield saturation effects in l-edge x-ray magnetic circular dichroism spectra of fe, co, and ni. *Phys. Rev. B*, 59(9):6421 6429, March 1999.

[59] J Noguès and Ivan K Schuller. Exchange bias. *Journal of Magnetism and Magnetic Materials*, 192(2):203 232, February 1999.

[60] J. Noguès, S. Stepanow, A. Bollero, J. Sort, B. Dieny, F. Nolting, and P. Gambardella. Simultaneous in-plane and out-of-plane exchange bias using a single antiferromagnetic layer resolved by x-ray magnetic circular dichroism. *Appl. Phys. Lett.*, 95(15):152515 3, October 2009.

[61] R Nunthel, T Gleitsmann, P Poulopoulos, A Scherz, J Lindner, E Kosubek, Ch Litwinski, Z Li, H Wende, K Baberschke, S Stolbov, and T.S Rahman. Epitaxial growth of ni on cu(001) with the assistance of o-surfactant and its magnetism compared to ni/cu(001). *Surface Science*, 531(1):53 67, May 2003.

[62] H. Ohldag, A. Scholl, F. Nolting, E. Arenholz, S. Maat, A. T. Young, M. Carey, and J. Stohr. Correlation between exchange bias and pinned interfacial spins. *Phys. Rev. Lett.*, 91(1):017203 , July 2003.

[63] Kyungwha Park. Antiferromagnetic coupling of the single-molecule magnet mn_{12} to a ferromagnetic substrate. *Phys. Rev. B*, 83(6):064423 , February 2011.

[64] S. Parkin, Xin Jiang, C. Kaiser, A. Panchula, K. Roche, and M. Samant. Magnetically engineered spintronic sensors and memory. *Proc. IEEE*, 91(5):661 680, 2003.

[65] M. L. Sands R. Feynman, R. B. Leighton. *The Feynman Lectures on Physics*. Addison-Wesley, 1963.

[66] Florin Radu and Hartmut Zabel. Magnetic heterostructures, 2008.

[67] Stefano Sanvito. Molecular spintronics. *Chem. Soc. Rev.*, 40(6):3336 3355, 2011.

[68] A. Scheybal, T. Ramsvik, R. Bertschinger, M. Putero, F. Nolting, and T.A. Jung. Induced magnetic ordering in a molecular monolayer. *Chem. Phys. Lett.*, 411(13):214 220, August 2005.

[69] P. Schieffer, C. Krembel, M.-C. Hanf, M.-H. Tuilier, P. Wetzel, G. Gewinner, and K. Hricovini. High spin state of mn in an ideal monolayer on ag(001). *Eur. Phys. J. B*, 8(2):165 168, March 1999.

[70] P Schieffer, M.-H Tuilier, M.-C Hanf, C Krembel, and G Gewinner. Sexafs investigation of bct mn grown epitaxially on ag(001) at room temperature. *Surf. Sci.*, 422(13):132 140, February 1999.

[71] B. Schulz and K. Baberschke. Crossover from in-plane to perpendicular magnetization in ultrathin ni cu(001) films. *Phys. Rev. B*, 50(18):13467 13471, November 1994.

[72] Ina Sebastian, Thomas Bertrams, Klaus Meinel, and Henning Neddermeyer. Scanning tunnelling microscopy on the growth and structure of nio(100) and coo(100) thin films. *Faraday Discuss.*, 114: , 1999.

[73] R. Sessoli, M. Mannini, F. Pineider, A. Cornia, and Ph. Sainctavit. *XAS and XMCD of Single Molecules Magnets*, chapter 10, pages 279 311. Springer-Verlag Berlin Heidelberg, 2010.

[74] Vassil Skumryev, Stoyan Stoyanov, Yong Zhang, George Hadjipanayis, Dominique Givord, and Josep Nogues. Beating the superparamagnetic limit with exchange bias. *Nature*, 423(6942):850 853, June 2003.

[75] S. Stepanow, A. Mugarza, G. Ceballos, P. Moras, J. C. Cezar, C. Carbone, and P. Gambardella. Giant spin and orbital moment anisotropies of a cu-phthalocyanine monolayer. *Phys. Rev. B*, 82(1):014405 , July 2010.

[76] Sebastian Stepanow, Jan Honolka, Pietro Gambardella, Lucia Vitali, Nasiba Abdurakhmanova, Tzu-Chun Tseng, Stephan Rauschenbach, Steven L. Tait, Violetta Sessi, Svetlana Klyatskaya, Mario Ruben, and Klaus Kern. Spin and orbital magnetic moment anisotropies of monodispersed bis(phthalocyaninato)terbium on a copper surface. *J. Am. Chem. Soc.*, 132(34):11900 11901, August 2010.

[77] J. Stohr. Exploring the microscopic origin of magnetic anisotropies with x-ray magnetic circular dichroism (xmcd) spectroscopy. *Journal of Magnetism and Magnetic Materials*, 200(13):470 497, October 1999.

[78] J. Stohr and R. Nakajima. Magnetic properties of transition-metal multilayers studied with x-ray magnetic circular dichroism spectroscopy. *IBM J. Res. Develop.*, 42:73 88, 1998.

[79] J. Stohr and H. C. Siegmann. *Magnetism. From Fundamentals to Nanoscale Dynamics*, chapter Topics in Contemporary Magnetism - Exchange Bias, pages 617 629. Springer - Verlag Berlin Heidelberg, 2006.

[80] T. Suzuki, M. Kurahashi, X. Ju, and Y. Yamauchi. Spin polarization of metal (mn, fe, cu, and mg) and metal-free phthalocyanines on an fe(100) substrate. *J. Phys. Chem. B*, 106(44):11553 11556, October 2002.

[81] Satoshi Takamatsu, Tadahiko Ishikawa, Shin-ya Koshihara, and Naoto Ishikawa. Significant increase of the barrier energy for magnetization reversal of a single-4f-ionic single-molecule magnet by a longitudinal contraction of the coordination space. *Inorg. Chem.*, 46(18):7250 7252, August 2007.

[82] Kentaro Takano, R. H. Kodama, A. E. Berkowitz, W. Cao, and G. Thomas. Interfacial uncompensated antiferromagnetic spins: Role in unidirectional anisotropy in polycrystalline $ni_{81}fe_{19}$ coo bilayers. *Phys. Rev. Lett.*, 79(6):1130 1133, August 1997.

[83] B. T. Thole, P. Carra, F. Sette, and G. van der Laan. X-ray circular dichroism as a probe of orbital magnetization. *Phys. Rev. Lett.*, 68(12):1943 1946, March 1992.

[84] B. T. Thole, G. van der Laan, J. C. Fuggle, G. A. Sawatzky, R. C. Karnatak, and J.-M. Esteva. 3d x-ray-absorption lines

and the $3d^9 4f^{n+1}$ multiplets of the lanthanides. *Phys. Rev. B*, 32(8):5107 5118, October 1985.

[85] E. Tsymbal. Evaluation of the magnetic dipolar fields from layered systems on atomic scale. *Journal of Magnetism and Magnetic Materials*, 130(13):L6 L12, February 1994.

[86] G. van der Laan and B. T. Thole. Strong magnetic x-ray dichroism in 2p absorption spectra of 3d transition-metal ions. *Phys. Rev. B*, 43(16):13401 13411, June 1991.

[87] Lucia Vitali, Stefano Fabris, Adriano Mosca Conte, Susan Brink, Mario Ruben, Stefano Baroni, and Klaus Kern. Electronic structure of surface-supported bis(phthalocyaninato) terbium(iii) single molecular magnets. *Nano Lett.*, 8(10):3364 3368, September 2008.

[88] Christian W´ackerlin, Dorota Chylarecka, Armin Kleibert, Kathrin Mller, Cristian Iacovita, Frithjof Nolting, Thomas A. Jung, and Nirmalya Ballav. Controlling spins in adsorbed molecules by a chemical switch. *Nat Commun*, 1:61 , August 2010.

[89] P. Weinberger, L. Szunyogh, C. Blaas, C. Sommers, and P. Entel. Magnetic properties of bulk $ni_c fe_{1-c}$ alloys, their free surfaces, and related spin-valve systems. *Phys. Rev. B*, 63(9):094417 , February 2001.

[90] H. Wende, M. Bernien, J. Luo, C. Sorg, N. Ponpandian, J. Kurde, J. Miguel, M. Piantek, X. Xu, Ph. Eckhold, W. Kuch, K. Baberschke, P. M. Panchmatia, B. Sanyal, P. M. Oppeneer, and O. Eriksson. Substrate-induced magnetic ordering and switching of iron porphyrin molecules. *Nat Mater*, 6(7):516 520, July 2007.

[91] J. Wu, J. S. Park, W. Kim, E. Arenholz, M. Liberati, A. Scholl, Y. Z. Wu, Chanyong Hwang, and Z. Q. Qiu. Direct measurement of rotatable and frozen coo spins in exchange bias system of coo/fe/ag(001). *Phys. Rev. Lett.*, 104(21):217204 , May 2010.

[92] Hiroyuki Yamada, Toshihiro Shimada, and Atsushi Koma. Preparation and magnetic properties of manganese(ii) phthalocyanine thin films. *J. Chem. Phys.*, 108(24):10256 10261, June 1998.